The investigation of photoelectric phenomena in the terahertz frequency range is a powerful tool to study nonequilibrium processes in low-dimensional structures. In this work, non-linear high frequency transport phenomena in graphene driven by the free-carrier absorption of electromagnetic radiation are explored. It is demonstrated that in the presence of adatoms and/or a substrate, as well as in the vicinity of graphene edges the carriers exhibit a directed motion in response to the alternating electric field of the terahertz radiation. Moreover, it is shown that these photoelectric phenomena can be giantly enhanced if graphene is deposited on a substrate with a negative dielectric constant. Novel models of the photocurrent generation are developed to describe the nonequilibrium processes in the purest two-dimensional material. The experiments together with the theoretical considerations give access to fundamental properties of graphene.

Universitätsverlag Regensburg

ISBN 978-3-86845-116-0

gefördert von:

Alumni der physikalischen Fakultät der Universität Regensburg e.V.

Universität Regensburg

Christoph Johannes Drexler

Dissertationsreihe Physik - Band 43

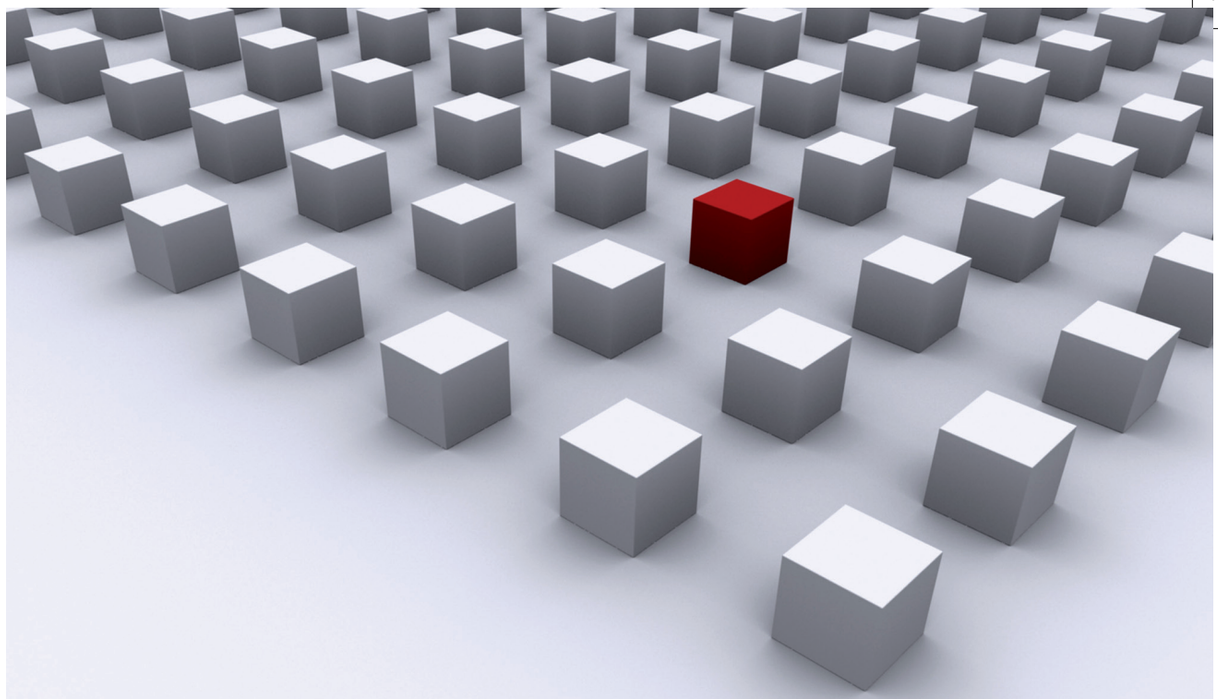

Christoph Johannes Drexler

Photoelectric Phenomena in Graphene Induced by Terahertz Laser Radiation

Universitätsverlag Regensburg

43

Dissertationsreihe Physik

Christoph Johannes Drexler

Photoelectric Phenomena in Graphene Induced by Terahertz Laser Radiation

Photoelectric Phenomena in Graphene Induced by Terahertz Laser Radiation

Dissertation zur Erlangung des Doktorgrades der Naturwissenschaften (Dr. rer. nat.)
der naturwissenschaftlichen Fakultät II - Physik der Universität Regensburg
vorgelegt von

Christoph Johannes Drexler

aus Hutthurm
im Mai 2014

Die Arbeit wurde von Prof. Dr. Sergey D. Ganichev angeleitet.
Das Promotionsgesuch wurde am 16.04.2014 eingereicht.

Prüfungsausschuss:	Vorsitzender:	Prof. Dr. Gunnar Bali
	1. Gutachter:	Prof. Dr. Sergey D. Ganichev
	2. Gutachter:	Prof. Dr. Josef Zweck
	weiterer Prüfer:	Prof. Dr. Franz J. Giessibl

Dissertationsreihe der Fakultät für Physik der Universität Regensburg, Band 43

Herausgegeben vom Präsidium des Alumnivereins der Physikalischen Fakultät:
Klaus Richter, Andreas Schäfer, Werner Wegscheider, Dieter Weiss

Christoph Johannes
Drexler

Photoelectric Phenomena in Graphene Induced by Terahertz Laser Radiation

Universitätsverlag Regensburg

Bibliografische Informationen der Deutschen Bibliothek.
Die Deutsche Bibliothek verzeichnet diese Publikation
in der Deutschen Nationalbibliografie. Detailierte bibliografische Daten
sind im Internet über http://dnb.ddb.de abrufbar.

1. Auflage 2014

Leibnizstraße 13, 93055 Regensburg

Konzeption: Thomas Geiger
Umschlagentwurf: Franz Stadler, Designcooperative Nittenau eG
Layout: Christoph Johannes Drexler
Druck: Docupoint, Magdeburg
ISBN: 978-3-86845-116-0

Weitere Informationen zum Verlagsprogramm erhalten Sie unter:
www.univerlag-regensburg.de

Contents

List of Figures

List of Tables

1 Introduction

With the realization of graphene [1], the first truly two-dimensional crystal of carbon atoms, A. K. Geim and K. S. Novoselov launched an avalanche of activities in science and technology leading to the nobel-prize in 2010. One of the reasons for the immense interest in graphene is the linear coupling between the charge carrier energy and momentum [2]. Resulting from its crystallographic structure, the energy dispersion of graphene resembles that of massless relativistic particles described by the Dirac equation [3]. Consequently, many unusual features appear in graphene, e. g. an extraordinary high electron mobility making graphene valuable for studies of phase coherent phenomena [4–7], a zero energy Landau level resulting in a half-integer quantum Hall effect which is unique for monolayer graphene [8, 9], a two-state degree of freedom due to the presence of two equivalent valleys which was suggested to be used in valleytronics [10], Klein tunneling [11–14], etc. (for review see e. g. Refs. [15–17]). These and many other phenomena result in a huge amount of potential applications [18], but on the way out of the labs straight into mass production and industrial applications, plenty of room for research and investigations on graphene is still given.

Most of the peculiarities listed above manifest in transport phenomena which are linear in the electric field and in the focus of research. In contrast, the transport phenomena which are nonlinear in the electric field are much less studied in graphene. In general, these effects result from the redistribution of charge carriers in the momentum and energy space, which were driven out of equilibrium by an alternating electric field provided, for instance, by external radiation. The radiation may cause both *ac* and *dc* current flows whose magnitudes are nonlinear functions of the field amplitude. Most of these effects are not peculiar for graphene and have been observed also in ordinary semiconductor systems, such as e. g. conventional two - and three - dimensional semiconductors [19, 20] as well as carbon based systems like carbon nanotubes and carbon films (for review see, [21]), before.

Considering graphene, the nonlinear transport phenomena which arise in response to an optical high frequency (HF) electric field have attracted attention just recently. The basic difference is that the effects are strongly enhanced in

graphene compared to their ordinary counterparts in semiconductors, basically due to the high electron velocity and the linear dispersion in graphene. Moreover, the microscopic mechanisms of these phenomena can be quite different in graphene. Among them can be found e. g., second - and third harmonic generation [22–24], frequency mixing [25], time-resolved photocurrents [26, 27] as well as the photon drag - and the photogalvanic effect [28, 29] (for review see [30]). The two latter effects result in *dc* currents being proportional to the squared amplitude of the *ac* electric field of terahertz (THz) laser radiation. The THz radiation induced photocurrents have proven to be a powerful tool to study nonequilibrium optical and electronic processes in semiconductors and provide information about their fundamental properties (for review see [19, 20]).

The main part of this thesis is aimed to the investigation of the nonlinear HF photoelectric phenomena in graphene resulting in a *dc* photocurrent. One of these phenomena is the magnetic quantum ratchet effect. Ratchets are systems which exhibit, due to their built-in asymmetry, a directed motion when they are driven out of equilibrium by an alternating force. Examples have been observed in various scientific fields (for review see [31, 32]). In graphene, being almost perfectly two-dimensional and highly symmetric, any ratchet mechanism is expected to be absent. However, it is demonstrated that when the symmetry is reduced by e. g., a substrate and/or adatoms, the Dirac electrons moving in an in-plane magnetic field drive a ratchet current. A shift of the electron orbitals leads to asymmetric carrier scattering for counter-propagating electrons. Hence, the periodic driving from THz radiation results in a directed ratchet current which indicates that orbital effects appear even in this purest possible two-dimensional system and gives access to the structure inversion asymmetry (SIA) in graphene.

In addition to the magnetic field induced currents, the chiral edge photocurrents induced in the vicinity of the edges of graphene are demonstrated. It is shown that the second order correction of the electric field results in a directed current restricted to a narrow channel close to the sample's edge. The investigations give direct access to the edge transport properties of graphene which are usually masked by the bulk transport properties.

Finally, the enhancement of the nonlinear photoelectric phenomena in gra-

phene within the spectral region of the reststrahl band of the substrate is demonstrated. The reststrahl band is characterized by a negative dielectric constant and almost perfect reflectivity. The strong modification of the local electric fields, acting on the carriers in graphene, due to the reflection at the substrate lead to anomalous spectral dependencies of the photocurrents which are amplified/ suppressed depending on the polarization state of the radiation. The modifications are described by a macroscopic Fresnel formalism what is remarkable since the studied epitaxial graphene samples are situated within atomic distances from the substrate.

In addition to the nonlinear photoelectric phenomena in graphene, the helicity sensitive detection of THz radiation by field effect transistors is demonstrated. The mechanism behind the generation of the *dc* response in a FET is quite different compared to that of the phenomena studied in graphene. However, the photosignals are several orders of magnitude higher. Consequently, the FETs show great potential as sensitive THz detectors. While the response to linearly polarized radiation has been addressed recently, the response which is sensitive to the helicity of circularly polarized THz radiation has not been observed so far.

The dissertation is organized as follows: In Chapter 2, the theoretical background which is necessary to study the nonlinear photoelectric phenomena in graphene is presented. The experimental methods are discussed in Chapter 3, containing an overview of the used sources of THz radiation as well as a description of the radiation's polarization state and methods for its variation. This is followed by the experimental setups and an overview of the investigated samples. Chapter 4 is devoted to the investigation of the magnetic quantum ratchet effect in graphene. A detailed experimental investigation is presented which is followed by a microscopic model and theory. In Chapter 5, the experimental observation of the chiral edge photocurrents is presented which is followed by a semiclassical theory. The reststrahl band assisted photocurrents are presented in Chapter 6. The experimental findings are discussed in terms of the phenomenological theory and qualitatively reproduced within a macroscopic Fresnel formalism. Finally, in the appendix of the thesis the helicity sensitive THz detection by field effect transistors is discussed.

2 Theoretical background

In the first chapter, the theoretical background of nonlinear HF photoelectric phenomena in graphene is presented. It starts with an introduction to the crystallographic and electronic properties of graphene, the monoatomic layer of carbon atoms. Therefore, the crystal structure resulting in a linear rather than a parabolic band structure is addressed. Moreover, the differences between the relativistic carriers in graphene and that in conventional two-dimensional (2D) electron or hole systems in semiconductor nanostructures are summarized. Subsequently, different optical absorption mechanism in graphene are presented.
Afterwards, the nonlinear HF photoelectric phenomena are introduced. First, a general description of the nonlinear response of the current density to an *ac* electric field oscillating with a frequency lying in the THz range is given. Subsequently, the focus is shifted towards the effects which are proportional to the squared amplitude of the radiation's electric field, i.e. the *dc* photocurrents. Three classes of phenomena are presented to give an idea how an *ac* THz field can be converted into a directed *dc* current.

2.1 Crystallographic and electronic properties of graphene

Discovered as the first perfect 2D crystal [1], graphene owes it's fundamental physical properties to its crystal structure. Due to sp^2 hybridization each carbon atom forms σ bondings to three nearest neighbor atoms with relative angles of 120°. The remaining p_z (π) orbital is decoupled from the hybridized orbitals and is delocalized over the entire crystal. As a result, the atoms assemble in the peculiar honeycomb lattice structure. The graphene lattice can be described by a unit cell with two atoms A and B, each of them arranged periodically in a triangular sublattice (Fig. 1 (a)). In real space, the primitive vectors are given by $\vec{a_1} = \frac{a}{2}\left(3, \sqrt{3}\right)$ and $\vec{a_2} = \frac{a}{2}\left(3, -\sqrt{3}\right)$ where $a = 0.142$ nm is the distance between nearest neighbors. In the reciprocal space the corresponding primitive vectors $\vec{A_1}$ and $\vec{A_2}$ are determined from the condition $a_i \cdot A_j = 2\pi\delta_{ij}$ leading to $\vec{A_1} = \frac{2\pi}{3a}\left(1, \sqrt{3}\right)$ and $\vec{A_2} = \frac{2\pi}{3a}\left(1, -\sqrt{3}\right)$. As a result,

the first Brillouin zone of the honeycomb lattice is a honeycomb lattice as well. A closer look onto the six points at the corners of the Brillouin zone reveals that two different groups of equivalent points are present which are denoted as K and K'. While points belonging to one group can be interconnected with the reciprocal lattice vectors, these vectors cannot connect the K with the K' points (see Fig. 1 (b)).

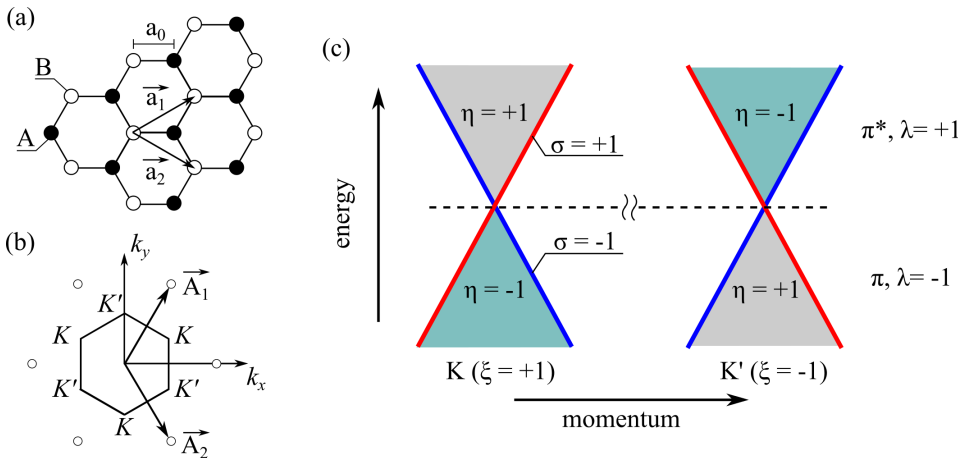

Figure 1: Honeycomb lattice of sp^2 hybridized carbon atoms in real (a) and momentum (b) space. (c) shows band structure of graphene close to the Dirac cones at K and K' with associated lattice pseudospins σ and chiralities η (grey and green cones).

Although graphene is experimentally available only for almost one decade, it has been theoretically investigated for the first time more than half a century ago [2]. P. R. Wallace derived the relation between energy E and momentum $\boldsymbol{k}$ of a carbon monolayer within a tight binding approximation up to second order nearest-neighbor hopping:

$$E_{\lambda=\pm1} \approx 3t' + \lambda\hbar v_F|\boldsymbol{k}| - \left(\frac{9t'a^2}{4} + \lambda\frac{3ta^2}{8}\sin(3\theta_k)\right)|\boldsymbol{k}|^2. \tag{1}$$

Herein, λ is the band index where "+1" stands for the conduction band (anti-bonding, π^*- orbitals) and "-1" for the valence band (bonding, π- orbitals), t is the nearest neighbor hopping amplitude (hopping between A and B sublattice), t' describes next nearest neighbor hopping (hopping within either A or B sublattice), $v_F = 3ta/2$ is the Fermi velocity and $\theta_k = \arctan^{-1}[k_x/k_y]$ is

the angle in the momentum space. In the vicinity of K- and K'-points Eq. (1) can be rewritten in the form

$$E^{\lambda}_{\boldsymbol{k},\xi=\pm1} = \lambda\hbar v_F|\boldsymbol{k}|, \tag{2}$$

by neglecting next nearest neighbor hopping. This relation is commonly used to describe graphene's band structure and reveals a linear connection of energy and momentum which was confirmed experimentally, for instance in Ref. [33]. The band dispersion is equal to that of ultrarelativistic particles with zero rest mass m_0, usually described by the Dirac equation instead of Schrödinger's equation [3]. Therefore, close to the K- and K'-points the carriers in graphene behave like relativistic particles with single-particle Fermi velocities in the order of 10^8 cm/s [16] and are often denoted "Dirac fermions", whereas K and K' are often referred to as the "Dirac points". Moreover, it follows from Eq. (2) that at the K- and K'-points where $|\boldsymbol{k}| = 0$, conduction and valence bands touch each other identifying graphene as a zero band-gap semiconductor or a semimetal. The band structure of graphene reveals several peculiarities which can be explained in terms of an effective Hamiltonian for spinless graphene carriers near the Dirac points [17]:

$$\mathcal{H}^{eff,\xi=\pm1}_{\boldsymbol{k}} = \xi\hbar v_F(k_x\sigma^x + \xi k_y\sigma^y). \tag{3}$$

Herein, $\sigma^{x,y}$ are the Pauli matrices describing the "sublattice" pseudospin quantum number $\boldsymbol{\sigma} = \pm1$. In addition, ξ describes the two equivalent valleys at the K- ($\xi = +1$) and K'-points ($\xi = -1$) which are called the "Dirac cones". Their presence reveals a two-fold valley degeneracy for graphene which is often referred to as the "valley" pseudospin. Although both pseudospins can be represented by Pauli matrices, they are independent of the electron spin.
The peculiar lattice and band structure of graphene leads to several new phenomena. For instance, the presence of the sublattice pseudospin leads to a novel chirality quantum number $\eta_{\boldsymbol{k}}$, also called helicity, which is described by the projection of the pseudospin onto the direction of motion of the carriers [17]:

$$\eta_{\boldsymbol{k}} = \frac{\boldsymbol{k}\cdot\boldsymbol{\sigma}}{|\boldsymbol{k}|}. \tag{4}$$

Thus, the chirality quantum number is $\eta = +1$ (-1) for particles within the conduction (valence) band (see different colors in Fig. 1 (c)) at the K-point, and

vice versa at the K'-point. In elastic scattering processes the chirality quantum number is conserved. This gives rise to the absence of intervalley scattering in pristine graphene and is the origin of Klein tunneling according to which a massless Dirac particle is fully transmitted, under normal incidence, through a high electrostatic barrier without being reflected [11–14]. Many other peculiar phenomena have been reported so far and are nicely reviewed, e. g. in Refs. [15–17].

To summarize, graphene's electronic properties differ significantly from that of conventional 2D semiconductor heterostructures. First, graphene is a gap-less semiconductor. While in common semiconductors 2D electrons or holes can only be studied in separately doped structures, in graphene both regions can be achieved within the same system by varying the Fermi level, e. g. by gating. Second, graphene particles are chiral, that of common semiconductor systems are not. This opens the door to completely different effects and physics. Third, graphene shows a linear dispersion relation rather than a quadratic one like conventional 2D semiconductors do. This gives rise to a vanishing effective mass of particles in graphene whereas carriers in conventional systems exhibit usually a finite effective mass. Finally, the carrier confinement in graphene is perfectly two-dimensional since the layer is exactly one atom thick (≈ 0.345 nm). By contrast, the confinement in heterostructures or quantum wells is usually in the order of a few nanometers or more and therefore, depending on the number of occupied subbands, not perfectly two-dimensional.

2.2 Optical transitions in graphene

Besides the peculiar electronic properties, graphene shows also interesting optical properties. Most outstanding is the almost frequency independent absorption of intrinsic graphene which assumes $\pi\alpha \approx 2.3\%$ in vacuum [34]. Therein, α is the fine-structure constant. However, for reasons shown below, the graphene samples investigated in this thesis are typically of n- type doping with Fermi energies of several hundreds of meV. In these structures, the condition $E_F\tau/\hbar >> 1$ is valid and electrons can be considered as free carriers. Consequently, depending on the Fermi - and the photon energy, additional absorption mechanisms become important.

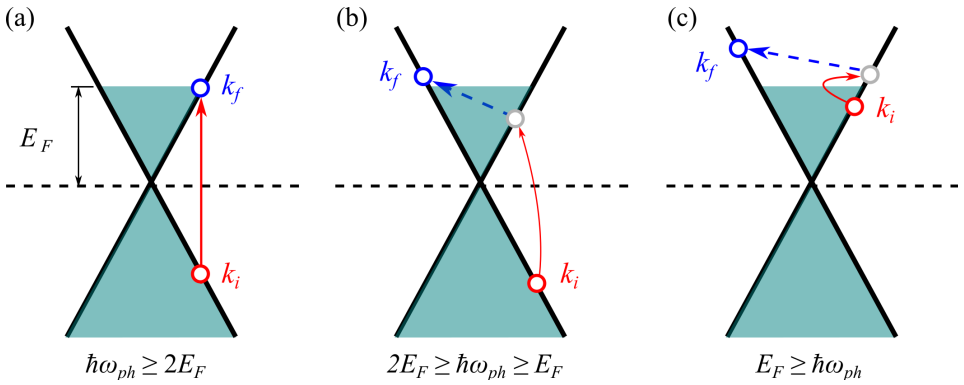

Figure 2: Scheme of possible transitions in graphene for $E_F > 0$: (a) direct interband transition, (b) indirect interband transition, (c) indirect intraband transition. Red arrows indicate electron-photon interaction, Blue dashed arrows represent electron scattering by impurities or phonons. Initial (Final) states are shown by red (blue) circles. Grey circles indicate virtual states.

In Fig. 2, the three different absorption regimes relevant for the conditions mentioned above are illustrated:

- **direct interband transitions:**
  In the case when the photon energy exceeds twice the Fermi energy, $\hbar\omega_{ph} \geq 2E_F$ (Fig. 2 (a)), the absorption of a photon results in the excitation of a final electronic state k_f.

- **indirect interband transitions:**
  If the condition $2E_F \geq \hbar\omega_{ph} \geq E_F$ is valid (Fig. 2 (b)), direct interband transitions are not possible. Assisted by electron scattering on phonons or impurities, an electronic state in the conduction band can be excited as far as energy- and momentum conservation are fulfilled.

- **indirect intraband transitions:**
  If the photon energy is lower than the Fermi energy (Fig. 2 (c)), the Drude-like free carrier absorption leads to indirect intraband transitions via intermediate states which are accompanied by electron scattering on phonons or impurities.

As it turns out, at THz frequencies ($\hbar\omega_{ph} \approx 10\,\mathrm{meV}$), the latter regime becomes dominant. In this case, the *ac* or high frequency conductivity, describing the electric current in response to the radiation's electric field, is given by:

$$\sigma(\omega) = \sigma_0 \frac{1 + i\omega\tau}{1 + (\omega\tau)^2}, \tag{5}$$

what is known as the Drude-Lorentz law of high-frequency conductivity [35]. The imaginary part of the conductivity indicates that the carriers lag behind the electric field of the radiation since they need roughly the time τ to accelerate in response to the change of the alternating field. This phenomenon is also called retardation and increases with higher angular frequencies ω.

2.3 Second order photoelectric effects

The aim of the thesis is to study *dc* photocurrents which result from the redistribution of a carrier ensemble in momentum space which was excited out of equilibrium by the absorption of THz radiation. In order to describe *dc* currents in response to an optical *ac* electric field it is convenient to use the coordinate and time-dependent electric current density $\boldsymbol{j}(\boldsymbol{r}, t) = \sigma \cdot \boldsymbol{E}(\boldsymbol{r}, t)$ and expand it in series of powers of the electric field $\boldsymbol{E}(\boldsymbol{r}, t) = \boldsymbol{E}(\omega, \boldsymbol{q}) \exp\left(i(-\omega t + \boldsymbol{q}\boldsymbol{r})\right) + \boldsymbol{E}^*(\omega, \boldsymbol{q}) \exp\left(i(\omega t - \boldsymbol{q}\boldsymbol{r})\right)$ [30]:

$$\begin{aligned} \boldsymbol{j}(\boldsymbol{r}, t) = &\left[\sigma^{(1)}_{\alpha\beta} E_\beta(\omega, \boldsymbol{q}) e^{-i\omega t + i\boldsymbol{q}\boldsymbol{r}} + c.c.\right] \\ &+ \left[\sigma^{(2')}_{\alpha\beta\gamma} E_\beta(\omega, \boldsymbol{q}) E_\gamma(\omega, \boldsymbol{q}) e^{-2i\omega t + 2i\boldsymbol{q}\boldsymbol{r}} + c.c.\right] \\ &+ \left[\sigma^{(2)}_{\alpha\beta\gamma} E_\beta(\omega, \boldsymbol{q}) E^*_\gamma(\omega, \boldsymbol{q}) + ...\right]. \end{aligned} \tag{6}$$

Herein, $\boldsymbol{q}$ is the photon wavevector, Greek subscripts represent Cartesian coordinates and c.c. stands for the complex conjugate. The first term in Eq. (6) describes the response which is linear in the electric field. The second term oscillates with 2ω and is known as the second harmonic generation. Effects related to the first two terms are out of scope of this thesis. In the focus are processes characterized by the second order nonlinear conductivity $\sigma^{(2)}_{\alpha\beta\gamma}$. These processes result in a static response which shows a quadratic dependence on the radiation's electric field $\boldsymbol{E}(\boldsymbol{r}, t)$, in other terms a linear dependence on the

radiation's intensity $I \propto |\boldsymbol{E}(\boldsymbol{r},\mathrm{t})|^2$.
Without any knowledge of the microscopic details, it is convenient to use symmetry arguments in order to characterize these effects upon variation of the radiation's polarization and its angle of incidence. Considering a spatial inversion $\boldsymbol{r} \to -\boldsymbol{r}$, the vector of the electric current density $\boldsymbol{j}(\boldsymbol{r}, t)$ changes its sign while the quadratic combination $E_\beta(\omega, \boldsymbol{q})E^*_\gamma(\omega, \boldsymbol{q})$ in the third term of Eq. (6) does not. Hence, second order effects are only allowed either if the second-order conductivity $\sigma^{(2)}_{\alpha\beta\gamma}(\omega, \boldsymbol{q})$ changes its sign upon spatial inversion or if the spatial inversion is not compatible with the symmetry of the system. The first condition is achieved if the conductivity tensor has components coupling to the photon wavevector $\boldsymbol{q}$ which changes its sign upon spatial inversion. The latter one is allowed if the studied system suffers a lack of inversion symmetry. Thus, the electric current density can be decomposed in two parts:

$$\boldsymbol{j}(\boldsymbol{r}, t) = \sigma^{(2)}_{\alpha\beta\gamma}(\omega, \boldsymbol{q})E_\beta(\omega, \boldsymbol{q})E^*_\gamma(\omega, \boldsymbol{q}), \tag{7}$$

$$= \left[\sigma^{(2)}_{\alpha\beta\gamma}(\omega, 0) + \Phi_{\alpha\beta\gamma\mu}(\omega)q_\mu\right] E_\beta(\omega, \boldsymbol{q})E^*_\gamma(\omega, \boldsymbol{q}), \tag{8}$$

The first term contains all contributions to $\sigma^{(2)}_{\alpha\beta\gamma}(\omega, 0)$ which are independent of the photon wavevector and describe the class of photogalvanic effects (PGE). The contributions which emerge due to the linear coupling to the photon wavevector are described by the fourth rank tensor $\Phi_{\alpha\beta\gamma\mu}(\omega)$. Such effects belong to the class of the photon drag effect (PDE). Both effects are discussed in the following.

2.3.1 The photon drag effect

The idea of a *dc* current flow in response to the photon momentum (second term of Eq. (8)), in other terms the radiation pressure, was introduced in 1935 [36]. In 1954, the effect was studied in the classical frequency limit of photon energies which are small compared to the typical electron energy [37]. In that work, the *dc* current is described as the result of the joint action of the radiation's electric and magnetic field and was denoted as the *ac* dynamic Hall effect. The effect was studied in epitaxial graphene in Ref. [28] as the classical limit of the PDE for photon energies which are small compared to the Fermi

energy ($E_{ph} << E_F$) in doped graphene samples. It was also shown that in the quantum limit of the drag current ($E_{ph} \leq E_F$) the dynamic Hall contribution $\propto E_\beta B^*_\gamma$, describing the coupling of the complex amplitudes of $\boldsymbol{E}$ and $\boldsymbol{B}$, can be written in the form of a photon drag effect $\propto q_\delta E_\beta E^*_\gamma$. The PDE was also observed in response to direct interband transitions [38], but this mechanism is out of scope of the present discussion.

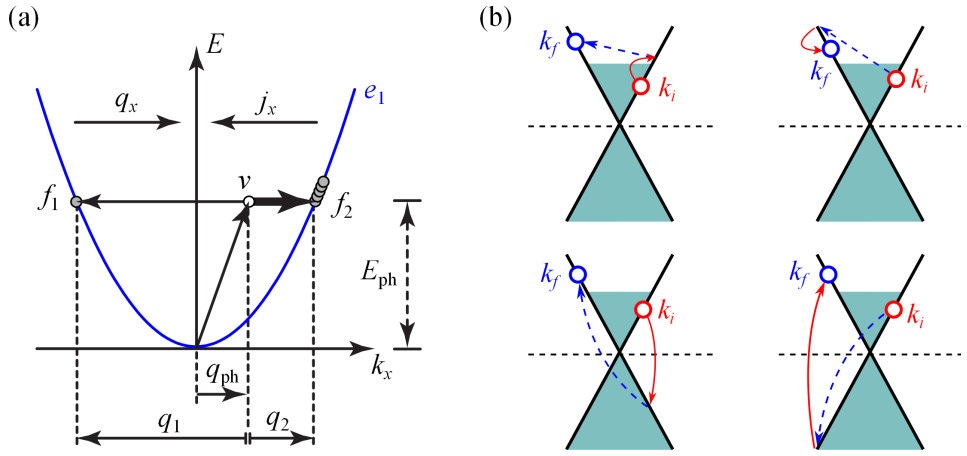

Figure 3: (a) Model of the PDE for a parabolic band-structure caused by Drude absorption, (b) schematic illustration of processes responsible for the drag current in doped graphene samples: red arrows denote electron-photon interaction, blue arrows stand for electron scattering by phonons/impurites.

A simplified scheme of the photon drag effect for a parabolic band structure and in response to Drude absorption is depicted in Fig. 3 (a). By taking into account the photon wavevector $\boldsymbol{q}_{ph}$ the excitation of an initial state ($k = 0$) into final electronic states f_1 and f_2 is done via a virtual state ν with $k \neq 0$. The lack of momentum between virtual and final states is provided by scattering processes, e. g. by acoustic phonons. The energy of acoustic phonons can be neglected in the THz range because it is small compared to the corresponding photon energies E_{ph}. Scattering events providing q_1 and q_2 appear with nonequal probabilities (see arrows of different thicknesses in Fig. 3 (a)). As a consequence, f_1 and f_2 get asymmetrically excited leading to an imbalance of carriers in $\boldsymbol{k}$-space, in other terms to a directed dc current j_x. Although this model is oversimplified it describes the underlying processes

behind the photon drag effect. In graphene, the PDE was studied within the quantum frequency range ($E_{ph} \leq E_F$) in Ref. [29] for doped systems where the intraband absorption process is more complex. A scheme for possible pathways is depicted in Fig. 3 (b). The Drude absorption appears via electron-photon interaction (red arrows) and is followed by an additional electron scattering process (blue dashed arrows) since energy and momentum conservation laws are violated otherwise.

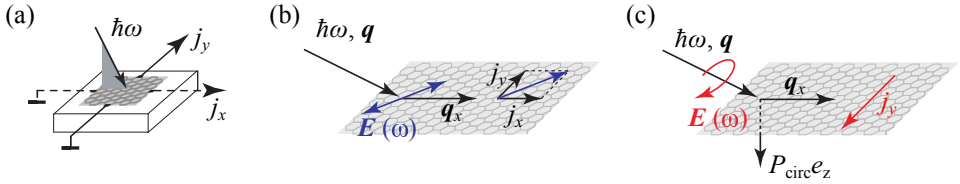

Figure 4: (a) experimental geometry of Eqs. (9) and (10); contributions to j_x and j_y due to the linear (b) and circular (c) photon drag effects.

Phenomenologically, the symmetry analysis of Eq. (8), considering the D_{6h} symmetry point group representative for a pristine graphene layer without substrate reveals the current density for the photon drag current in response to elliptically polarized radiation [29]:

$$j_x = T_1 q_x \left(\frac{|E_x|^2 + |E_y|^2}{2} \right) + T_2 q_x \left(\frac{|E_x|^2 - |E_y|^2}{2} \right), \tag{9}$$

$$j_y = T_2 q_x \left(\frac{E_x E_y^* + E_x^* E_y}{2} \right) - \tilde{T}_1 q_x P_{circ} \hat{e}_z (|E_x|^2 + |E_y|^2). \tag{10}$$

Therein, (xy) is chosen as the plane of the graphene sheet and (xz) as the plane of incidence (see Fig. 4 (a)). It follows that the PDE requires oblique incidence of radiation, since q_x vanishes for normal incidence. The linear photon drag current, described by T_1 and T_2 is present in both longitudinal ($\parallel x$) and transverse ($\parallel y$) directions. By contrast, the circular photon drag current being sensitive to the degree of circular polarization, P_{circ}, and described by $\tilde{T}_1$ is present only in transverse direction. The equations reflect the main features of the PDE: i) the current is coupled to the presence of an in-plane component of the photon wavevector q_x and ii) the current is proportional to the squared amplitude of the radiation's electric field $\boldsymbol{E}(\boldsymbol{r}, t)$. Here it's worth

mentioning that any reduction of the symmetry does not change the general form of Eqs. (9) and (10).

2.3.2 The photogalvanic effect

While the PDE is related to the linear coupling of the photon wavevector to the symmetric part of the conductivity tensor in Eq. (8), also its asymmetric part, $\sigma^{(2)}_{\alpha\beta\gamma}(\omega, \boldsymbol{q} = 0)$, may lead to the generation of a *dc* current. The related phenomena are the so called photogalvanic effects and are possible in noncentrosymmetric media only, such as e. g. graphene on a substrate, and are forbidden in perfectly symmetric systems like pristine graphene. Similarly to the PDE, the PGE was observed as early as the 1950's, but was correctly identified as a new phenomena in 1974 [39]. Up to now, linear and circular PGE have been studied in e. g., bulk materials, Si-MOSFETs and quantum wells (for review see [19, 20]). Phenomenologically, for the C_{6v} point group symmetry, which is representative for graphene on a substrate, and the same experimental geometry as considered above the current density can be written as [29]:

$$j_x = \chi_l \frac{E_x E_z^* + E_x^* E_z}{2}, \tag{11}$$

$$j_y = \chi_l \frac{E_y E_z^* + E_y^* E_z}{2} + \chi_c P_{circ} \hat{e}_x (|E_x|^2 + |E_y|^2). \tag{12}$$

Therein, χ_l (χ_c) describes the linear (circular) PGE. It turns out that the polarization dependence is similar to that of the PDE. The basic difference is that the PGE requires a z - component of the radiation's electric field instead of an in-plane wavevector component, restricting it's observation to oblique incidence as well. As a consequence, both effects are hard to distinguish from each other concerning their dependencies on the radiation's polarization state and the angle of incidence. The observation of the photogalvanic effect in graphene is most likely under conditions where the photon drag effect is reduced, e. g. at high radiation frequencies [29].

Microscopically, in the quantum frequency range the *dc* current driven by the PGE results from a quantum interference of two processes: i) Drude-like indirect optical transitions, described by the transition matrix element $M^{(1)}_{\boldsymbol{k}_f, \boldsymbol{k}_i}$,

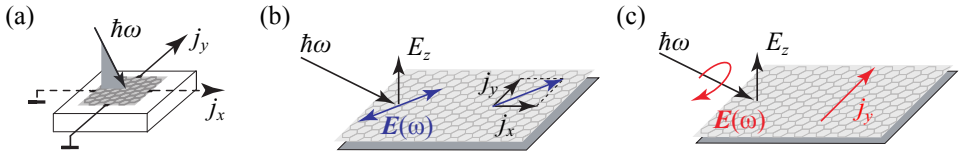

Figure 5: (a) experimental geometry of Eq. (11) and (12); contributions to j_x and j_y due to the linear (b) and circular (c) photogalvanic effects.

which are linear in $\boldsymbol{k}$ and ii) indirect intraband transitions with intermediate states in distant bands represented by $M^{(2)}_{\boldsymbol{k}_f,\boldsymbol{k}_i}$, which are almost independent of $\boldsymbol{k}$. The scheme of possible pathways of transitions is shown in Fig. 6 for parabolic bands of a Si-MOSFET (a) and the linear dispersion of graphene (b). A transition from an initial $\boldsymbol{k}_i$ to a final $\boldsymbol{k}_f$ electronic state is possible only due to the interference of both effects. The total transition rate is given by [40]:

$$W_{\boldsymbol{k}_f,\boldsymbol{k}_i} \propto |M^{(1)}_{\boldsymbol{k}_f,\boldsymbol{k}_i} + M^{(2)}_{\boldsymbol{k}_f,\boldsymbol{k}_i}|^2 = |M^{(1)}_{\boldsymbol{k}_f,\boldsymbol{k}_i}|^2 + |M^{(2)}_{\boldsymbol{k}_f,\boldsymbol{k}_i}|^2 + Re[M^{(1)}_{\boldsymbol{k}_f,\boldsymbol{k}_i} M^{(2)}_{\boldsymbol{k}_f,\boldsymbol{k}_i}]. \tag{13}$$

Herein, only the last term, $Re[M^{(1)}_{\boldsymbol{k}_f,\boldsymbol{k}_i} M^{(2)}_{\boldsymbol{k}_f,\boldsymbol{k}_i}]$, which describes the quantum interference, is linear in $\boldsymbol{k}$. The first term is an even function of the wave vector, whereas the second term is independent of $\boldsymbol{k}$. Hence, only the interference of both processes results in an imbalance of the carrier distribution in the $\boldsymbol{k}$-space and thus, in a *dc* photocurrent.

Considering graphene, the distant energy bands necessary for the interference are formed from σ-orbitals. It was shown that σ-orbitals form a deep valence band which is separated from the π-orbital valence band by roughly 10 eV [41]. Consequently, the PGE in graphene arises due to the interference of two transitions: i) Drude-like intraband transitions similar to that presented in Fig. 3 (b) and ii) indirect interband transitions via virtual states in the distant energy band (see Fig. 6 (c)).

Since it was shown in Ref. [30] that $M^{(1)}$ and $M^{(2)}$ have different parity under $z \to -z$ reflection, the interference restricts itself to a system where the $z \to -z$ symmetry is broken. As a consequence, in pristine graphene the PGE is expected to be absent. However, if graphene has lost its spatial symmetry

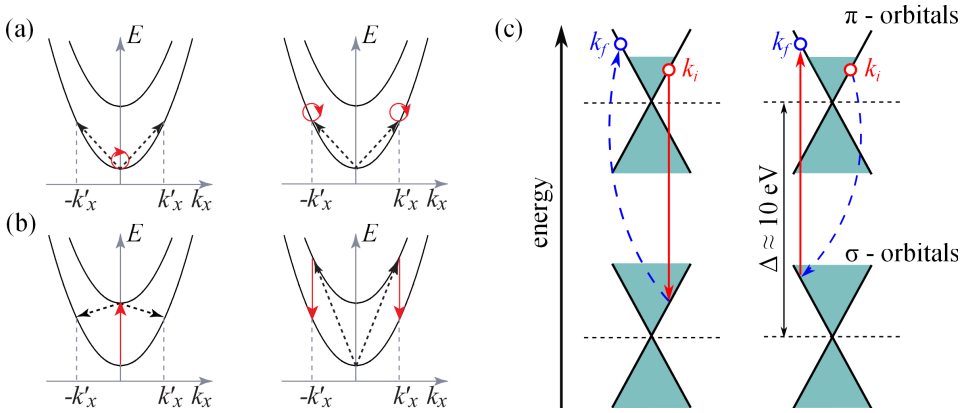

Figure 6: Pathways of intraband (a) and interband (b) transitions in conventional semiconductors; (c) indirect intraband transitions in graphene via intermediate states in distant bands.

with respect to $\pm z$, a *dc* photocurrent can appear which is proportional to the squared amplitude of the radiation's electric field. The lack of spatial symmetry is often discussed in terms of structure inversion asymmetry (SIA). The perfect honeycomb lattice with its flatness suffers a lack of SIA. However, if graphene is synthesized on a substrate or in the presence of adatoms, ripples, edges, etc., the system looses it's symmetry and the PGE is allowed.

2.3.3 The magnetic field induced photogalvanic effect

Besides the photon drag and photogalvanic effect, which require either an in-plane momentum or a normal-to-plane electric field component, also a class of second order photoelectric effects was discovered which are related to an in-plane magnetic field known as the magnetic field induced photogalvanic effect (MPGE) [42]. Apart from microscopic details, phenomenologically the current density within the linear approximation in the magnetic field strength $\boldsymbol{B}$ can be written as:

$$j_\alpha = \sum_{\beta\gamma\mu} \Phi_{\alpha\beta\gamma\mu} B_\beta \frac{\left(E_\gamma E_\mu^* + E_\gamma^* E_\mu\right)}{2} + \sum_{\beta\gamma} \chi_{\alpha\beta\gamma} B_\beta \hat{e}_\gamma E_0^2 P_{circ}. \tag{14}$$

Herein, Φ is a fourth rank pseudo-tensor which is symmetric with respect to γ and μ describing contributions to the *dc* current being sensitive to linearly

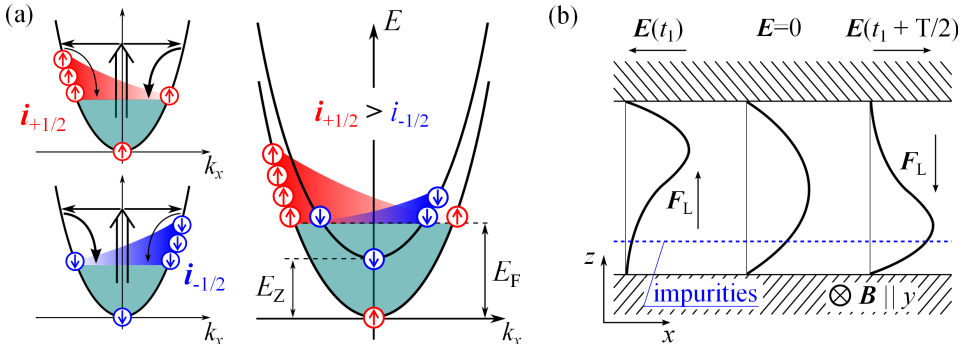

Figure 7: Microscopic mechanism of the MPGE caused by (a) spin-dependent scattering in Zeeman split spin-subbands (b) a diamagnetic shift of the electron wavefunction in an asymmetric QW.

polarized radiation. The second term of Eq. (14) contains the regular third-rank tensor $\chi_{\alpha\beta\gamma}$ describing contributions due to circularly polarized radiation. Depending on the point group symmetry of the studied system, Φ and χ need to be analyzed in terms of symmetry arguments as done above for the PDE and the PGE in order to transform Eq. (14) into Cartesian coordinates and to study the direction of j_α, as well as its dependence on the radiation's polarization state.

The most characteristic feature of the MPGE is the linear dependence of the current density on the in-plane magnetic field $\boldsymbol{B}$. Numerous microscopic mechanisms depicting the influence of the magnetic field have been discovered. All of them require asymmetric carrier scattering with respect to $\pm\boldsymbol{k}$ in order to convert THz radiation into a *dc* current. The asymmetric scattering, described by the scattering matrix element $W_{\boldsymbol{k}_f,\boldsymbol{k}_i}$, can be caused for instance by spin-related phenomena [43] or by the direct influence of the in-plane magnetic field onto the electron orbitals which is often discussed in terms of a diamagnetic shift [44]. In the following, these two mechanisms are introduced.

Spin-related phenomena: In systems with strong spin-orbit coupling, the scattering matrix element $W_{kk'}$ looks as follows [45]

$$W_{\boldsymbol{k}_f,\boldsymbol{k}_i} = W_0 + \sum_{\alpha\beta} w_{\alpha\beta}\sigma_\alpha(\boldsymbol{k}_i + \boldsymbol{k}_f), \tag{15}$$

where W_0 describes conventional symmetric carrier scattering, the second-rank pseudo tensor $w_{\alpha\beta}$ represents the asymmetric spin-dependent scattering and

σ_α is a Pauli-matrix component. The model of the *dc* current generation is depicted in Fig. 7 (a) for a spin degenerated parabolic dispersion and Drude absorption. The linear coupling between spin (σ) and momentum ($\boldsymbol{k}_f, \boldsymbol{k}_i$) leads to spin dependent scattering within spin-up and spin-down subbands and results in asymmetric population of each subband with respect to $\pm k$. This spin accumulation can be seen as two fluxes of spin polarized electrons $\boldsymbol{i}_{\pm 1/2}$ of opposite directions. However, the total electric current is zero. This mechanism is known as the zero bias spin separation [45].
In order to convert the spin fluxes into a spin-polarized electric current, the spin degeneracy need to be lifted, for instance by an in-plane magnetic field. The spin up and spin down subbands get energetically separated by the Zeeman energy $E_Z = g\mu_b B$ and thus, are unequally occupied. As a result, the spin fluxes $\boldsymbol{i}_{\pm 1/2}$ due to the asymmetric scattering do not cancel each other any more, leading to a directed *dc* electric current which is the result of the MPGE and linear in $\boldsymbol{B}$.

Diamagnetic contributions: In systems which are characterized by spatial inversion asymmetry (SIA), such as e.g. (001)-oriented QWs grown from zinc-blende-type compounds, $W_{\boldsymbol{k}_f,\boldsymbol{k}_i}$ is given by [44]

$$W_{\boldsymbol{k}_f,\boldsymbol{k}_i} = W_0 + \sum_{\alpha\beta} w_{\alpha\beta} B_\alpha (\boldsymbol{k}_i + \boldsymbol{k}_f), \tag{16}$$

where B_α is the applied in-plane magnetic field which couples linearly to the carrier momentum. A model system of the *dc* current generation due to a diamagnetic shift is depicted in Fig. 7 (b). The spatial asymmetry is given by a doping layer which is placed apart from the center of the QW reducing the symmetry of the system in z-direction. In this particular geometry the magnetic field is applied along the y-direction. If an alternating electric field supplied by THz radiation acts on the carriers, they start to move back and forth. The motion in the magnetic field results in a Lorentz force $\boldsymbol{F}_L$ which shifts right (left) moving electrons down (up). The up-shifted electrons scatter with lower probability than those which are down-shifted towards the δ layer. Thus, within a period of time of the electric field the carriers exhibit a directed motion leading to a *dc* current. Since the orbital shift is provided by

the Lorentz force $\boldsymbol{F}_L = (e/c)[\boldsymbol{v} \times \boldsymbol{B}]$, the current is typically linear in $\boldsymbol{B}$.

The specific mechanism which is responsible for the MPGE is determined by the system under study. In Ref. [46] spin related contributions to the MPGE were studied showing that spin-polarized currents can be strongly enhanced in QW systems with a high electron g-factor (InAs) or dilute magnetic semiconductors (DMS) where the exchange interaction between electrons and paramagnetic ions causes an additional contribution to the Zeeman energy known as the giant Zeeman splitting. By contrast, in Ref. [47] it was shown that also the diamagnetic shift can yield a significant contribution to the MPGE in samples which are characterized by a strong structure inversion asymmetry. The magnetic field induced photogalvanic effects have proven to be a powerful tool to study semiconductor heterostructures, but so far, these effects were not observed in graphene.

3 Experimental methods

This chapter is devoted to the experimental methods required for studies of photoelectric phenomena in graphene. At first, the generation of THz radiation by optically pumped molecular THz lasers and free electron lasers (FEL) is presented. Therefore, the underlying effects are explained and the buildup of the devices is shown. Subsequently, the description of the radiation's polarization state by the Stoke's parameters and techniques allowing their manipulation are presented. This is followed by the description of the experimental setups where the used optical components, the measurement techniques, and the calibration of the laser systems and - beams are discussed. Finally, the studied samples are presented. Two groups of samples are investigated in the framework of this thesis and hence, their production and preparation methods are explained briefly. Sample parameters which are of importance to explain experimental results are introduced at the end of this chapter.

3.1 Sources of high-power THz radiation

The photoelectric phenomena which are in the focus of this thesis are the result of the light-matter coupling in response to radiation with frequencies ranging from around 100 GHz up to some tens of THz. The corresponding photon energies are roughly situated between 1 and 100 meV. Nowadays, a vast amount of sources of coherent radiation for this range of the electromagnetic spectrum is available. Two sources of high-power THz radiation were chosen for the experiments: i) the optically pumped molecular THz laser [48] providing discrete laser lines in the THz range and output powers of tens of kW and ii) the free electron laser [49], which offers an almost continuously tunable output spectrum from the near- to the far- infrared region. Both sources of THz radiation have proven as powerful tools to study photoelectric phenomena [19]. In the following, the used radiation sources and the basic principles leading to coherent emission of THz radiation are briefly introduced.

3.1.1 Optically pumped molecular THz lasers

The emission of IR/THz laser radiation from molecular transitions was realized in the mid of the 1960s with the development of HCN and H_2O lasers [50, 51]. The first optically pumped molecular THz laser was realized in 1969 for continuous wave (*cw*) operation [48] and in 1974 extended to pulsed operation [52]. The scheme of the optical transitions leading to population inversion in a molecule is sketched in Fig. 8 (a). Two vibrational levels ν_0 and ν_1 of different energies are split up into various rotational levels ($E_{rot} << E_{vib}$) with angular momentum J and K being it's projection onto the symmetry axis of the molecule. The typical energy separation of the rotational levels in molecules is smaller than $k_BT \approx 25$ meV and hence, corresponds to THz photon energies. By optical pumping with a CO_2 laser providing laser lines between approximately 9.2 and 11.2 μm ($E_{ph} \approx 4k_BT$) [53] rotational levels in the higher energetic vibrational state ν_1 are excited leading to population inversion in both vibrational bands. This population inversion relaxes by emitting photons with energies within the THz range (see arrows in Fig. 8 (a)).

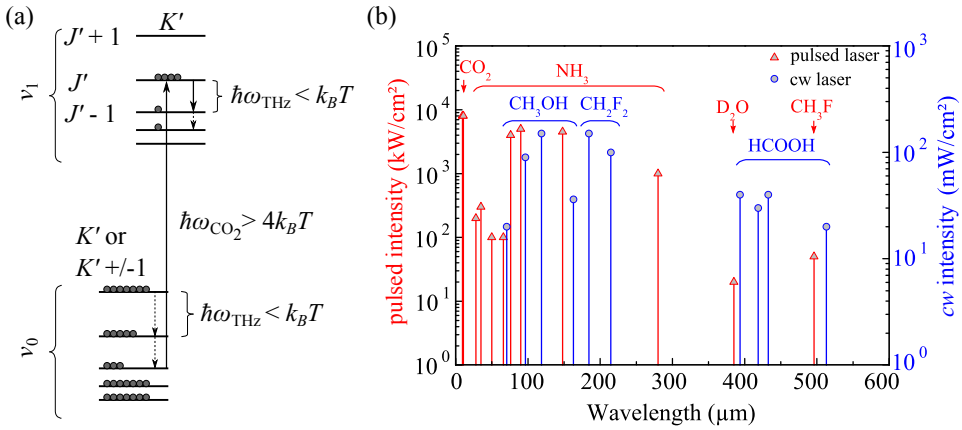

Figure 8: (a) Optical transitions in a molecule between vibrational states ν_1 and ν_2 which are split up into rotational levels: resonant pumping leads to population inversion between rotational states in both vibrational levels and to emission of THz radiation. (b) available laser lines for pulsed (red) and *cw* (blue) operations together with corresponding output intensities.

With that principle, plenty of resonant transitions can be achieved by the choice of the molecule and the variation of the pump frequency. Moreover, in the case of high pump power ($P_{pump} \approx$ MW) additional laser lines may appear due to the level broadening in the presence of a high electric field [54, 55]. In addition, assisted by stimulated Raman scattering molecular levels can be excited which are distant from the excitation energy depending on the excitation frequency and the gas pressure of the active media [19]. A summary of all laser lines available for the experiments is presented in Fig. 8 (b). It indicates that the optically pumped molecular THz lasers cover the spectral range between 0.6 and 30 THz with several discrete laser lines.

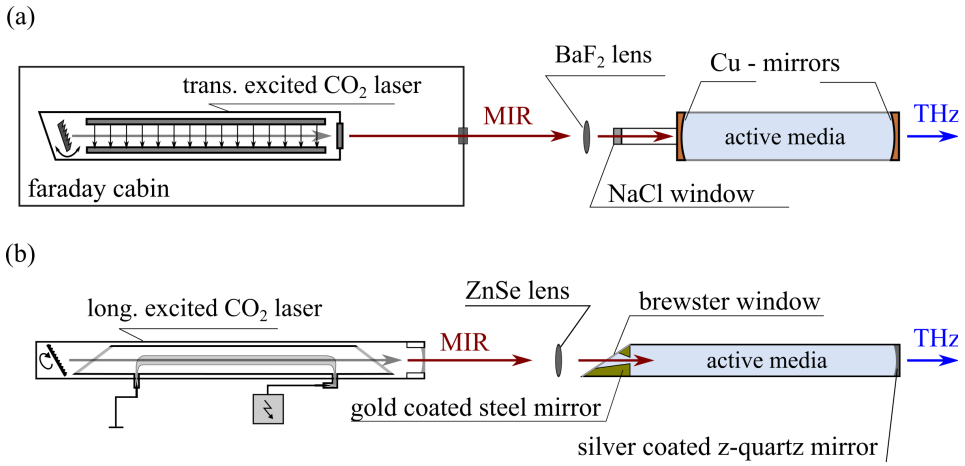

Figure 9: Schemes of (a) pulsed and (b) *cw* optically pumped molecular THz lasers.

Depending on the pump source, either *cw* or pulsed laser radiation can be generated. Schemes of both types of molecular lasers are depicted in Fig. 9. To generate pulsed THz radiation a pulsed transversely excited (TEA) CO_2 laser [56, 57] serves as a pump source providing pulses with approximately 100 ns duration and powers in the order of tens of MW. With a BaF_2 lens the pulses are coupled through a NaCl window into a resonator containing the active media which is built up of a glass tube and two spherical Cu mirrors at each end. The resulting THz pulses are coupled via a TPX window into the free space. The THz pulses have the same temporal shape as the excitation pulses and the typical output power is in the order of tens of kW.

To achieve *cw* operation, MIR radiation from a longitudinally excited CO_2 laser [58] is coupled through a ZnSe Brewster window into the THz resonator by a ZnSe lens. Here, a gold-coated steel mirror and a semi-transparent silver coated z-quartz mirror form the resonator of the laser. The output power which can be achieved with the *cw* laser is typically in the order of tens of mW. Both types of molecular THz lasers have proven as a powerful tool to study the nonlinear photoelectric phenomena in graphene [28, 30] and were used for the majority of the experiments presented in this thesis.

3.1.2 The free electron laser FELIX

Another source of coherent THz radiation is the free electron laser [59–61]. The emission of radiation results from relativistic electrons which oscillate in a magnetic field.

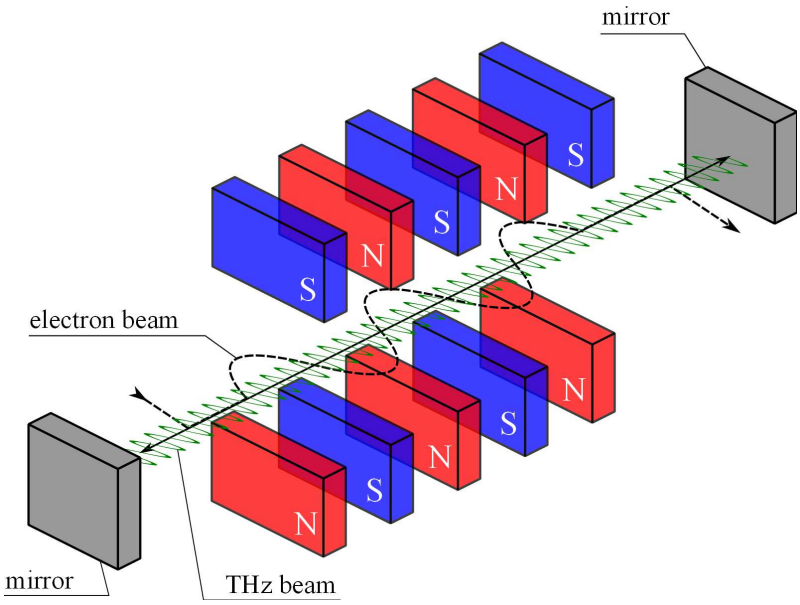

Figure 10: Scheme of a FEL: an electron beam oscillates in a perpendicular magnetic field of a Wiggler magnet array (dashed line) and emits THz radiation.

The scheme of a FEL is depicted in Fig. 10. A beam of relativistic electrons ($v \approx c$) is coupled into an alternating magnetic field of the so called Wiggler

magnet array. The electrons follow an oscillating trajectory with a periodicity given by the Wiggler period λ_w due to the action of the magnets. This electron oscillations lead to the emission of radiation. The determination of the radiation's wavelength λ can be found e. g. in Ref. [62] and follows to:

$$\lambda = \frac{\lambda_w}{2\gamma^2}(1 + K_w^2/2), \tag{17}$$

including the relativistic correction $\gamma = \left(1 - (v/c)^2\right)^{-1/2}$ and the Wiggler strength $K_w = eB_w\lambda_w/2\pi m_0 c^2$. Consequently, the laser wavelength can be tuned by the Wiggler periodicity λ_w, the magnetic field strength, or the kinetic energy of the electron beam. The radiation pattern is almost perfectly directed in the direction of motion of the electron beam [63]. A microbunching process resulting from the interaction of the relativistic electrons with the electromagnetic wave leads to the emission of coherent radiation [53].

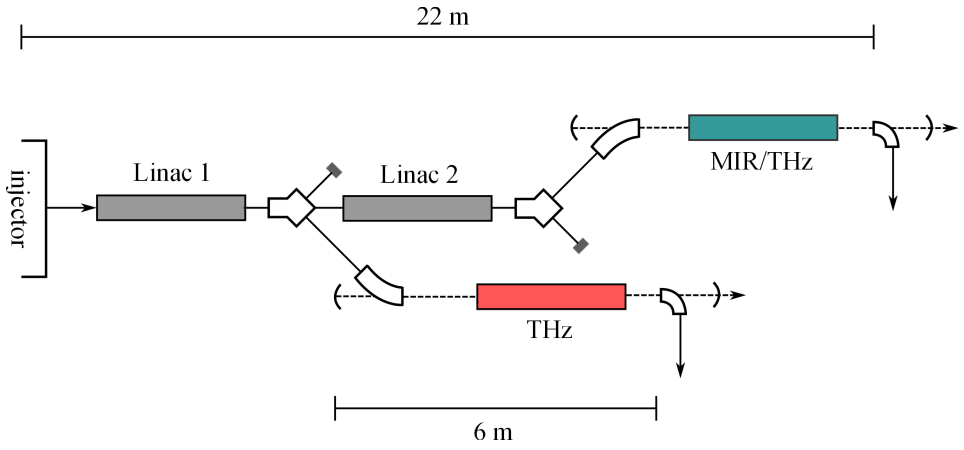

Figure 11: Outline and dimensions of the free electron laser FELIX.

For the experiments, the free electron laser facility FELIX [64] situated at the FOM Institute Rijnhuizen in The Netherlands, was chosen. FELIX was built in 1999 and consists of two FEL lasers covering the total frequency range from 4.5 up to 250 μm. A scheme of the laser facility is shown in Fig. 11. The laser consists of an electron injector and two radio frequency linear accelerators (linacs). The first linac provides electron beams with energies up to 25 MeV, the second one delivers beams up to 50 MeV. Wiggler magnet arrays are connected after both the first and the second accelerator yielding radiation

ranging from 5 to 30 μm and from 25 to 250 μm, respectively. The output power can be tuned from 0.5 up to 100 MW within a picosecond micropulse and the overall degree of linear polarization is $> 99\%$ for the FEL radiation. The tunability in a wide frequency range and the high output power makes the free electron laser attractive for experiments on nonlinear photoelectric phenomena in graphene.

3.2 Variation of the light's polarization state

As discussed in the previous chapter, the photoelectric phenomena under study show complex dependencies on the radiation's polarization state. Both linearly and circularly polarized radiations may result in a directed electric current. As mentioned above, THz laser radiation is almost perfectly linearly polarized. Therefore, it is inevitable to manipulate the polarization state of the THz radiation. In this section, at the beginning, the description of the polarization state by the Stokes parameters [65] is presented. Only this formalism yields a full description because it includes unpolarized radiation states as well. Afterwards, experimental methods to vary the radiation's polarization state are discussed.

3.2.1 The Stokes parameters

The Stokes parameters are a set of four values which fully describe the polarization state of electromagnetic radiation. A method to introduce the parameters is shown in Fig. 12 (a-c) considering four linear polarizers aligned along x, y, $+45°$ and -45° and two filters being sensitive to the intensity of either left- or right handed circularly polarized radiation, respectively.

The transmitted intensity I of a laser beam through the six filters defines the Stokes parameters as follows:

$$S_0 = I_x + I_y, \tag{18}$$

$$S_1 = I_x - I_y, \tag{19}$$

$$S_2 = I_{+45} - I_{-45}, \tag{20}$$

$$S_3 = I_{right} - I_{left}. \tag{21}$$

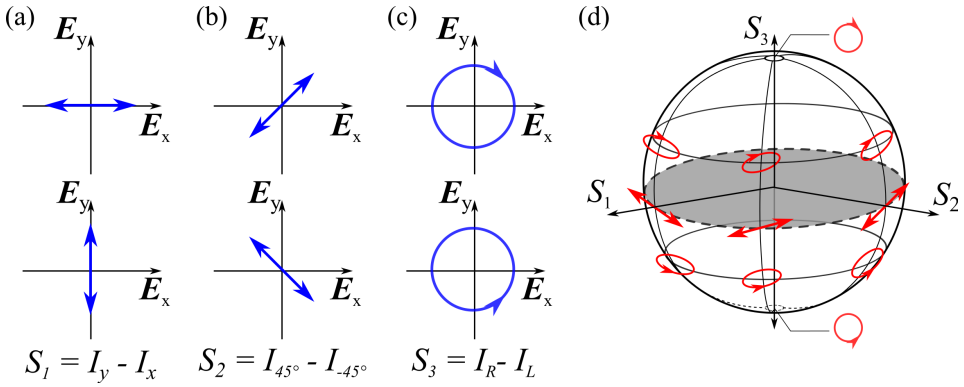

Figure 12: Set of vectors describing the second (a), third (b) and fourth (c) Stokes parameter. (d) Poincaré sphere describing all possible polarization states on its surface.

The first Stokes parameter, S_0, describes the light's total intensity I. The second, S_1, and third parameter, S_2, define the state of linear polarization. In detail, S_1 indicates whether the polarization is primarily oriented along the x- or y-direction. S_2 reveals the components which are aligned in between. The fourth parameter, S_3, yields whether the polarization state has any elliptically or even circularly polarized components and vanishes if the radiation is purely linearly polarized. Instead of intensity, also the corresponding electric field components can be used for the description [65]:

$$S_0 = E_x E_x^* + E_y E_y^*, \tag{22}$$
$$S_1 = E_x E_x^* - E_y E_y^*, \tag{23}$$
$$S_2 = E_x E_y^* + E_y E_x^*, \tag{24}$$
$$S_3 = i(E_x E_y^* - E_y E_x^*). \tag{25}$$

Below will be shown that this presentation allows one to recalculate the Stokes parameters into experimentally available parameters such as rotational angles of quarter- and half-wave plates. By choosing S_{1-3} as the axes of a three-dimensional coordinate system, each polarization state can be described by a point on the surface of the 3D sphere (see Fig. 12 (d)). Linearly polarized radiation states are situated in the S_1-S_2 plane of the surface. Circularly polarized states are located at the poles ($\pm|S_3|$) of the sphere and in between the elliptically polarized radiation states can be found. This sphere is known as

the Poincaré sphere [66]. In order to describe the full polarization state the parameters are normalized:

$$p = \frac{\sqrt{S_1^2 + S_2^2 + S_3^2}}{S_0}. \tag{26}$$

Thus, if p equals unity the wave is fully polarized whereas in the case it vanishes the radiation is completely unpolarized. In between the wave is partially polarized. Hence, the Stokes parameters deliver a full description of all possible polarization states. In the following methods to vary the Stokes parameters are presented.

3.2.2 Variation of the Stokes parameters by waveplates

A method to vary the radiation's polarization state is to use birefringent materials. In the THz range, x-cut crystal quartz can be applied for instance.

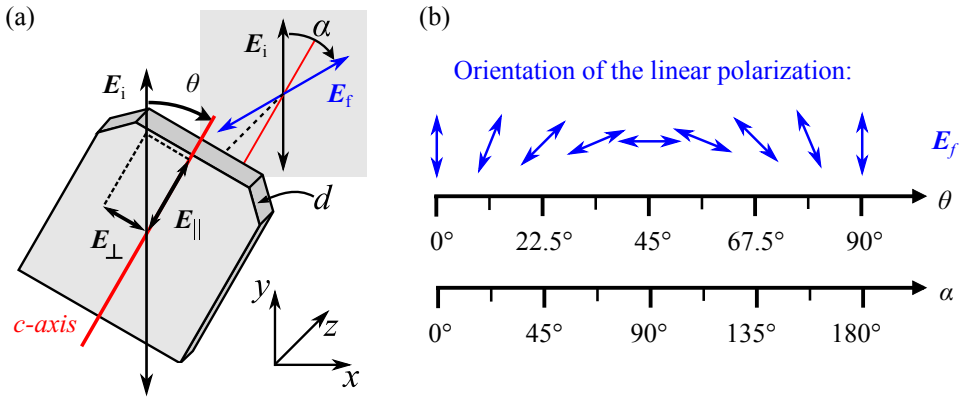

Figure 13: (a) Geometry of rotation of the linear polarization plane by a $\lambda/2$ plate and (b) the final polarization states with respect to the rotational angle θ of the plate. The final azimuth angle of the linearly polarized radiation is $\alpha = 2\theta$.

The scheme of the variation of a linearly polarized beam is depicted in Fig. 13. An incident electric field vector $\boldsymbol{E}_i$, which is rotated with respect to the crystallographic axis c of a quartz plate under a certain angle Θ, can be divided into

an ordinary beam $\boldsymbol{E}_{\perp}$, which is aligned perpendicularly to c, and an extraordinary beam $\boldsymbol{E}_{||}$, which is aligned parallel to the axis. For THz frequencies, the refractive index n of quartz is different for $\boldsymbol{E}_{\perp}$ and $\boldsymbol{E}_{||}$ and thus, both parts of the beam propagate with different velocities. The resulting phase shift $\Delta\phi$ between the beam components after passing a plate with a certain thickness d can be calculated as [67]:

$$\Delta\phi = (2\pi d)/\lambda \cdot \Delta n, \tag{27}$$

with $\Delta n = n_{eo} - n_o$ being the difference of refractive indices for the extraordinary (eo) and ordinary (o) beam, respectively. If $\Delta\phi$ equals $\pi/2$, the plate acts as quarter-wave / $\lambda/4$-plate and produces circularly polarized radiation. In the case $\Delta\phi = \pi$, the plate acts as a half-wave / $\lambda/2$-plate and rotates the polarization plane of linearly polarized radiation. Experimentally, the polarization state is varied by the rotation of quarter- or half-wave plates. In the case of a half-wave plate, this results in the rotation of an incident electric field vector $\boldsymbol{E}_i$ by an angle α which is twice the rotational angle θ of the plate (see Fig. 13). In the case of a quarter-wave plate, $\boldsymbol{E}_i$ is converted into an elliptically, or even circularly polarized state depending on the rotational angle φ (see Fig. 14).

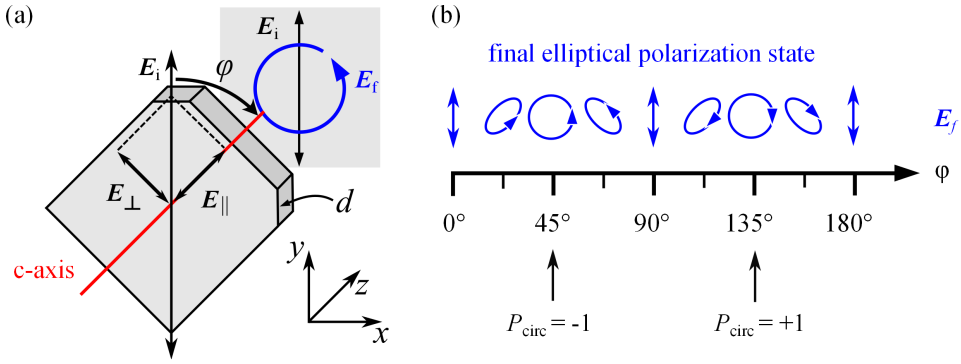

Figure 14: (a) Geometry of conversion of originally linearly into elliptically polarized radiation by a $\lambda/4$ plate and (b) the final polarization states with respect to the rotational angle φ of the plate.

Using Eqs. (22) to (25), the Stokes parameters for vertically polarized radiation ($\boldsymbol{E}_i||y$) and clockwise rotation of the wave plate can be rewritten in the form:

$$\frac{S_1}{S_0} = \frac{E_x E_x^* - E_y E_y^*}{|E|^2} = -\frac{\cos 4\varphi + 1}{2} = -\cos 2\alpha, \tag{28}$$

$$\frac{S_2}{S_0} = \frac{E_x E_y^* + E_y E_x^*}{|E|^2} = \frac{\sin 4\varphi}{2} = \sin 2\alpha, \tag{29}$$

$$\frac{S_3}{S_0} = \frac{i(E_x E_y^* - E_y E_x^*)}{|E|^2} = -\sin 2\varphi = -P_{circ}. \tag{30}$$

It can be seen that by using half-wave plates, the second and third parameter can be varied, whereas with the help of a quarter-wave plate also the fourth Stokes parameter, often denoted as the degree of circular polarization P_{circ}, can be manipulated. This conversion allows the direct identification of the Stokes parameters from polarization dependent measurements.

3.2.3 Refractive index of crystal quartz

For crystal quartz, Δn depends strongly on the frequency. Thus, the plates considered in the previous section show only a narrow bandwidth. In order to design plates for a certain frequency the spectral dependence of Δn is of importance.

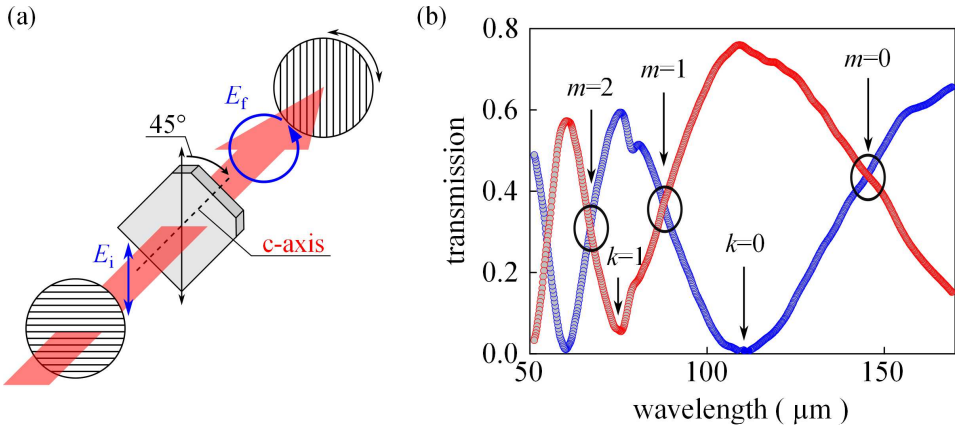

Figure 15: (a) Analysis of quartz plates with two polarizers in a FTIR spectrometer. (b) transmission spectra of a quartz plate for parallel (red) and crossed (blue) polarizers.

Different results where obtained in Refs. [68, 69] (see blue and red dots in Fig. 16). In precedent experiments to the thesis, the spectral dependence of Δn was investigated with a Fourier Transform Infrared (FTIR) spectrometer. The scheme of these experiments is seen in Fig. 15(a). Plates of different thicknesses d were mounted between two polarizers. The first one ensures that solely linearly polarized radiation is shined on the quartz plates. The plate was rotated in a way that the final angle between the crystal axis c with respect to the linearly polarized radiation achieved 45°. A full spectra were recorded for two orientations of the second polarizer: i) in parallel and ii) perpendicular with respect to the first one.

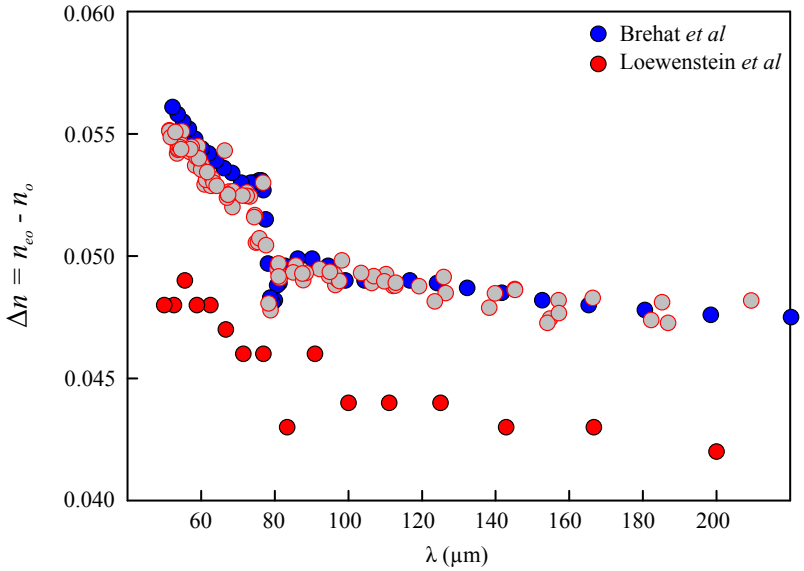

Figure 16: Spectral dependence of Δn (grey dots) compared to the data taken from Refs. [68] (red dots) and [69] (blue dots).

The spectra measured for one of the plates are presented in Fig. 15 (b) for parallel (red) and crossed (blue) polarizers. Crossing points of both curves, indicated by black circles, represent circularly polarized radiation where $\Delta\phi = (2m+1)\cdot\pi/2$. For these frequencies, the plate acts as $\lambda/4$-plate. Extrema indicate linearly polarized radiation. Here, $\Delta\phi = (2k+2)\cdot\pi/2$ and the plate acts as $\lambda/2$-plate. From these curves the values of Δn can be calculated using Eq. (27). The results of all available plates are shown in Fig. 16, indicated by the grey dots. The derived data fit well to that of Ref. [69]. With that

knowledge, $\lambda/4$- and $\lambda/2$-plates were designed for every desired frequency by matching the corresponding thickness of the plate. The plates were produced by the company TYDEX (194292 St.Peterburg, Russia).

3.2.4 Variation of the Stokes parameter by Fresnel rhomb

Another tool to vary the Stokes parameters is a Fresnel romb. It utilizes the principle that when light is shined on an interface under the critical angle θ_c of total internal reflection, there is a relative phase change of $\pi/4$ between the electric fields of s- and p-polarizations referring to the components polarized perpendicularly and parallel to the plane of incidence [70]. By aligning a series of interfaces under the conditions of total internal reflection, the phase shift between the two polarizations can be tuned at discretion. Utilizing this effect, broadband devices to vary the radiation's polarization state can be produced.

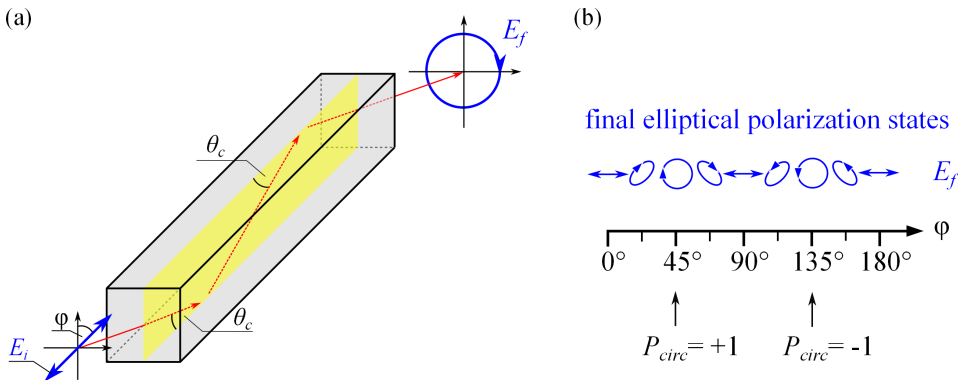

Figure 17: Basic principle of a quarter wave Fresnel rhomb (a) and final polarization states (b) for $\boldsymbol{E}_i$ aligned horizontally and clockwise rotation of the rhomb around its optical axis by an angle φ.

For the experiments, a ZnSe quarter-wave Fresnel rhomb from II-VI Inc. (375 Saxonburg Blvd., Saxonburg, PA 16056-9499, United States) was used. In Fig. 17 (a), the scheme of such a rhomb is sketched. Linearly polarized radiation entering the rhomb under $\varphi = 45°$ results in circularly polarized radiation. Here it's worth mentioning that in the experiments, $\boldsymbol{E}_i$ is aligned horizontally and the rhomb is rotated clockwise around φ. The resulting polarization states

for these conditions are shown in Fig. 17 (b). With that method, the Stokes parameters are varied in the same way as by rotating a quarter-wave plate.

3.3 Experimental Setups

After discussing the sources and optical components which are of interest for the photocurrent experiments, the experimental setups are presented next. The optically pumped molecular THz laser is located at the THz center in Regensburg, Germany and can be used at room, as well as at cryogenic temperatures. The FELIX free electron laser was situated at the FOM Rjihnhuizen, The Netherlands, but meanwhile has been transferred to Nijmegen. In similar quasi-optical setups photocurrent experiments have been performed. Both setups are introduced in this section.

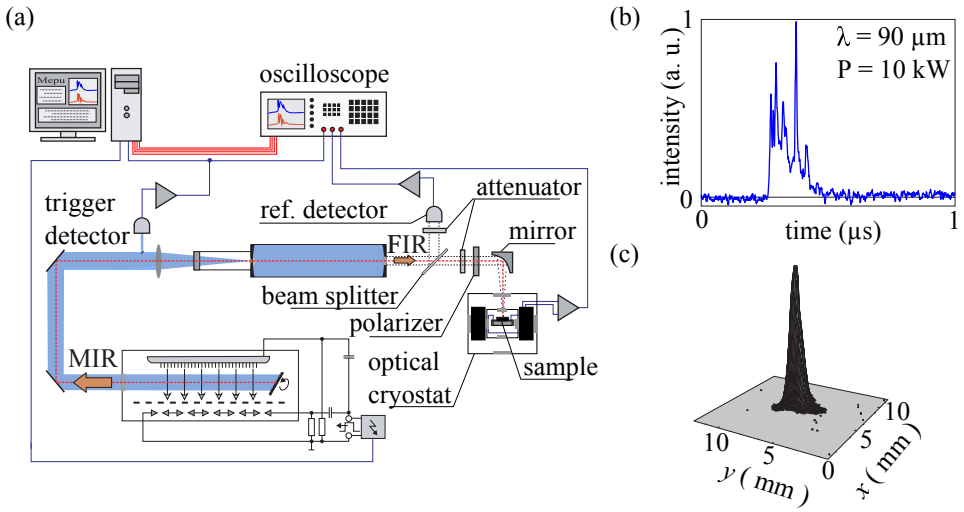

Figure 18: (a) Scheme of the setup used for experiments with a pulsed optically pumped molecular laser. (b) Time-resolved THz pulse detected with a photon drag detector and recorded with a GHz oscilloscope. (c) Spatial distribution of the focused THz beam recorded with a pyroelectric camera.

A typical setup for experiments with a pulsed optically pumped molecular THz laser is sketched in Fig. 18 (a). The computer triggers the pulsed TEA-CO_2 laser and collects the data from a GHz storage oscilloscope which is connected

by GPIB. A mid-infrared photon drag detector PD5M which is mounted in combination with a beam splitter after the CO_2 laser measures a reference pulse which is used to trigger the oscilloscope. A far-infrared photon drag detector PD5F is located together with a second beam splitter after the FIR resonator in order to monitor the power of the THz pulse. A time resolved THz pulse recorded with the GHz oscilloscope is plotted in Fig. 18 (b) for $\lambda = 90$ μm. Thin mylar layers are typically used as THz beam splitters and the final ratio between transmitted and reflected radiation depends on the thickness of the layer and the frequency [71]. The transmitted part of the THz radiation is used for photocurrent experiments. After the beam splitter, attenuators and polarizers are mounted before the radiation is focused on the sample with the help of parabolic gold mirrors of different focal lengths. Alternatively, the radiation can be coupled into an optical cryostat to measure photocurrents at liquid helium temperature and in presence of magnetic fields up $\pm$ 7 Tesla. The parabolic mirrors lead to almost Gaussian beam profiles (see Fig. 18 (c)) with typical full widths at half maximum in the order of 1 - 3 mm^2 depending on the focal length of the mirror. The beam profiles are recorded with a pyroelectric camera from Spiricon. In order to calibrate the beam stage with all components a second photon drag detector is mounted at the sample position and from the ratio of both PD5F signals the incident power at the sample can be calculated [19]. Finally, photocurrent signals are measured as voltage drop over 50 Ω load resistors and fed into low-noise 20 dB amplifiers with a typical bandwidth of 300 MHz. These signals are measured with the GHz oscilloscope and collected by the computer.

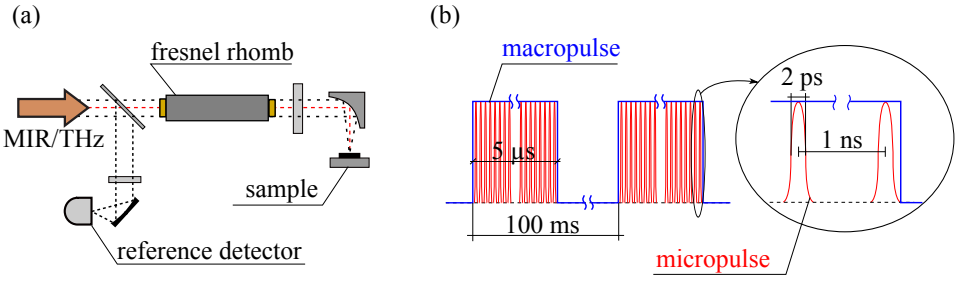

Figure 19: (a) beam stage used at FELIX. (b) shows time dependent structure of micro - (red lines) and macropulses (blue envelope).

At the FELIX the laser beam is guided from the resonators located in the basement of the institute to the laboratories. A scheme of the beam stage used in the laboratory can be seen in Fig. 19 (a). A KRS5 beam splitter in combination with a photon drag detector PD5M was used for power monitoring. Attenuators and a Fresnel rhomb were mounted afterwards and the transmitted radiation was focused onto the sample leading to beam profiles similar to that of the molecular THz laser. The time structure of the outcoupled radiation beam is depicted in Fig. 19 (b). Micropulses of approximately 2 ps duration separated by 1 ns in time form pulse trains or macropulses with durations up to 5 μs. These macropulses are separated by 100 ms in time from each other. At FELIX, only room temperature measurements were performed and the signals were measured via an amplifier with 20 MHz bandwidth. Both frequency and polarization of the laser radiation can be tuned by the measurement unit. The alignment of the electric field vector of the radiation is provided in three different orientations, that are horizontal, vertical, and 45° with respect to each other.

3.4 Graphene samples

In the final section of this chapter, the investigated graphene samples are introduced. Up to now, several techniques have been developed which allow the production of wafer-sized graphene samples. Among them are the epitaxial growth of graphene on silicon carbide (SiC) [72] and the chemical vapor deposition (CVD) method [73]. Both type of samples were used to study photoelectric phenomena and thus, their production- and characterization methods are briefly described.

Most of the epitaxial graphene samples (denoted as Epi-1 - Epi-6) under investigation are distributed from the group of Prof. Dr. Rositza Yakimova at the Linköping University, Sweden. The details of the growth process can be found in Ref. [74]. Also a sample grown in the group of Prof. Dr. Thomas Seyller at the University of Erlangen is investigated (Epi-7). The epitaxial growth of monolayer graphene can be done by annealing silicon carbide at $T \approx 2000\ ^{o}$C in argon atmosphere leading to the sublimation of SiC and recrystallization of carbon. Precise control of growth conditions, as well as careful selection

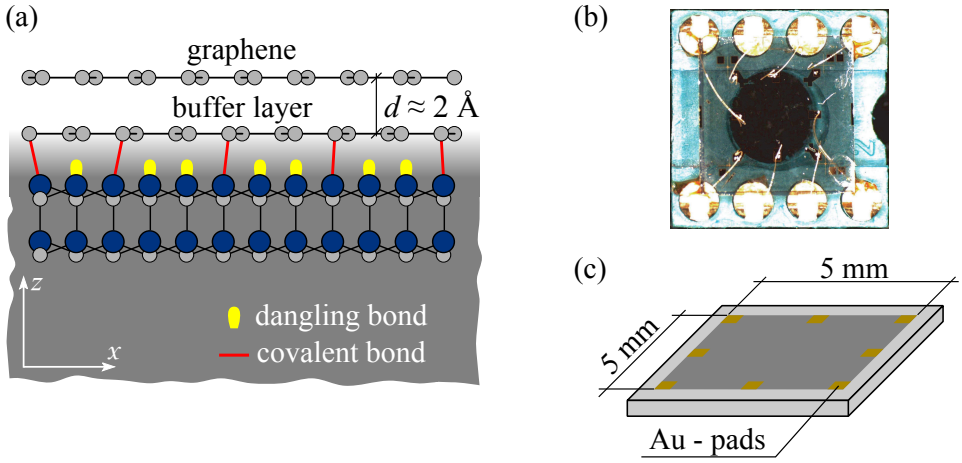

Figure 20: (a) Layer profile of epitaxial graphene; (b) picture of sample Epi-2 with bonding scheme; (c) dimensions and contact geometry of the samples.

of crystal-type, -face and -orientation are required for the growth of a single graphene layer. The underlying SiC is available in numerous polytypes [75] where in all of them the fundamental repeating unit is a tetrahedron formed by three silicon atoms sp^3 bonded to a carbon atom. The polytypes emerge due to different crystal lattices and stacking orders. The investigated samples were produced from 4H-SiC which assembles in a hexagonal crystal lattice and four basal planes within a unit cell following an ABCB stacking order. This polytype offers two surfaces, that are the carbon $(000\bar{1})$ and silicon (0001) faces where only the latter allows a manageable growth of monolayer graphene by silicon desorption. All investigated samples are grown on the Si-face, where a graphene-like layer is formed at the interface between graphene and SiC. This layer, known as the buffer-layer, has the same honeycomb lattice structure as the graphene layer but is partially covalently bonded to the substrate with some open bonds, denoted as dangling bonds, remaining (see Fig. 20 (a)). In contrast to the graphene layer, it is electrically inert with a band gap of approximately 0.3 eV [76].

For the investigation of photocurrents in graphene, squares with dimensions of 5×5 mm^2 were patterned using standard electron beam (e-beam) lithography and oxygen plasma etching (see Fig. 20 (c)). Metallic contacts on the periphery

sample	n (4K)	n (300K)	μ (4K)	μ (300K)	E_{F}(4K)	E_{F} (300K)
	[10^{12} cm^{-2}]		[cm^2/Vs]		[meV]	
Epi-1	3.8	3.4	1550	930	215	227
Epi-2	2.3	2.5	2800	1420	176	183
Epi-3	1.1	1.3	2760	1700	121	135
Epi-4	0.9	1.1	6150	2600	112	122
Epi-5	7.3	7.0	1350	910	314	308

Table 1: Carrier density n, mobility μ, and Fermi energy E_{F} of various epitaxial graphene samples at 4.2 K and room temperature.

of graphene were produced by straightforward deposition of Ti/Au (3/100 nm) through a lithographically defined mask, followed by lift-off. Samples Epi-1 - Epi-5 where encapsulated in a polymer film as described in Ref. [77], consisting of a spacer thin film of positive e-beam resist poly(methylmethacrylate-co-methacrylate acid), commercially known as PMMA/MMA [MMA (8.5) MAA, Microchem Corp.] followed by an active poly-methyl styrene-co-chloromethyl acrylate traded as ZEP520 polymer (Nippon Zeon Co. Ltd). For comparison, the surface of samples Epi-6 and Epi-7 remained unprotected and prone to uncontrolled contamination from the ambient atmosphere. Finally, the samples were glued onto chip carriers and electrically contacted by Au wires (see Fig. 20 (b)).

The sample out of Prof. Yakimova's group were characterized by the coworkers in the group of Prof. Dr. Sergey Kubatkin at the Chalmers University in Gothenburg, Sweden, in terms of carrier type, concentration and mobility using van der Pauw measurements at room temperature and $T = 4.2$ K, employing magnetic fields up to $B = \pm 5$ T (see Table 1). Most notably, all these samples were found to be n-doped due to the charge transfer from SiC [78]. The low temperature carrier (electron) concentration was found to be typically $\sim 10 - 15\%$ lower compared to its room temperature value, probably due to thermally excited carriers in the SiC substrate. The room temperature mobility of the large samples is typically smaller than that at low temperatures what can be attributed to phonon scattering [79]. The unprotected samples

showed a slow drift of carrier concentration and mobility on a time scale of months.

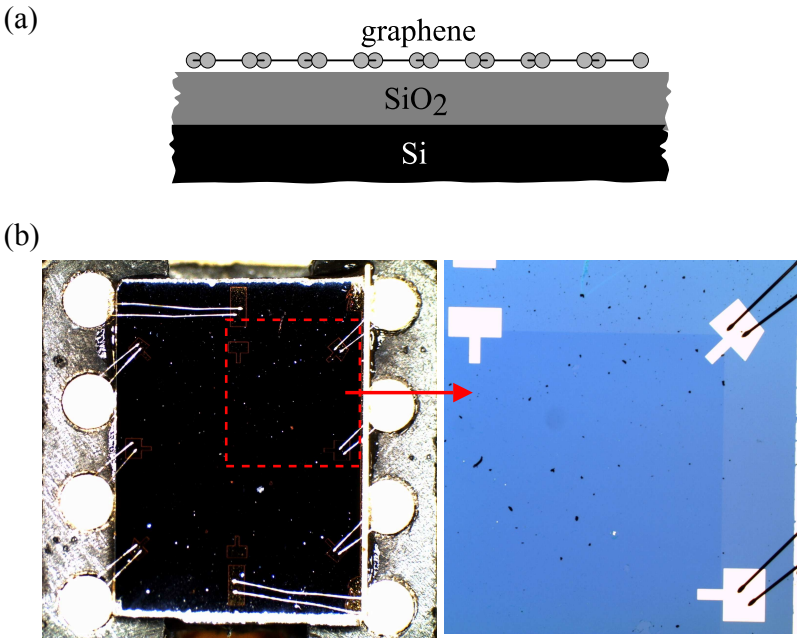

Figure 21: (a) Layer profile of CVD-grown graphene; (b) pictures of sample CVD-2.

CVD grown graphene samples were provided from two groups. One sample (CVD-1) was provided by Prof. Dr. Junichiro Kono and co-workers from the Rice University in Houston, United States. Details about the growth and transfer process of these samples can be found in the supplementary material of Ref. [80]. The resulting graphene layer was of 1.2×1.2 cm^2 and is deposited on a 300 nm SiO_2 insulating layer (see Fig. 21 (a)). For electrical measurements eight electrodes were defined in the corners and at the middle point of the sides of the square shaped graphene layer by e-beam deposition of 3 nm Ti and 80 nm Au trough a laser-cut shadow mask. Each of the electrodes had 200×200 μm^2 lateral dimension. Typical room temperature mobilities achievable with this method are, in accordance to our co-workers, between 500 to 750 cm^2 / Vs and hence, significantly lower as for epitaxial graphene.
A second CVD grown sample (CVD-2) was provided by the group of Prof. Dr. August Yurgens from the Chalmers University in Gothenburg, Sweden. This sample was produced in a similar growth process but is smaller in size (5 × 5

mm^2). A picture can be found in Fig. 21 (b). This sample was also glued on a chip carrier and mechanically bonded. The co-workers predicted a similar mobility as for sample CVD-1 from resistance measurements.

4 Magnetic quantum ratchet effect

After discussing the theoretical background and the experimental methods, in the following chapters the focus is set on the experimental observation of the photoelectric phenomena in graphene. In this particular chapter it is demonstrated that carriers in graphene, which is characterized by a spatial asymmetry, exhibit a directed motion when they are driven out of equilibrium by a periodic force in presence of an in-plane magnetic field. The chapter starts with the experimental observation of magnetic-field dependent photocurrents in various graphene samples in response to linearly - and circularly - polarized radiation. The investigation reveals that the current scales linearly with i) the in-plane magnetic field and ii) the squared amplitude of the radiation's electric field and hence, belongs to the class of magnetic field induced photogalvanic effect introduced in Section 2.3.3. Subsequently, a theoretical explanation for the magnetic field induced photocurrent is worked out. First, a model is presented showing that the current emerges solely if the graphene samples are characterized by a structure inversion asymmetry. The asymmetry results in non-equal transport properties of counter-propagating electrons in an in-plane magnetic field and gives rise to classify the current as a ratchet current [31]. The model is followed by a brief introduction of the microscopic developed by Sergey A. Tarasenko. Within a semiclassical formalism, the current is derived by solving the Boltzman kinetic transport equation assuming asymmetric carrier scattering in graphene. The results of first principles calculations done by Jaroslav Fabian and Martin Gmitra assuming hydrogen adatoms as a source for the asymmetry are briefly summarized and allow the estimation of the strength of the asymmetric scattering. Consequently, all experimental findings are compared to the developed theory and result in the discussion of the origin of the asymmetric carrier scattering under the experimental conditions. As it turns out, the magnetic quantum ratchet effect is direct noninvasive tool to quantify the structure inversion asymmetry in graphene.

4.1 THz photocurrents subjected to an in-plane magnetic field

The magnetic field induced photocurrents are studied in unbiased graphene samples under illumination with THz radiation from the pulsed molecular laser providing pulses of roughly 100 ns duration and discrete laser lines in the THz range (see Section 3.3). The samples are mounted in the optical cryostat in order to study the photocurrents in a wide temperature range. The current is measured perpendicular to the magnetic field B_y and the radiation is shined under normal incidence ($-z$ direction) on the sample.

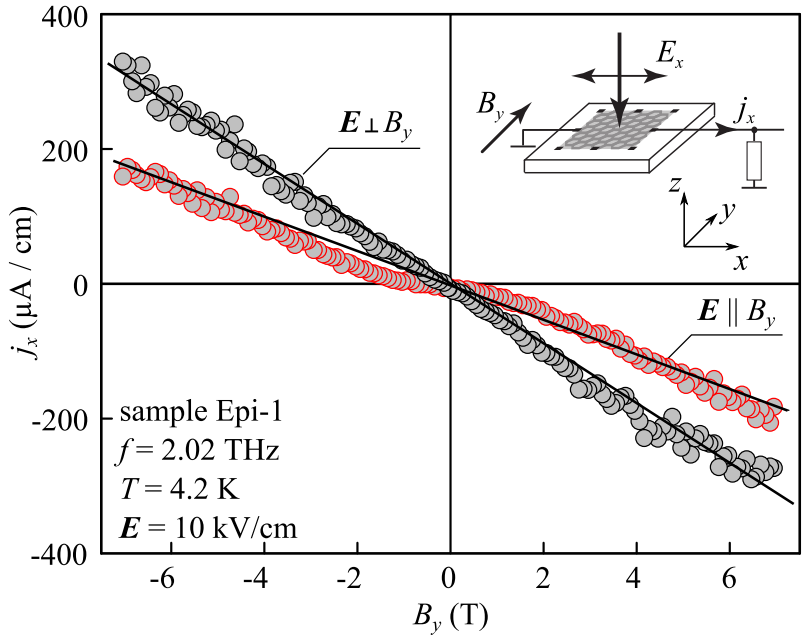

Figure 22: Photocurrent density j_x measured perpendicularly to the magnetic field B_y obtained by illuminating sample Epi-1 at 4.2 K with a radiation frequency of 2.02 THz. j_x is plotted versus B_y for an electric field of 10 kV/cm aligned in parallel (red) and perpendicular (black) to B_y. The experimental geometry is depicted in the inset.

First of all, by illumination without magnetic field under normal incidence of linearly polarized radiation no current is observed for most of the studied samples. This is in agreement with Eqs. (9) to (12) which yield that both, photon drag - and photogalvanic effects are absent for the point group symmetry

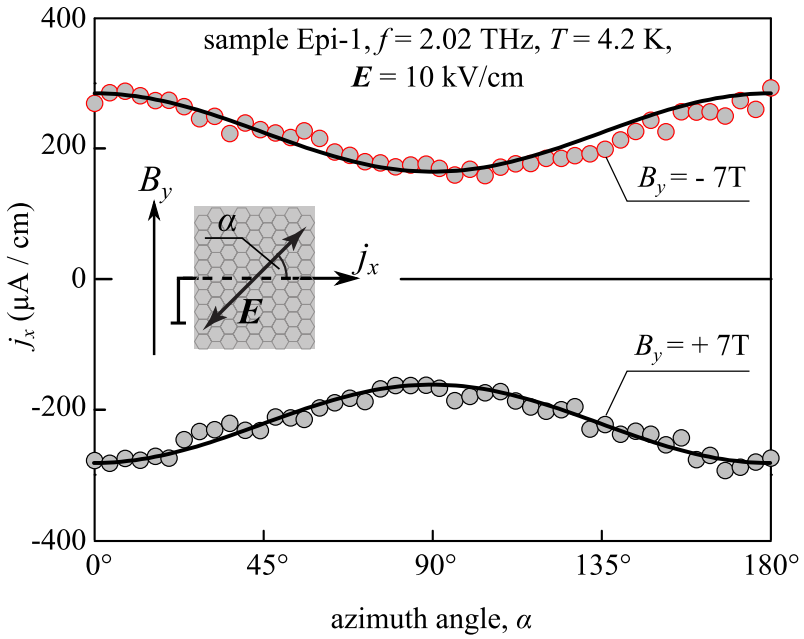

Figure 23: Perpendicular photocurrent j_x obtained by illuminating sample Epi-1 at 4.2 K, $f = 2.02$ THz and $E = 10$ kV/cm under variation of the azimuth angle α (see inset) of the radiation's electric field for $+/-7$ Tesla. The full lines are fits after Eq. (31).

C_{6v}. However, in some studied samples photocurrent signals appear even under normal incidence of radiation indicating that the symmetry of these samples is reduced. The focus is set on the samples which show no signal at normal incidence and zero magnetic field. A magnetic field dependence of the current density j_x, measured at 4.2 K in the epitaxial graphene sample Epi-1, obtained by illumination with pulsed radiation at a frequency of 2.02 THz is plotted in the main panel of Fig. 22 for an electric field amplitude of 10 kV/cm. It can be seen that by applying an in-plane magnetic field a photocurrent j_x is observed which scales linearly with $\boldsymbol{B}$. A reversion of the sign of the current is observed by switching the polarity of the magnetic field resulting in a symmetric dependence with respect to $\pm\boldsymbol{B}$. Moreover, the current is proportional to the squared amplitude of the radiation's electric field and the signals repeat the temporal shape of the excitation pulses very well (not shown). As it is indicated in Fig. 22, the current is observed for two alignments of the electric field, that is perpendicular (along x- direction, red symbols) and in parallel (along

y- direction, black symbols) to the magnetic field $\boldsymbol{B}$. For the two orientations of $\boldsymbol{E}$ the currents differ in magnitude.

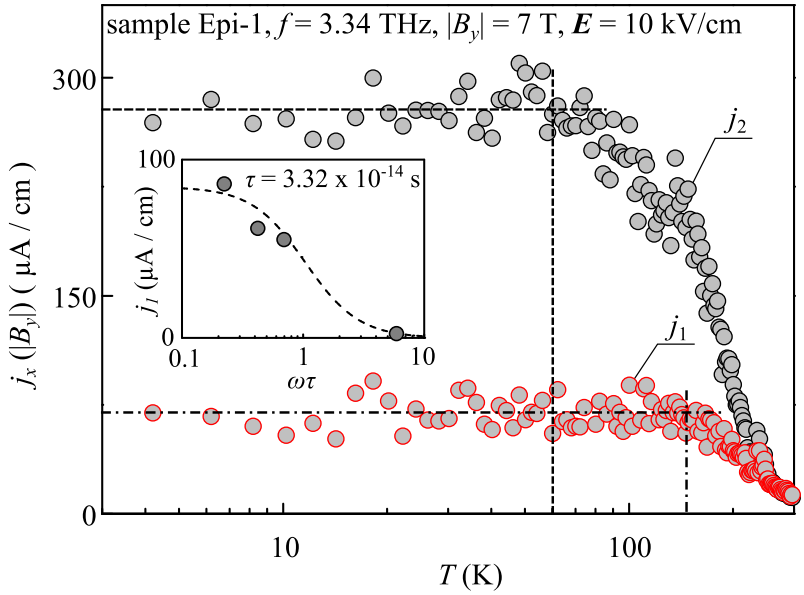

Figure 24: Temperature dependence of the polarization dependent (j_1) and - independent (j_2) photocurrent for $|B_y| = 7$ Tesla and $f = 3.34$ THz, measured by illuminating sample Epi-1. The inset shows the frequency dependence of j_1 for a momentum scattering time $\tau = 3.32 \times 10^{-14}$s. The dashed line is a guide for the eye, its description can be found in the main text.

The dependence of j_x measured in the same sample at $B_y = \pm 7$ T and T = 4.2 K upon variation of the alignment of the electric field $\boldsymbol{E}$ is shown in Fig. 23. The orientation of $\boldsymbol{E}$ is described by the azimuth angle α which is defined as the angle between the electric field vector and the x- axis. The plot shows that the current develops a maximum for α equal zero degree corresponding to $\boldsymbol{E} \perp B_y$ and oscillates with the second harmonic of the azimuth angle α. The overall dependence can be fitted after

$$j_x = j_1 \cos 2\alpha + j_2, \tag{31}$$

indicated by the full line in Fig. 23. Equation (31) demonstrates that j_x contains two contributions: i) a polarization dependent part of the current density, j_1, and ii) a polarization independent part, j_2, as well.

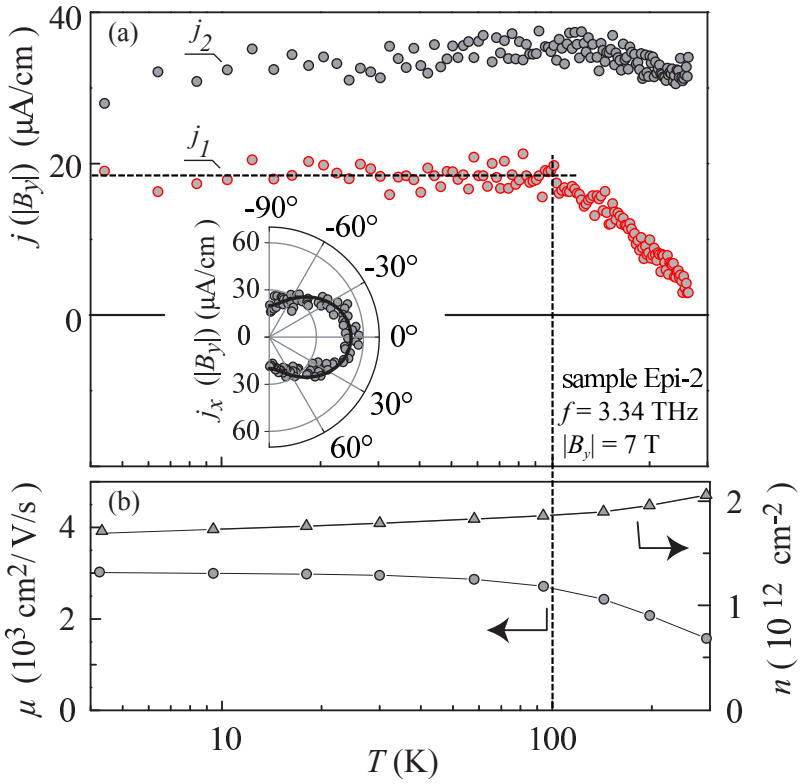

Figure 25: (a) Main panel shows temperature dependence of j_1 and $j_2$obtained by illuminating sample Epi-2 at $f = 3.34$ THz. Inset shows polarization dependence at 4.2 K and a fit after Eq. (31). (b) shows temperature dependence of carrier density n and mobility μ obtained by transport measurements.

Both parts of the current are studied in terms of their temperature dependence and the result is presented in Fig. 24. At low-temperatures, the polarization independent current j_2 is higher by a factor of four compared to the polarization dependent part j_1. It stays constant up to roughly 60 K and then decreases by an order in magnitude up to room temperature. By contrast, j_1 stays constant up to approximately 100 K and decreases to similar values as j_2 at room temperature. Besides the temperature dependence, j_1 shows also a dependence under variation of the excitation frequency. The inset in Fig. 24 reveals an overall decrease of j_1 with increasing frequency. At the highest radiation frequency, no polarization dependent current was observed. The dashed line serves as guide for the eye and is a fit after $\propto 1/(1 + (\omega\tau)^2)$.

A set of experimental data obtained by illuminating another epitaxial graphene sample Epi-2 is presented in Fig. 25. The polarization dependence of the current, measured at 4 K for ± 7 T, can be fitted by Eq. (31) as well showing a maximum for $\boldsymbol{E} \perp B_y$ corresponding to $\alpha = 0°$. Under variation of the temperature, j_1 stays constant up to approximately 100 K and decreases up to room temperature by an order in magnitude. Consequently, it shows almost identical behavior as observed in sample Epi-1. By contrast, the polarization independent current j_2 depends only weakly on the temperature and shows different behavior as in sample Epi-1. Additional temperature dependent Hall measurements, shown in Fig. 25 (b), reveal a smooth increase (decrease) of the carrier density (mobility) with increasing temperature.

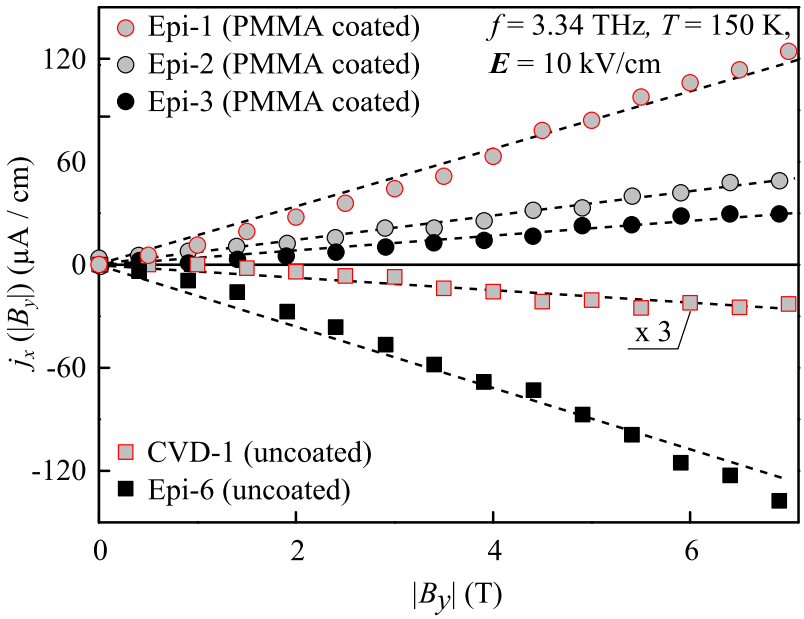

Figure 26: Magnetic field dependencies of j_x obtained for $\alpha = 0°$ in various samples for a laser frequency of 3.34 THz. The data were obtained at $T = 150$ K. The red squares are data obtained for sample CVD-1 and measured at 4.2 K. The curve is multiplied by a factor 3.

The magnetic field dependence of sample Epi-2 can be found in Fig. 26 together with that of other investigated samples. For all curves, the excitation frequency is 3.34 THz and the electric field is aligned perpendicularly to the magnetic field ($\alpha = 0°$). As a result, the samples Epi-1, Epi-2 and Epi-3 be-

ing encapsulated in a polymer have the same polarity but differ in magnitude. The uncoated epitaxial sample Epi-6 is of the same order of magnitude but of opposite polarity. The current observed in the uncoated sample CVD-1 grown by the chemical vapor deposition method showed only weak responsivity with a current which is approximately lower by a factor of 100 compared to the highest signals and could be observed only at low temperatures. All other curves were derived at 150 K. Consistently, different signs were observed for two different groups of samples. While the samples which are uncovered and their surface is sensitive to the environment exhibit a negative slope, the samples which are encapsulated in PMMA show a positive slope.

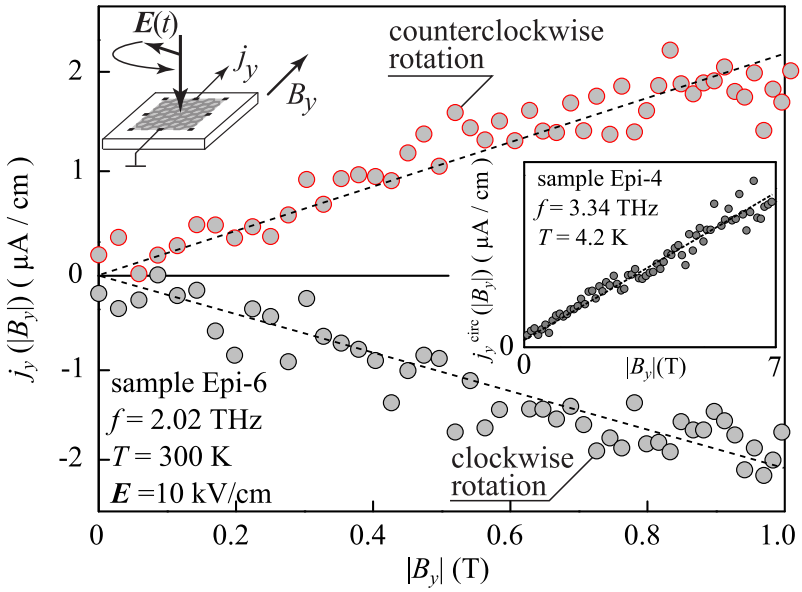

Figure 27: Parallel photocurrent j_y excited at room temperature and 2.02 THz in sample Epi-6 by circularly polarized radiation providing clockwise and counterclockwise rotating electric fields. The inset shows $j_y^{circ} = [j(\sigma_+) - j(\sigma_-)]/2$ measured in sample Epi-4 at 4.2 K by excitation with 3.34 THz.

Besides the sensitivity to linearly polarized radiation, also the illumination with circularly polarized radiation results in a photocurrent in the presence of an in-plane magnetic field. Figure 27 shows the magnetic field dependence of the photocurrent j_y in sample Epi-6, measured in parallel to the magnetic field B_y at room temperature for an excitation frequency equal to 2.02 THz.

For both right-handed (σ_+) and left-handed (σ_-) circularly polarized radiation providing clockwise - and anticlockwise rotating electric fields, a photocurrent is present which scales linearly with the magnetic field. A change of sign is observed by reversing the rotational direction of the electric field, in other terms by switching the radiation's helicity. A helicity dependent current was also observed in sample Epi-4 at 4.2 K and 3.34 THz. The inset in Fig 27 shows the linear dependence of j_y^{circ} describing the sensitivity to the radiation's helicity. However, the helicity dependent current vanishes at higher temperatures and lower excitation frequencies. In all other samples, a parallel photocurrent sensitive to the radiation's helicity was not observed.

4.2 Microscopic model and theory

After the observation of the magnetic field induced photocurrents in graphene its microscopic mechanism is worked out. Following Section 2.3.3 a possible microscopic origin of the MPGE can be caused by spin related phenomena. However, due to the electrons low-effective mass the spin-orbit coupling is vanishingly weak in graphene and the spin-dependent origin of the photocurrent becomes ineffective. The second mechanism described in there considers a shift of the electron orbitals due to the Lorentz force which results in asymmetric electron scattering in quantum wells with structure inversion asymmetry. As shown in Chapter 2.1, graphene is highly symmetric and the confinement in a graphene sheet is nearly two-dimensional. On a first glance, also orbital mechanism leading to a magnetic field induced photocurrent are expected to be weak. The situation changes when graphene loses its spatial symmetry due to the presence of a substrate and/or adatoms. Under these circumstances, a novel phenomenon denoted as the magnetic quantum ratchet effect may appear and lead to the directed current in the in-plane magnetic field.
The physics of the magnetic quantum ratchet current is depicted in Fig. 28. THz radiation, incident normal to the graphene plane, provides an *ac* electric field which moves the carriers in the graphene sheet back and forth. At a certain time t_1, where the electric field points to the right, the motion of the electrons perpendicularly to the in-plane magnetic field deforms the electron

orbitals in such a way that their center of mass is shifted upwards. In the classical picture the diamagnetic shift of the electron orbitals is a consequence of the Lorentz force. Half a period later, at $t = t_1 + T/2$, the electrons are driven to the left and their orbitals are shifted slightly downwards, indicated by the red areas in Fig. 28 representing the carrier density.

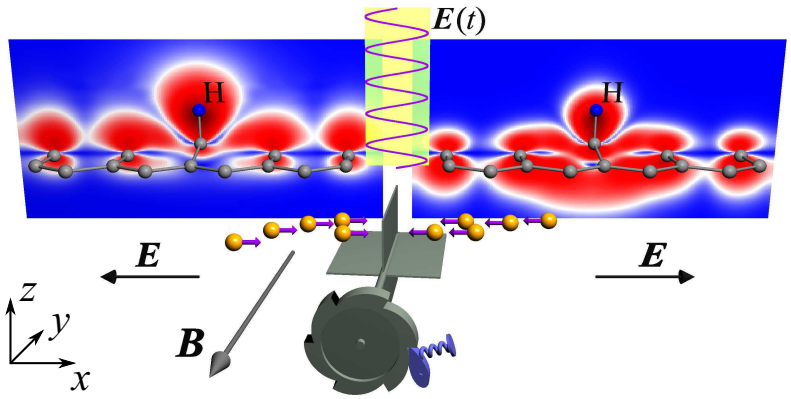

Figure 28: Dirac electrons drive a ratchet: Red spheres show carrier densities shifted up (down) for left (right) moving electrons in the presence of an in-plane magnetic field. The asymmetric scattering by hydrogen adatoms leads to a directed motion which is depicted as a ratchet and pawl mechanism.

As far as the graphene sheet has equivalent up- and down-surfaces, in other terms it is symmetric with respect to $\pm z$, the shift does not affect the motion of the carriers moving to the left or to the right and hence, within an oscillation period T of the *ac* electric field no net electric current emerges. However, in the case that $z \to -z$ symmetry is broken due to unequal up- and down-surfaces, e. g. in the presence of hydrogen adatoms, electrons with up- and down- shifted orbitals exhibit different transport behavior. In detail, the left moving electrons having their center of gravity shifted towards the adatoms (red sphere in Fig. 28) feel a stronger scattering potential from the hydrogen as the right moving electrons which are shifted downwards. By averaging over a period in time, the motions to the left and to the right do not cancel each other any more and result in one way traffic for carriers in graphene driven by an external electric field. The inevitable underlying spatial asymmetry of the system leading to the rectification of the particle flow gives rise to classify the

effect as a ratchet effect [31, 32]. Therefore, a ratchet and pawl mechanism is used in Fig. 28 in order to depict the one-way particle flow which can be rotated only in one direction from moving carriers. In the model of the magnetic quantum ratchet effect, hydrogen adatoms are chosen for reasons shown below to induce the $z \rightarrow -z$ asymmetry which can be understood as a structure inversion asymmetry. In general, the *dc* current generation is not necessarily restricted to hydrogen adatoms since every kind of substrate or adatom can cause the asymmetric electron scattering leading to the rectification.
The microscopic model of the magnetic quantum ratchet effect implies already its basic features. Since the current is caused by the orbital shift, which is a consequence of the quantum mechanical analogue of the classical Lorentz force $\boldsymbol{F}_L = q(\boldsymbol{E} + (\boldsymbol{v} \times \boldsymbol{B}))$, it depends linearly on the magnetic field $\boldsymbol{B}$. Moreover, the radiation's *ac* electric field is involved twice because it causes the oscillating motion of the electrons in the graphene sheet and also F_L is proportional to $\boldsymbol{E}$. Consequently, the effect is linear in the squared amplitude of the radiation's electric field, in other terms in the light's intensity. In the following, the semiclassical theory of the magnetic quantum ratchet effect, developed by S. A. Tarasenko and presented in [80], is introduced and the basic ideas are highlighted. Furthermore, the equations describing the current formation and its dependencies on the radiation's polarization state, magnetic field and other fundamental parameters are presented.
As discussed above, the magnetic quantum ratchet effect originates from the interplay of the *ac* electric field and the asymmetric electron scattering in the in-plane magnetic field previously considered for inversion channels in Si-MOSFETs and semiconductor quantum wells [44, 81, 82]. The general expression for the electric current density is given by

$$\boldsymbol{j} = 4e \sum_{\boldsymbol{p}} \boldsymbol{v} f(\boldsymbol{p}, t) \,. \tag{32}$$

Herein, e is the electron charge, the factor 4 accounts for the spin and valley degeneracy in graphene, $\boldsymbol{p}$ is the momentum, $\boldsymbol{v} = d\varepsilon/d\boldsymbol{p}$ is the velocity, ε is the kinetic energy, and $f(\boldsymbol{p}, t)$ is the carrier distribution function. In the case of

$E_{ph} << E_F$, the distribution function can be found by solving the Boltzmann kinetic equation [83]:

$$\frac{\partial f(\boldsymbol{p},t)}{\partial t} + e\boldsymbol{E}(t)\cdot\frac{\partial f(\boldsymbol{p},t)}{\partial \boldsymbol{p}} = \mathrm{St}[f(\boldsymbol{p},t)]\,. \tag{33}$$

Here, $\boldsymbol{E}(t) = \boldsymbol{E}\exp(-i\omega t) + \boldsymbol{E}^*\exp(i\omega t)$ is the *ac* electric field oscillating at the angular frequency ω, and $\mathrm{St}[f(\boldsymbol{p},t)]$ is the collision integral. For elastic scattering, it assumes the form

$$\mathrm{St}[f(\boldsymbol{p},t)] = \frac{2\pi}{\hbar}\sum_{\boldsymbol{p}'}\langle|V_{\boldsymbol{p}'\boldsymbol{p}}|^2\rangle[f(\boldsymbol{p}',t) - f(\boldsymbol{p},t)]\,\delta(\varepsilon-\varepsilon')\,, \tag{34}$$

where the angular brackets denote impurity ensemble averaging and $V_{\boldsymbol{p}'\boldsymbol{p}}$ is the matrix element of electron scattering between the initial and final states with the momenta $\boldsymbol{p}$ and $\boldsymbol{p}'$, respectively. The ratchet current emerges only in the case of asymmetric electron scattering in presence of the in-plane magnetic field as a consequence of structure inversion asymmetry. In the presented model, SIA is a consequence of hydrogen adatoms on top of carbon atoms which cause a $\sigma - \pi$ hybridization around the Dirac points [84]. Formally, the asymmetric scattering is described by the matrix element

$$V_{\boldsymbol{p}'\boldsymbol{p}} = V_{\pi\pi} - B_y(p_x + p_x')\frac{z_{\pi\sigma}e}{\varepsilon_{\pi\sigma}m_0 c}V_{\pi\sigma}\,, \tag{35}$$

where $z_{\pi\sigma}$ is the coordinate matrix element between the π- and σ-band states, $\varepsilon_{\pi\sigma}$ is the energy distance between the two bands, m_0 is the free electron mass, and c is the speed of light. $V_{\pi\pi}$ is the intraband- and $V_{\pi\sigma}$ the interband-matrix element of scattering at zero magnetic field. Without magnetic field the second term in Eq. (35) vanishes and $V_{\boldsymbol{p}'\boldsymbol{p}}$ stays symmetric with respect to $\pm\boldsymbol{p}$. In presence of an in-plane magnetic field however, the linear coupling between B_y and p_x leads to the asymmetry of electron scattering in momentum space and hence, to the ratchet current.

Equation (33) can be solved by expanding the distribution functions in series of powers of the electric field. The first order correction to the equilibrium distribution function oscillates at the radiation field frequency and does not contribute to any *dc* electric current. The *dc* current is mainly determined by the second order corrections in $\boldsymbol{E}$ being proportional to the squared amplitude of the radiation's electric field. For the experimental geometry where the

magnetic field is aligned along the y-direction and the radiation is shined in -z direction onto the sample, the calculations yield

$$\begin{aligned} j_x &= M_1(|E_x|^2 - |E_y|^2)B_y + M_2|\boldsymbol{E}|^2 B_y. \\ j_y &= M_1(E_x E_y^* + E_y E_x^*)B_y + M_3 i(E_x E_y^* - E_y E_x^*)B_y. \end{aligned} \tag{36}$$

For the particular case of scattering by short-range defects and degenerate statistics, relevant for the highly doped samples under study, the parameters M_1, M_2 and M_3 assume the form

$$M_1 = \frac{12\alpha^2 c\, z_{\pi\sigma}\langle V_{\pi\pi}V_{\pi\sigma}\rangle}{\pi m_0\, \varepsilon_{\pi\sigma}\langle V_{\pi\pi}^2\rangle}\frac{\tau^2 E_F}{1+(\omega\tau)^2}\,, \tag{37}$$

$$M_2 = -\frac{4\alpha^2 c\, z_{\pi\sigma}\langle V_{\pi\pi}V_{\pi\sigma}\rangle}{\pi m_0\, \varepsilon_{\pi\sigma}\langle V_{\pi\pi}^2\rangle}\frac{(1-\omega^2\tau^2/2)\tau^2 E_F}{1+(\omega\tau)^2}\,, \tag{38}$$

$$M_3 = \frac{6\alpha^2 c z_{\pi\sigma}\langle V_{\pi\pi}V_{\pi\sigma}\rangle}{\pi m_0\, \varepsilon_{\pi\sigma}\langle V_{\pi\pi}^2\rangle}\frac{\omega\tau^3 E_F}{[1+(\omega\tau)^2][1+(\omega\tau/2)^2]}\,, \tag{39}$$

where $\alpha = e^2/(\hbar c)$ is the fine-structure constant, τ is the momentum relaxation time, and E_F the Fermi energy. Equation (36) reveals a linear dependency on the magnetic field as well as a quadratic on the electric field and hence, reflects the main features of the magnetic quantum ratchet effect. This is a direct consequence of the quantum mechanical Lorentz force analogon which is linear in $\boldsymbol{B}$ and quadratic in $\boldsymbol{E}$ and drives the ratchet current. On the other hand, a complex dependence on the radiation's polarization state can be seen as well and Eqs. (37) to (39) yield a connection to sample parameters such as the momentum relaxation time and Fermi energy, as well as to the radiation frequency ω. In the following, the coincidence between theory and experiment is discussed.

4.3 Discussion

From Eq. (36) it follows that both currents, flowing perpendicular and in parallel to the magnetic field, show a complex dependence on the radiation's polarization state. Using the Stokes parameter introduced in Section 3.2.1, Eq. (36) can be rewritten as follows:

$$\begin{aligned} j_x &= M_1(|E_x|^2 - |E_y|^2)B_y + M_2|\boldsymbol{E}|^2 B_y \\ &= (M_1 S_1 + M_2 S_0)B_y. \\ j_y &= M_1(E_x E_y^* + E_y E_x^*)B_y + M_3 i(E_x E_y^* - E_y E_x^*)B_y \\ &= (M_1 S_2 + M_3 S_3)B_y. \end{aligned} \tag{40}$$

It turns out that the current flowing perpendicular to the magnetic field, j_x, is sensitive to the first (S_0) and second (S_1) Stokes parameter. This means that it consists of two parts: one being sensitive solely to the radiation's intensity and independent on the polarization state, and a second contribution which varies with the alignment of the linear polarization state. Using the angular expressions for the Stokes parameter from Eqs. (28), this part of the current oscillates with the second harmonic of the azimuth angle α. Exactly such a behavior is experimentally observed (see Fig. 23) where the overall polarization dependence was fitted after $j_x = j_1 \cos 2\alpha + j_2$. The current flowing parallel to the magnetic field, j_y, is driven by the third (S_2) and fourth (S_3) Stokes parameter. For left- and right handed circularly polarized radiation, the contribution proportional to the third Stokes parameter vanishes and the current is purely driven by the phase shift between E_x and E_y components described by $S_3 = i(E_x E_y^* - E_y E_x^*)$ or in other terms, by the radiation's helicity. This contribution has been observed experimentally (see Fig. 27) where the parallel ratchet current changes its sign by inverting the rotational direction of the radiation's electric field. From Eq. (39) it follows that the sensitivity to the rotational direction of the *ac* field reaches a maximum at $\omega\tau \sim 1$. This is in agreement with the experiments where the helicity dependent contribution to the parallel current was observed in sample Epi-4 for the highest excitation frequency, showing the highest mobility and consequently, the highest relaxation time τ. For sample Epi-6, where the contribution was also observed, no transport data is available. By contrast, for the linear photocurrent j_1 the mi-

croscopic theory predicts a different frequency behavior. Equation (37) reveals a decrease of the current with increasing frequency (see dashed line in the inset of Fig. 24). This is confirmed by the experimental data.

The microscopic model and theory of the magnetic quantum ratchet effect presented above are solely based on the excitation of carriers in response to the THz radiation. The asymmetry of electron scattering in presence of the in-plane magnetic field lead to different transport properties for counter-propagating electrons. This connection of the current to the transport properties is reflected in the temperature dependence of the perpendicular ratchet current. The polarization dependent ratchet current j_1 shows almost identical behavior in all studied samples by staying constant up to a certain temperature and decreasing by an order in magnitude up to room temperature (see Figs. 24 and 25 (a)). Equation (37) shows that j_1 depends on the momentum relaxation time τ and the Fermi energy E_F, both of them being temperature dependent. Indeed, the decrease of the current goes along with a decrease of the sample mobility (see Fig. 25 (b)) and consequently, the momentum relaxation time. From Table 1 the values of τ can be calculated to 3.32 $\times 10^{-14}$ s (4.93 $\times 10^{-14}$ s) at 4.2 K to 2.11 $\times 10^{-14}$ s (2.58 $\times 10^{-14}$ s) at room temperature in sample Epi-1 (Epi-2). However, while the momentum relaxation time decreases by roughly a factor of 2 up to room temperature, j_1 decreases by almost on order in magnitude. Hence, a full quantitative description of the temperature dependence of j_1 with Eq. (37) is not possible yet, but the effect of the transport behavior of the electrons in graphene on the ratchet current is clearly present. The current which is independent on the polarization state, j_2, shows different dependencies under variation of the temperature in samples Epi-1 and Epi-2. In contrast to j_1, which is solely a consequence of the excitation of carriers and described by the model shown above, the relaxation of carriers may lead to additional contributions to j_2 which are not described by the model of the magnetic quantum ratchet effect at all. In conventional semiconductor nanostructures, the relaxation contribution to the electric current depends on the mechanism of inelastic scattering [44, 85] and is out of scope of the present discussion.

As the next step, a quantitative analysis of the ratchet current is presented. In order to calculate the magnitude of j_1 from Eqs. (36) and (37) the matrix ele-

ment $z_{\pi\sigma} \approx 0.15$ Å and the energy $\varepsilon_{\pi\sigma} \approx 10$ eV can be taken from [86]. Fermi energy E_F and momentum relaxation time τ can be taken from Table 1. Thus, the missing parameter is the matrix element $\langle V_{\pi\pi}V_{\pi\sigma}\rangle/\langle V_{\pi\pi}^2\rangle$ for asymmetric electron scattering as a consequence of structure inversion asymmetry. In order to estimate the relevant structure asymmetry quantities, hydrogen adatoms on graphene are considered as prototypical sp^3 bonded adsorbent sitting on each carbon atom. First-principles calculations of the electronic band structures of graphene with hydrogen adatoms have been performed by J. Fabian and M. Gmitra [80]. The calculations reveal $V_{\pi\sigma} \approx 3.5$ eV as the mixing between σ and π carbon orbitals and $V_{\pi\pi} \approx 3.6$ eV as the mixing between the π orbitals in the presence of hydrogen adatoms giving the total orbital mixing to $\langle V_{\pi\pi}V_{\pi\sigma}\rangle/\langle V_{\pi\pi}^2\rangle \sim 1$. The reason for the strong mixing is the hybridization of the p_z orbitals with the orbitals of the adatoms (s for hydrogen), and subsequent mixing with the σ orbitals. With that values, the current can be calculated to $j \sim 1$ μA/cm at the magnetic field $B = 7$ T, an electric field amplitude of $2E = 10$ kV/cm and an angular frequency $\omega = 2.1 \times 10^{13}$ rad/s. The current density j_1, measured in the experiment for the same conditions, is ~ 18 μA/cm, see Fig. 25. The estimation for the current density at $T = 260$ K gives $j \sim 0.7$ μA/cm vs ~ 2.6 μA/cm measured in the experiment. Consequently, the simplified model reveals amplitudes which are within an order of magnitude compared to the experimental data.

In the microscopic theory, the presence of adatoms is considered to be the origin of the asymmetry. This might be the case in the uncovered samples under study which are sensitive to the environment. As it was mentioned in Chapter 3.4 the samples which are exposed to ambient conditions show a drift in carrier density and mobility. The chemisorbtion of adatoms is most probably the reason for this and could also be responsible for the asymmetric scattering leading to the magnetic quantum ratchet effect. The opposite sign of the ratchet current observed in the protected samples affirms the strong influence of the environment. In this group of samples, rather the protection layer instead of adatoms influence the symmetry of the system. However, it was shown in [77] that the polymer coating has no influence on the transport in graphene. It is more likely that the buffer layer can be responsible for the asymmetry in electron scattering in that systems. The buffer layer is known to interact

strongly with the graphene layer (see e. g. [87–89]) and may considerably increase SIA. To get an upper limit for this interaction the ratchet current for an asymmetric bilayer-like structure was calculated as well (see supplementary material in [80]). The estimation reveals an enhancement of the ratchet current by two orders of magnitude compared to single-layer graphene and indicates that even small interaction between two layers should enhance the magnetic quantum ratchet effect. However, large area epitaxially grown bilayer samples are not available at present and clarifying investigations remain a future task. Another hint for a substantial role of the buffer layer is the enhancement of the ratchet current in epitaxial graphene on SiC compared to the low magnitude of the signal detected in the CVD grown graphene sample. As discussed in Section 3.4, in the CVD growth process graphene is transferred onto an insulating SiO_2 layer and the interaction between both layers is known to be significantly smaller [90]. Hence, the absence of the buffer layer may lead to the observation of the weaker ratchet current in CVD grown graphene.
Finally, as shown in Fig. 26, the encapsulation of the graphene surface in a polymer leads to a consistently opposite sign of the ratchet current. While the transport parameters are almost independent of this method of post-growing treatment [77], the structure inversion asymmetry and consequently, the ratchet current is strongly affected. Equations (36)-(39) show that the change of sign can only be dedicated to the coupling of the current to the ratio between asymmetric and symmetric scattering matrix elements $\langle V_{\pi\pi} V_{\pi\sigma} \rangle / \langle V_{\pi\pi}^2 \rangle$ which is a direct measure of SIA. While the sheer existence of the ratchet current is a proof that macroscopic graphene samples exhibit a space inversion asymmetry, each specific adsorbent, substrate or cover layer may imprint its specific quantitative signature on the SIA in graphene. Consequently, the magnetic quantum ratchet effect can serve as tool to study this material property.

5 Chiral edge currents

Subsequent to the *dc* photocurrents subjected to an in-plane magnetic field, in this chapter the nonlinear transport in the vicinity of the edges of macroscopic graphene samples is investigated. According to Sections 2.3.1 and 2.3.2, the illumination of graphene at normal incidence results in zero current since neither the photon drag effect nor the photogalvanic effect are allowed under that circumstances. However, further reduction of the system's symmetry, e. g. in the vicinity of edges, may allow contributions to the photogalvanic effect even at normal incidence [91]. These contributions are studied in this chapter. At first, the experimental observation of the THz radiation driven chiral edge currents in graphene is presented. It is shown that under normal incidence of radiation a photocurrent appears which stems solely from illumination of the edges. The experiments are followed by the microscopic theory developed by M. M. Glazov and S. A. Tarasenko which is briefly summarized. It is demonstrated that the current emerges solely in a nanometer-sized channel at the sample's edges and vanishes in the interior area. The polarity of the current reveals that the carrier type changed from n to p-type within this channel what is agreement with Raman experiments. Allowing the determination of the edge scattering times, the terahertz radiation driven chiral edge currents in graphene open an experimental access to microscopic edge properties, which can usually not be separated from bulk properties.

5.1 Edge current experiments

The investigation of the high frequency transport in the vicinity of the graphene samples has been done with the optically pumped molecular THz laser from Section 3.3. The edge current experiments were performed at room temperature by applying sub-ns pulses to the unbiased sample which was mounted at a $x-y$ stage to adjust the relative beam position at the sample. The direction of incidence of radiation is the $-z$ direction (see inset in Fig. 29).

Figure 29 shows the result of an edge current experiment obtained by illuminating the epitaxial graphene sample Epi-5 with a radiation frequency of 2.02 THz and a laser peak power of 14 kW. The laser beam was adjusted

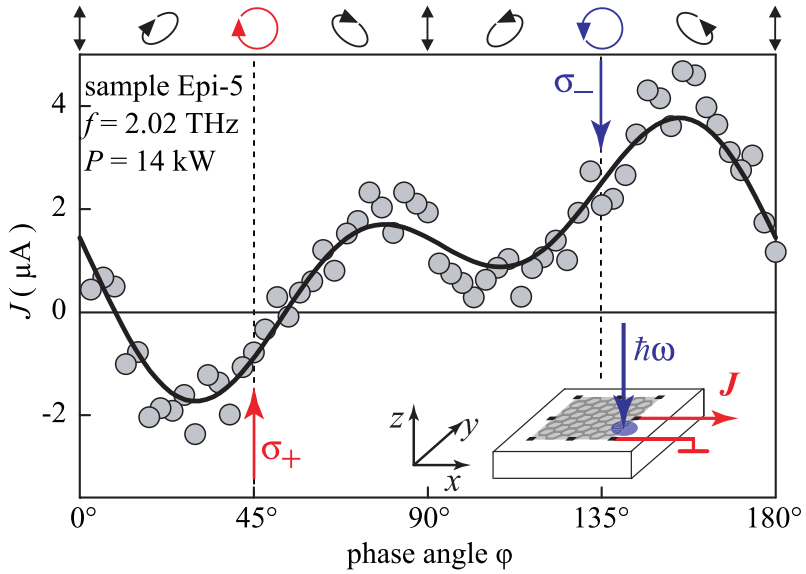

Figure 29: Photocurrent J at normal incidence in the edge's vicinity observed in sample Epi-5 as a function of the angle φ which is the rotational angle of a corresponding quarter-wave plate. The solid line is a fit after Eq. (41). The inset shows the experimental geometry and the ellipses on top illustrate the polarization states for various φ.

between two ohmic contacts by avoiding the illumination of the contact pads. The radiation's polarization state was varied with the help of a quarter wave plate according to Section 3.2.2. The photosignal was measured between the two contacts and picked up as a voltage drop over a 50 Ω load resistor. As it can be seen, the illumination of the samples edge results in a photocurrent which varies with the polarization state. Most notably, it changes its sign by switching the radiation's helicity from σ_+ to σ_- at phase angles $\varphi = 45°$ and $\varphi = 135°$, respectively. The overall dependence is more complex and well described by:

$$\begin{aligned} J(\varphi) &= J_A \sin 2\varphi + (J_B/2) \sin 4\varphi - J_C \cos^2 2\varphi + \xi \\ &= J_A P_{\text{circ}}(\varphi) + J_B S_2(\varphi) + J_C S_1(\varphi) + \xi. \end{aligned} \tag{41}$$

In the latter equation the Stokes parameter are introduced. The first term given by the coefficient J_A is proportional to the radiation helicity and reverses its sign by switching the radiation's handedness from left to right as it was observed experimentally. The second ($J \propto J_B$) and third ($J \propto J_C$) terms

change with degree and orientation of the linear polarization but vanish for circularly polarized radiation. The observed offset ξ is smaller than, or at least comparable to J_A, J_B, and J_C (see Fig. 29).

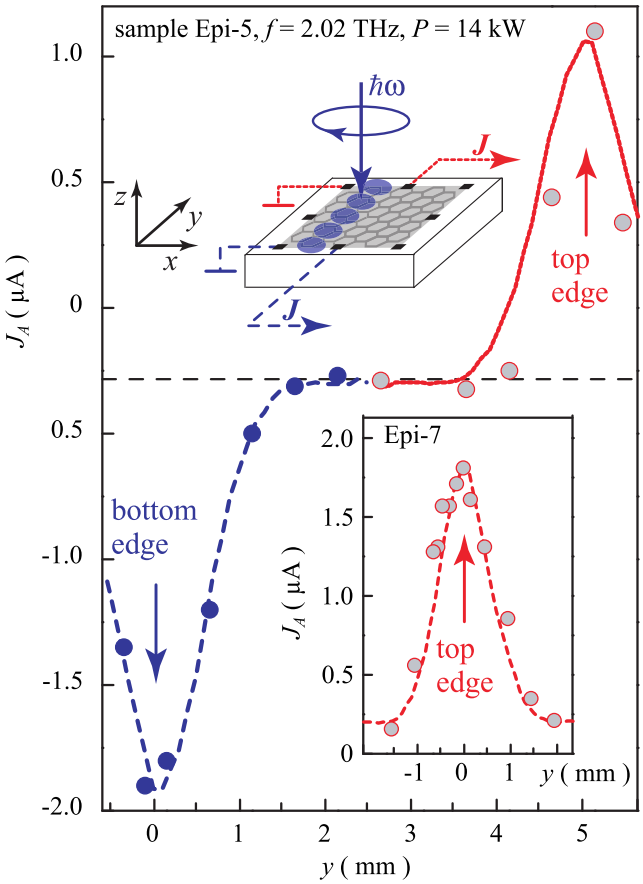

Figure 30: Photocurrent J_A in sample Epi-5 as a function of the laser spot position. The laser spot is scanned along y and the current is picked up from two contact pairs at the top (red circles) or bottom (blue full circles) sample edges aligned along x (see inset). Dashed lines represent the laser beam spatial distribution, which is measured by a pyroelectric camera, scaled to the current maximum. The inset shows a similar scan obtained in another epitaxial graphene sample.

An evidence that the photocurrent stems solely from the sample's edge is presented in Fig. 41. In order to prove this, the laser spot was scanned across the samples edge and for accuracy, a full polarization dependence was measured like the one shown above and J_A extracted by fitting Eq. (41) to the data. In

that way a detailed spatial profile of the helicity driven photocurrent J_A was recorded which is the only contribution which reverses the current direction upon switching the radiation helicity from σ_+ to σ_-. For circularly polarized light ($P_{\mathrm{circ}} = \pm 1$ and $S_1 = S_2 = 0$) and $\xi = 0$, the current is solely determined by the first term in Eq. (41). The scan across the sample's edge along the y axis reveals that J_A forms a peak which is centered around the sample's edge, and decreases close to zero if the beam is moved to the center of the sample (see Fig. 30). The comparison of the spatial distribution with the independently recorded beam profile of the laser spot (full and dashed line in Fig. 30) reveals that the signal just follows the Gaussian intensity profile. At the opposite pair of contacts, a similar spatial profile of the helicity driven current is detected by scanning the spot across the opposite edge. However, the peak is of opposite polarity and exhibits a magnitude which is larger by a factor of two. The distance between the two peaks fits perfectly to the size of the sample which is 5 mm in square. This observation clearly demonstrates that the current is caused by the illumination of the sample edges. Moreover, it shows that the helicity driven current changes its direction for opposite edges.

Similar behavior was observed in the CVD grown graphene samples as it is shown in Fig. 31 for sample CVD-2 which was excited with laser radiation at $f = 3.34$ THz and as well a peak power of 14 kW. The circular photocurrent J_A exhibits peaks at the sample's edges which are of opposite polarity. In the interior of the sample no current was observed. The spatial distribution of J_A also fits well to the beam profile. In contrast to the epitaxial samples, the magnitude of the current is lower by an order of magnitude. The overall polarization dependence (see inset in Fig. 31) is also described by Eq. (41). In this sample, a stronger polarization independent part ξ as in the epitaxial samples is present, but the circular photocurrent J_A is clearly detected at the sample's edge.

The results presented above show that the current direction at a specific edge depends on the light's helicity and is counter-propagating at opposite edges. Indeed, investigations on all accessible contact pairs yield a remarkable behavior of the circular edge photocurrent: it forms a vortex winding around the edges of the square shaped samples and shows chiral behavior in that sense

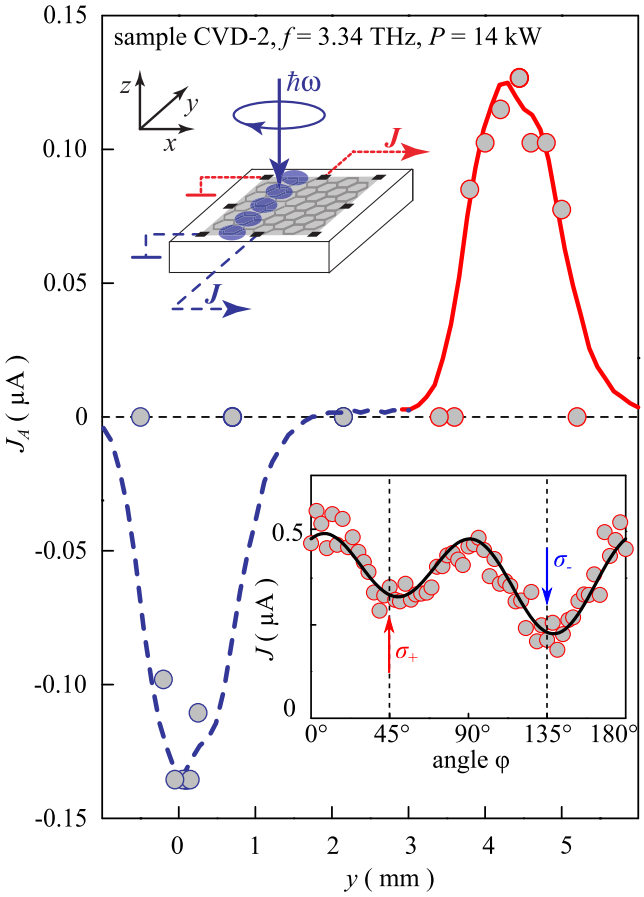

Figure 31: Spatial distribution of the circular photocurrent J_A for sample CVD-2 excited with a frequency of 3.34 THz. The current was picked up in the same way as for Fig. 30. The data are extracted from polarization dependencies as shown in the inset which refers to the currents peak position at $y = 9.4$ mm.

that it reverses its direction upon switching the radiation's helicity from right- to left-handed. The current direction for σ_+ (red arrow) and σ_- (blue arrow) circularly polarized radiation and the magnitude of J_A for various contact pairs are shown in Fig. 32 for the samples Epi-5 (a) and Epi-1 (b). This behavior was identified by centering the laser spot at the maximum signal between two contacts and recording a full polarization dependence showing that the derived amplitudes differ within the same order of magnitude for all contact pairs.

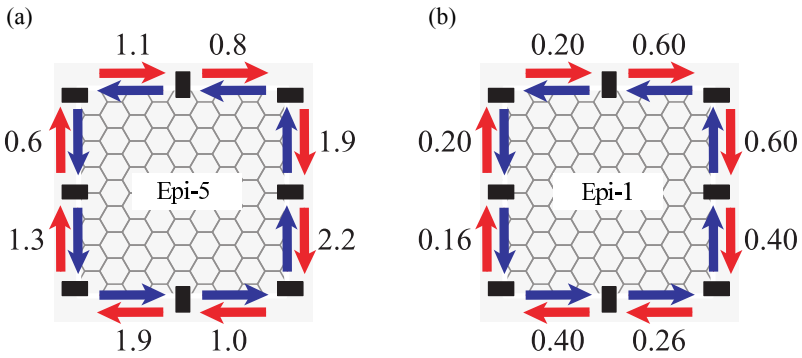

Figure 32: Amplitudes of J_A in μA measured between various contact pairs for sample Epi-5 (a) and Epi-1 (b). Red and blue arrows show the current direction for σ_+ and σ_- polarizations, respectively carried out at $f = 2$ THz and $P = 14$ kW.

5.2 Microscopic theory

All experimental results were observed under normal incidence of THz radiation. Hence, the observation that a photocurrent occurs only if the laser spot is adjusted to an edge agrees with the symmetry analysis: As shown above, at normal incidence the photon drag effect is forbidden at any symmetry, the photogalvanic effect is only allowed if the C_{6v} symmetry considered for graphene on a substrate is further reduced. Consequently, the observation of a photocurrent at *normal* incidence of radiation is a clear manifestation of the symmetry reduction of the system, in this case, due to the edges.

A microscopic process activating the edge photocurrent generation is illustrated in Fig. 33. It involves the action of the light's electric field of circularly polarized radiation on the free carriers in the vicinity of a graphene edge. Below it will be shown that solely the second order $\boldsymbol{E}$-field correction results in a directed current. The carriers follow the trajectory of the electric field leading to a time dependent motion. Assuming a clockwise rotating electric field (σ_+) acting on holes in graphene, the resulting trajectory of the carriers leads to a net motion towards the edge (in $-x$ direction), and at the same time to a motion in $+y$ direction as well. Considering diffusive scattering at the edge, a net carrier flow emerges due to the action of the electric field. This carrier flow changes its direction when a counterclockwise electric field (σ_+) acts on

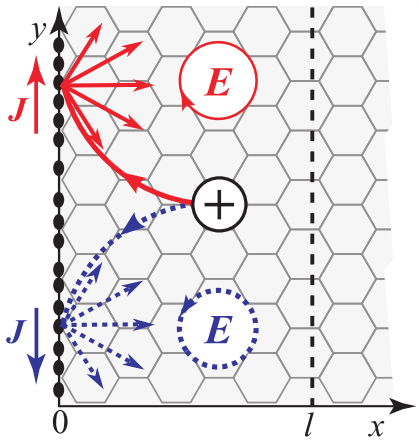

Figure 33: Action of circularly polarized radiation onto carriers in the vicinity of graphene edges accompanied by diffusive scattering at the graphene edge. The mean free path is indicated by l.

the carriers. As a result, a helicity dependent current emerges which reverses its direction upon changing the radiations degree of circular polarization (see different colors in Fig. 33). Carriers which move in $+x$-direction scatter as far as they exceed the mean free path l and do not contribute to the *dc* current. Thus, the current is restricted to a narrow channel in the vicinity of the sample's edge with a width of approximately the mean free path of the carriers. The microscopic description of the mechanism can be treated classically since the typical photon energies ($\hbar\omega_{ph} \approx 10$ meV) used in the experiments are much smaller than the characteristic energy of carriers ($E_F \sim 100$ meV). The theory of the current generation was developed by Sergey A. Tarasenko and Mikhail M. Glazov in the framework of the Boltzmann kinetic equation and will be briefly introduced in the following. In this approach, the electron (hole) distribution is described by the function $f(\boldsymbol{p}, x, t)$ which depends on the carrier momentum $\boldsymbol{p}$, coordinate x ($x \geq 0$ for a semi-infinite layer) and time t. The exact form of the distribution function can be found by solving the Boltzmann equation:

$$\frac{\partial f}{\partial t} + v_x \frac{\partial f}{\partial x} + q\boldsymbol{E}(t)\frac{\partial f}{\partial \boldsymbol{p}} = Q\{f\}, \tag{42}$$

where $\boldsymbol{E}(t) = \boldsymbol{E}_0 \mathrm{e}^{-\mathrm{i}\omega t} + \boldsymbol{E}_0^* \mathrm{e}^{+\mathrm{i}\omega t}$ is the electric field of the radiation, $\boldsymbol{v} = v\boldsymbol{p}/p$ is the electron velocity, $v \approx 10^6$ m/s is the effective speed, q is the carrier

charge ($q = +|e|$ for holes and $-|e|$ for electrons), and $Q\{f\}$ is the collision integral. Expanded in series of powers of the electric field the distribution function follows to

$$f(\boldsymbol{p}, x, t) = f_0(\varepsilon_{\boldsymbol{p}}) + [f_1(\boldsymbol{p}, x)\mathrm{e}^{-\mathrm{i}\omega t} + \text{c.c.}] + f_2(\boldsymbol{p}, x) + \dots , \tag{43}$$

yielding a static contribution $f_0(\varepsilon_{\boldsymbol{p}})$ which is the equilibrium distribution function with $\varepsilon_{\boldsymbol{p}} = vp$ being the electron energy. The first order correction $f_1 \propto |\boldsymbol{E}|$ oscillates with frequency ω and does not contribute to a *dc* current. Only the second order correction $f_2 \propto |\boldsymbol{E}|^2$ results in a directed electric current along the structure edge. Being sensitive to terms which are quadratic in the electric field reveals that the photocurrent is linear in the light's intensity. The total electric current is given by:

$$J_y = 4\ q \int_0^\infty dx \sum_{\boldsymbol{p}} f_2(\boldsymbol{p}, x) v_y \ . \tag{44}$$

Herein, the factor 4 accounts for the spin and valley degeneracy of the graphene lattice. The solution of Eq. (42) considering the scattering integral $Q\{f\}$ for diffusive scattering and fulfilling boundary conditions concerning particle- as well as energy and momentum conservation can be found in [92]. The total photocurrent follows to:

$$J_y = -\frac{q^3\tau^3 v^2}{2\pi\hbar^2[1+(\omega\tau)^2]} \left[\frac{10}{3} \frac{\omega\tau}{1+(\omega\tau)^2} \mathrm{i}[\boldsymbol{E}_0 \times \boldsymbol{E}_0^*]_z + \left(1 + \frac{7}{6}\frac{1-(\omega\tau)^2}{1+(\omega\tau)^2}\right) \times (E_{0,x}E_{0,y}^* + E_{0,y}E_{0,x}^*) \right] . \tag{45}$$

The helicity-driven current is given by the first term because $\mathrm{i}[\boldsymbol{E}_0 \times \boldsymbol{E}_0^*]_z \equiv -P_{\mathrm{circ}}$ for our geometry where the light propagates along $-z$. This term is proportional to the fourth Stokes parameter. The second term yields the current caused by linearly polarized radiation and vanishes for circular polarization. In the case of elliptically polarized light, $E_{0,x}E_{0,y}^* + E_{0,y}E_{0,x}^* \propto (1/2)\sin 4\varphi = S_2$. Both contributions to the current are proportional to the squared amplitude of the radiation's electric field. The coincidence between the experimental findings and the results obtained from theoretical considerations is discussed in the following chapter.

5.3 Discussion

Equation (45) yields two contributions to the electric current, one being sensitive to linearly polarized radiation and a second one being sensitive to the radiation's helicity. Both of them are clearly detected in the experiment and correspond to the first ($\propto J_A$) and second ($\propto J_B$) terms in the empirical Eq. (41), see Fig. 29. The focus is now shifted towards the helicity dependent contribution to the total current presented by Eq. (45). Although a linear contribution was observed as well, it is out of scope of the present discussion. Further information can be found in Ref. [30].

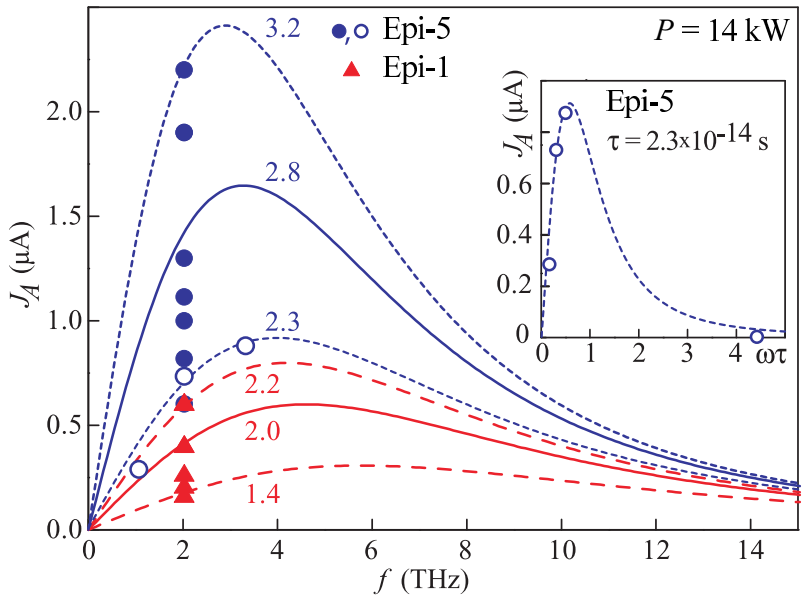

Figure 34: Photocurrent J_A measured for different edge segments. Lines are fits to Eq. (45). The fitting parameters $\tau/10^{-14}$ s for sample Epi-5 and Epi-A1 are indicated by numbers. The inset shows the measured circular photocurrent $J_A(\omega\tau)$ at one of the edge segments of sample Epi-5 (open circles) together with the fit after Eq. (45). The data point at $\omega\tau = 4.4$ is obtained applying the pulsed CO_2 laser.

As shown above (Fig. 32), the circular current forms a vortex around the square shaped samples and reverses its sign upon switching the radiation's helicity. As it was experimentally shown, the amplitudes differ for all investigated edges between different contact pairs. The amplitudes are plotted in Fig. 34 for

sample Epi-5 (blue circles) and Epi-1 (red triangles) together with Eq. (45) for circularly polarized light. The blue and red curves (full lines) are calculated using the bulk scattering times determined from Hall measurements (see Section 3.4), that are $\tau = 2.8 \times 10^{-14}$ s for sample Epi-5 and $\tau = 2.0 \times 10^{-14}$ s for sample Epi-1. It can be seen that the experimentally derived values of J_A scatter around the bulk value. For some of the contact pairs already perfect quantitative agreement is achieved with these curves. However, for other edge segments the values deviate significantly. This is a consequence of the strong non-linear dependence of J_A on the scattering time τ. Indeed, the variation of τ by only ± 15 % changes the current amplitude by almost ± 50 %. By small variations of the scattering time a coincidence between the measured amplitudes of J_A and the calculated curves can be found. Consequently, this allows the determination of the local scattering time τ for every edge segment. The best fits are shown by the dashed lines and constitute a map of scattering times along the edge. Scattering times smaller/larger than the average bulk scattering time most likely reflect primarily fluctuations of the local scattering time and hence, inhomogeneities in the distribution of scatterers.

By comparing the edge currents obtained in epitaxial graphene to that in CVD grown graphene it turns out that the amplitude in the latter one is lower by an order of magnitude. From Table 1 it follows that the carriers in the epitaxially grown graphene samples exhibit mobilities around 1000 $\mathrm{cm}^2/\mathrm{Vs}$ at room temperature. By contrast, the mobility of the CVD samples was estimated by the co-workers to approximately 500 - 750 $\mathrm{cm}^2/\mathrm{Vs}$ what is in accordance with the literature and significantly lower than the values in the epitaxially grown samples. Following Eq. (45), the lower mobility and consequently the lower momentum relaxation time result in the huge difference in the current's amplitude.

The current's frequency dependence is strongly non-monotonic as it is demonstrated by the curves in Fig. 34 which are fitted by Eq. (45). The $\omega\tau$- dependence for a single edge segment with a scattering time τ equal to $2.3 \cdot 10^{-14}$ s is presented in Fig. 34 by the open dots. The additional measurements reveal an in increase of J_A with the radiation frequency. This is in agreement with Eq. (45) which predicts zero current at zero frequency and a maximum at $\omega\tau \sim 1$. For higher frequencies the current vanishes what was also shown

experimentally. The inset of Fig. 34 shows additional results at $\omega\tau \approx 4.4$ obtained by excitation with a pulsed CO_2 laser. An edge current contribution was not observed at the highest frequency yielding An overall good agreement between Eq. (45) and the experimental findings.

Quantitatively, Eq. (45) yields that the overall polarity of the circular edge current should be negative (positive) for holes (electrons) due to the cubic dependence on q and the minus sign. However, consistently opposite signs of J_A are observed for the n-doped samples. This at a first glance surprising result agrees with results from spatially resolved Raman spectroscopy experiments on graphene flakes [93] and antidot lattices [94]. There it was carried out that the doping in the vicinity of graphene edges can change from n to p type and vice versa. This is in accordance with the observed sign of the photocurrent, which is generated in a narrow edge channel comparable to the mean free path ($\approx 10 - 20$ nm) and has opposite sign for electrons and holes, see Eq. (45). In the case of epitaxial graphene, the difference in the conductivity type can be also understood from the details of the sample fabrication. It was already pointed out above that epitaxial graphene on SiC(0001) is n-doped due to charge transfer from the interfacial buffer layer [78], while so-called quasi-free-standing graphene, lacking such buffer layer and sitting on a hydrogen terminated SiC(0001) surface, is p-doped [95]. Similar effects on the transition from n- to p-type of doping at the edges of graphene flakes on SiO_2, which were attributed to the difference in the work functions of graphene and the substrate has been reported [96]. While the origin in the change in doping is not perfectly understood yet, the chiral edge currents clearly indicate that the transport in a narrow channel close to the edges is dominated by holes. Consequently, a transmission from n- to p-type conductivity is present in the vicinity of graphene edges.

6 Reststrahl band assisted photocurrents

In the past chapters, two new photoelectric phenomena, observed at under normal incidence of radiation, have been investigated. In this chapter, it is demonstrated that the nonlinear HF photoelectric phenomena can be enhanced in graphene on a substrate with negative dielectric constant. Therefore, the observation of the photocurrents under oblique incidence of radiation in the frequency range of the reststrahl band of the substrate is presented. First, the experimental results done at the FELIX free electron laser are summarized. As a result, within the spectral region of the substrate's reststrahl band a strong amplification of the linear - and a suppression of the circular photocurrent is observed. While the microscopic origin of the current can explained in terms of the photon drag - and the photogalvanic effect, this quite unusual frequency dependence is not expected. Within the framework of a macroscopic Fresnel formalism, the resonance as well as the suppression of particular contributions to the current are explained by a strong modification of the local electric fields acting on electrons that are confined in the graphene layer. As an important result, the observed reststrahl band assisted photocurrents demonstrate that nonlinear photoelectric phenomena can be giantly enhanced by a proper combination of the spectral range and the substrate material.

6.1 Photocurrent experiments

The experiments for the investigations of photocurrents in epitaxial graphene on SiC in the spectral region of the substrate's reststrahl band have been performed at the FELIX free electron laser described in Section 3.1.2. Due to its tunability and high output power, FELIX is the perfect tool to study the photocurrents within that spectral region which can be identified from Fig. 35. Therein, the reflection spectra of graphene (red line) and SiC (dashed line) are presented, measured with a standard Fourier Transform Infrared (FTIR) spectrometer. Within the reststrahl band, the substrate is highly reflective due to the excitation of optical phonons and is restricted by the Eigenfrequencies of the transverse optical phonons ($\hbar\omega_{TO} \approx 99$ meV) and the longitudinal optical phonons ($\hbar\omega_{LO} \approx 120$ meV). The reflectivity spectra of graphene on SiC

shows only small deviations close to $\hbar\omega_{LO}$ (see dotted line in Fig. 35) and is attributed to the substrate phonon-induced surface plasmon-polariton formation in epitaxial graphene [97].

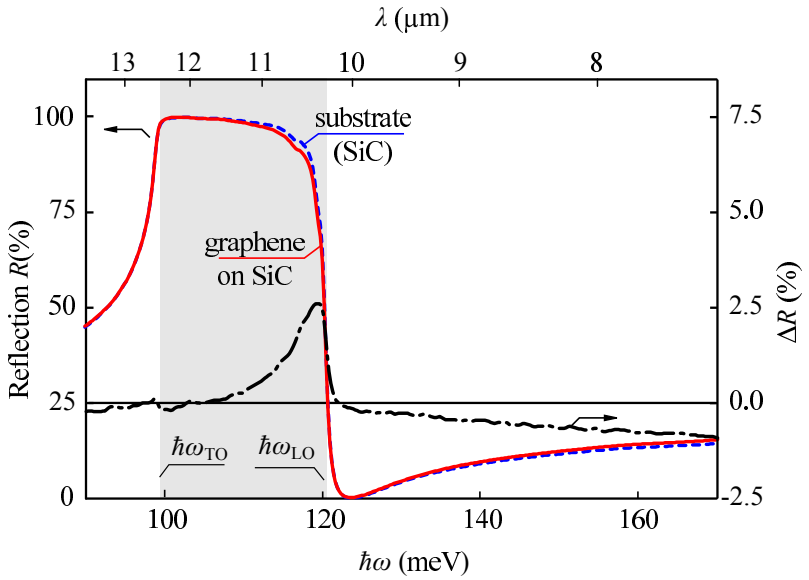

Figure 35: Reflection spectra of silicon-carbide (dashed) and graphene (red). The dash-dot line is the difference in reflectivity of both spectra and the grey area refers to the Reststrahl band of the substrate.

The geometry of the photocurrent experiments is depicted in the inset of Fig. 36. The angle of incidence θ of the radiation is defined with respect to the sample normal which is the z-axis. The angle α describes the alignment of the electric field vector with respect to the plane of incidence which is the (xz) plane. The photocurrent has been measured in two directions: i) perpendicular to the plane of incidence which is denoted as the transverse photocurrent j_y^L, and ii) parallel to the plane of incidence which is referred to as the longitudinal photocurrent j_x^L.

Under oblique incidence of radiation, a photocurrent was observed in all investigated samples which vanishes at normal incidence. The temporal shape of the current recorded with an oscilloscope repeats that of the micropulses of the laser radiation which is provided in picosecond micropulses separated by two nanoseconds very well. Figure 36 shows the spectral dependence of the transverse current j_y^L at $|\theta| = 30°$ obtained by illuminating sample Epi-1. The

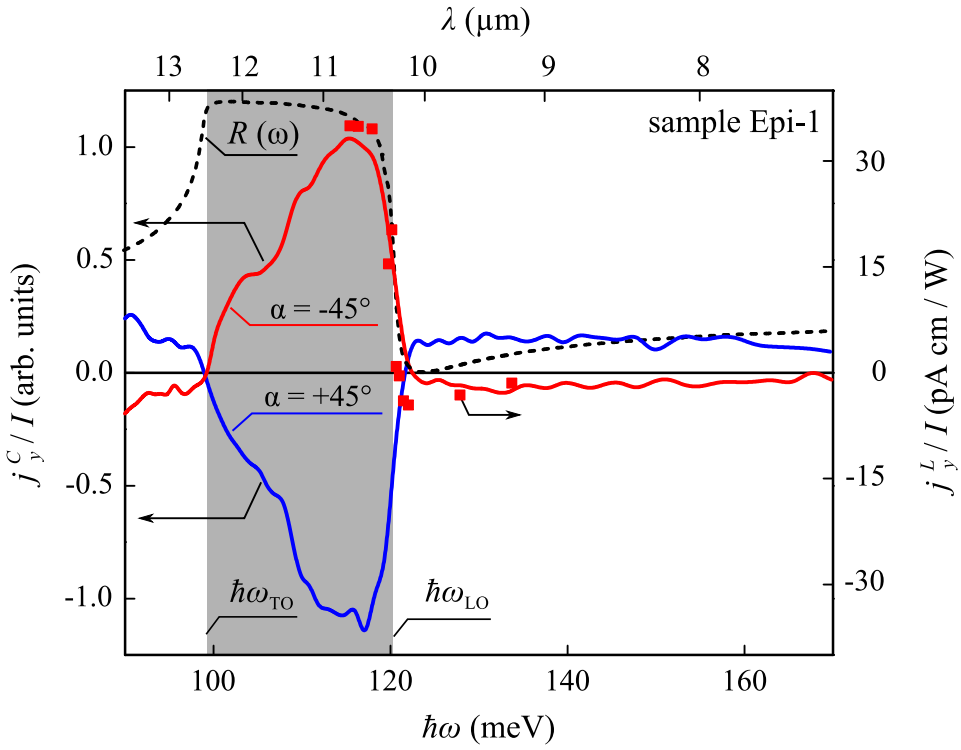

Figure 36: Spectra of the linear transverse photocurrent j_y^L under oblique incidence of radiation measured in sample Epi-1 at room temperature. j_y^L is presented by averaging after $j_y^L = (j(\theta = +30°) - j(\theta = -30°))/2$. Blue and red curves indicate different alignments of electric fields described by the angle $\alpha = \pm 45°$. The inset shows the experimental geometry and definitions of angles θ and α. The dashed line is the reflection spectrum from Fig. 35 and the grey area is the Reststrahl band of the SiC substrate indicated by the transverse ($\hbar\omega_{TO} \approx 99$ meV) - and the longitudinal optical phonon energy ($\hbar\omega_{LO} \approx 120$ meV). Dots are data points taken from [29] and belong to the right hand scale.

radiation is linearly polarized and the electric field is aligned along $\alpha = +45°$ (blue curve) and $\alpha = -45°$ (red curve). The current is averaged over two symmetric angles of incidence equal to $\pm 30°$ (for details see figure caption) to exclude any errors from possible misalignments. As a result, the transverse linear photocurrent is present in the whole investigated spectral range. Most remarkably, the current changes its sign at 10.3 and 12.4 μm corresponding

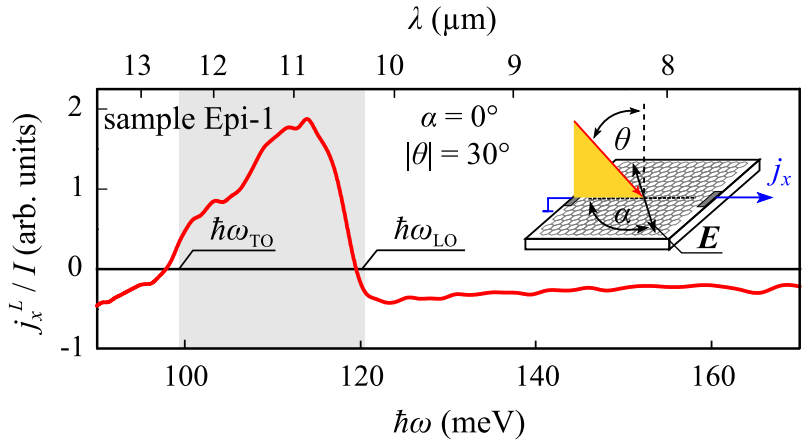

Figure 37: longitudinal photocurrent j_x^L measured in sample Epi-1 along x-direction under excitation with linearly polarized radiation. The electric field is aligned along x-direction corresponding to $\alpha = 0°$. The inset shows the experimental geometry, the grey area represents the reststrahl band of the SiC substrate.

to photon energies $\hbar\omega_{ph}$ of 99 and 120 meV. In between, the current exhibits a peak and is stronger by an order of magnitude compared to its values at shorter or longer wavelengths. The whole spectrum including the resonance changes its sign by mirroring the alignment of the electric field vector from $\alpha = +45°$ to $\alpha = -45°$ and is therefore, an odd function of α. The inversion of the angle of incidence with respect to the sample normal results in a change of sign of the current as well (not shown). The current is linear in the light's intensity and varies after $j_y^L = L \sin 2\alpha \sin\theta E_0^2$, where L is a dimensionless prefactor. A remarkable coincidence yields the comparison of the photocurrent with the reflection spectra of the sample which is plotted as the dashed line in Fig. 36 for better comparison. It turns out that the resonance of the current is connected to the spectral region where the reflectivity of the substrate $R(\omega)$ reaches unity. The resonance of the current is almost centered within the reststrahl band of the substrate and the changes of the current's sign coincide with the transverse optical phonon energy ($\hbar\omega_{TO} \approx 99$ meV) and the longitudinal optical phonon energy ($\hbar\omega_{LO} \approx 120$ meV) of the substrate. The result is in agreement with the data taken from Ref. [29], where similar behavior of the transverse photocurrent is observed in response to a Q-switch

CO_2 laser providing several discrete laser lines between approximately 9 and 11 μm. The data, indicated by the red squares in Fig. 36 show a change of sign for an almost identical photon energy and an increase of the photocurrent by an order of magnitude. However, only a narrow spectral region close to $\hbar\omega_{LO} \approx 120$ meV is investigated in that work.

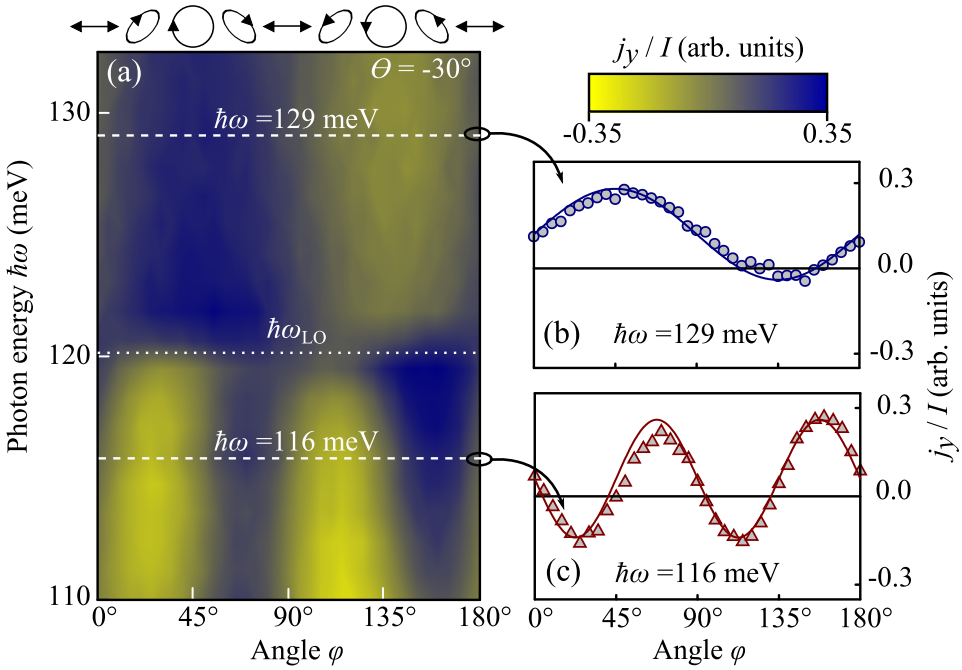

Figure 38: Transverse photocurrent in response to elliptically polarized radiation. (a) shows frequency scans for different angles of φ with resulting polarization states on top. The right panel shows polarization dependencies for $\hbar\omega_{ph}$ at 116 (b) and 129 meV (c), respectively. Full lines are fit functions after the Stokes parameter. All data are obtained at $\theta = -30°$.

In addition to the transverse current, the illumination with linearly polarized radiation results also in a photocurrent in longitudinal direction. Figure 37 shows j_x^L excited with an electric field aligned along the plane of incidence ($\alpha = 0°$), averaged over $\theta = \pm 30°$. A similar resonance is present compared to that detected in the transverse direction, again accompanied by a double change of sign. Overall, the current varies with $j_x^L = L \cos 2\alpha \sin\theta E_0^2$ and vanishes for $\alpha = \pm 45°$ (not shown).

The transverse photocurrent shows also sensitivity to elliptically polarized radiation. Dependencies of the current obtained by the rotation of a Fresnel rhomb according to Section 3.2.4 and the resulting polarization states for various rotational angles φ can be found in Fig. 38. For φ equal to 45° and 135° circularly polarized radiation is produced, described by the circular degree of polarization which oscillates with $\propto \sin 2\varphi$. In contrast, the degree of linear polarization oscillates with $\propto \sin 4\varphi$. Polarization dependencies for two differ-

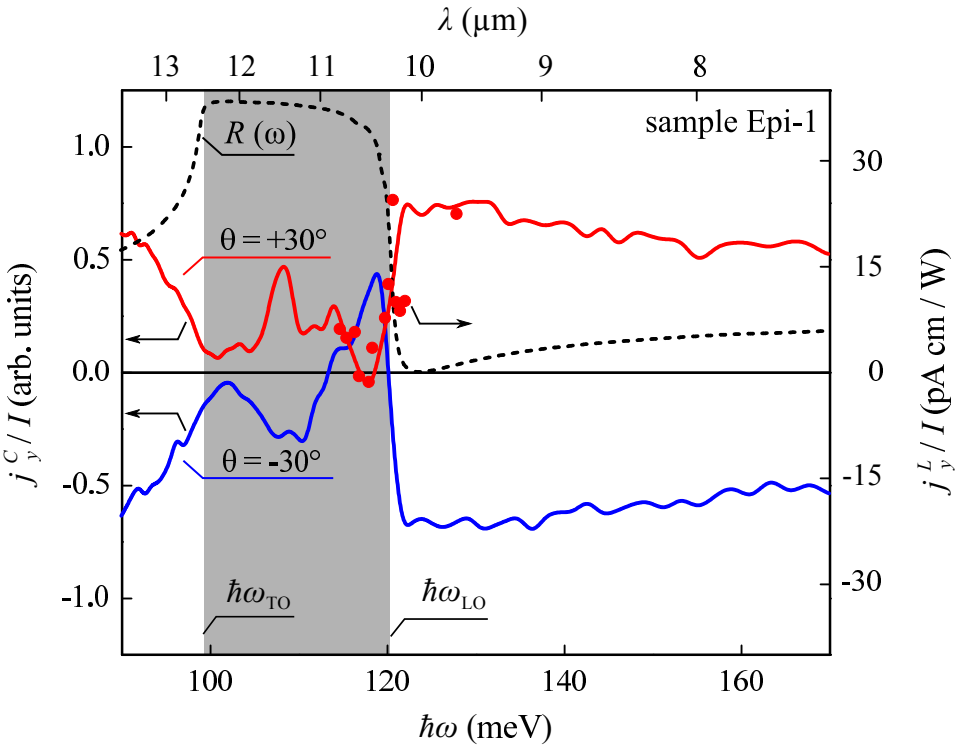

Figure 39: Spectra of the circular transverse photocurrent j_y^C under oblique incidence obtained in sample Epi-1 at room temperature. The circular photocurrent was measured for right (σ^+) and left (σ^-) handed circularly polarized radiation and averaged after $j_y^C = (j(\sigma^+) - j(\sigma^-))/2$. Blue and red curves indicate different angles of incidence. The grey area is the reststrahl band of the SiC substrate obtained from reflectivity measurements (dashed line) and indicated by the phonon Eigenfrequencies of the transverse optical phonons ($\hbar\omega_{TO} \approx 99$ meV) and the longitudinal phonons ($\hbar\omega_{LO} \approx 120$ meV). Dots are data points taken from [29] for intensity calibration.

ent photon energies are shown on the right hand side of Fig. 38. The transverse photocurrent can be fitted by a superposition of linear and circular contributions after $j_y = j_y^L + j_y^C = [(L/2)\sin 4\varphi + C\sin 2\varphi]\sin\theta\, E_0^2$. At $\hbar\omega_{ph} = 116$ meV (Fig. 38 (c)) the linear contribution proportional to $\propto \sin 4\varphi$ is dominant. In contrast, for $\hbar\omega_{ph} = 129$ meV (Fig. 38 (b)) the current oscillates rather with $\propto \sin 2\varphi$ and is sensitive to circularly polarized radiation. A transition from a dominating linear to circular current can be seen from the 2D color plot on the left hand side of Fig. 38. Blue (yellow) colors indicated positive (negative) amplitudes of the transverse current. The color map indicates that the current oscillates with $\propto \sin 4\varphi$ for $\hbar\omega_{ph} < \hbar\omega_{LO}$ and with $\propto \sin 2\varphi$ for $\hbar\omega_{ph} > \hbar\omega_{LO}$. A sharp transition from a linear to a circular photocurrent can be observed at $\hbar\omega_{ph} = \hbar\omega_{LO} = 120$ meV. The data were taken at an angle of incidence θ equal to $-30°$.

The spectral dependence of the circular transverse photocurrent j_y^C obtained by applying right (σ^+) and left (σ^-) handed circularly polarized radiation to the sample is shown in Fig. 39. The current results from averaging over ($\sigma^\pm$) and is plotted for $\theta = \pm 30°$. It turns out that in contrast to the linear photocurrent which is strongly enhanced between $\hbar\omega_{TO}$ and $\hbar\omega_{LO}$, the circular photocurrent is rather suppressed within the reststrahl band of the substrate. For larger photon energies the circular contribution is higher in magnitude than the linear current. The data are again in agreement with that taken from [29]. In longitudinal direction, a circular photocurrent was not detected.

6.2 Phenomenological analysis

Following Sections 2.3.1 and 2.3.2, the generation of the photocurrent under oblique incidence of radiation can be devoted to both the photon drag effect and the photogalvanic effect. Indeed, it was shown in Ref. [29] under similar experimental conditions, that the photocurrent emerges as a result of the superposition of both phenomena. Without going into microscopic details, the phenomenological equations reveal a couple of features which coincide with

the experimental findings. In the experimental geometry considered above they can be rewritten as follows:

$$j_x^{PDE} = \widetilde{T}' q_x(|E_x|^2 + |E_y|^2) + T q_x(|E_x|^2 - |E_y|^2), \tag{46}$$

$$j_y^{PDE} = T q_x(E_x E_y^* + E_x^* E_y) + T' q_x \mathrm{i}(E_y E_x^* - E_x E_y^*), \tag{47}$$

for the PDE and

$$j_x^{PGE} = \chi\,(E_z E_x^* + E_x {E_z}^*), \tag{48}$$

$$j_y^{PGE} = \chi\,(E_z E_y^* + E_y {E_z}^*) + \gamma\,\mathrm{i}(E_z E_y^* - E_y {E_z}^*), \tag{49}$$

for the PGE. Herein, $\boldsymbol{E}$ is the electric field acting on electrons, T, $\widetilde{T}'$ and χ are coefficients describing, respectively, the PDE and PGE currents proportional to the linear polarization given by symmetrical combinations of electric field components. The two remaining coefficients correspond to the circular PDE (T') and PGE (γ) currents. These contributions reverse the direction upon switching the photon helicity $P_\mathrm{c} = i(\boldsymbol{E} \times \boldsymbol{E}^*) \cdot \boldsymbol{q}/q$. Thus, it follows from Eqs. (46) and (48) that j_x is sensitive to linearly polarized radiation only. Indeed, in the longitudinal direction, no circular photocurrent has been observed. By contrast, the transverse current j_y has both linear (see Fig. 36) and circular contributions (see Fig. 39). Furthermore, both longitudinal and transverse current reverse their direction upon inversion of the angle of incidence of the radiation with respect to the sample normal (see Fig. 39). This can be dedicated to the inversion of the in-plane component of the photon wavevector q_x for the PDE, and to the reversion of the out-of-plane component of the electric field E_z in the case of the PGE. All observed agreements with the phenomenological equations remain unchanged over the entire investigated spectral region.

While Eqs. (46) to (49) reflect most of the experimentally observed features, they do not explain the observed resonance (suppression) of the linear (circular) photocurrent. In the frequency range $E_{ph} \leq E_F$ and room temperature, the microscopic mechanism is expected to be the same over the entire studied spectral region. Consequently, both the PDE and the PGE arise in response to Drude-like intraband absorption processes where a smooth dependence on the radiation frequency is expected. This is observed outside the substrate's reststrahl band where both linear and circular photocurrents are almost independent on the photon energy. However, in this absorption regime no resonant

process is expected being responsible for the resonance/suppression inside the band. Also all prefactors of the phenomenological equations have smooth frequency dependencies [28, 29].
A possible origin of the unusual frequency dependence of the current is most likely the modification of the local electric fields acting on the carriers in graphene. Indeed, one can expect drastic modifications of the in-plane and out-of-plane radiation electric field components for frequencies within the reststrahl band of the substrate which is characterized by a negative dielectric constant of the material. Under oblique incidence of radiation, an electromagnetic wave is reflected at the substrate leading to an interference of both incoming and reflected wave. Thus, the electric field acting on the carriers in the graphene layer and driving the electric current would rather be that resulting from the interference instead of that of the incoming wave. In the following section, the analysis of the modified electric fields within a macroscopic Fresnel formalism is presented.

6.3 Fresnel analysis of the local electric fields

The reststrahl band of a polar crystal, such as SiC, is characterized by a negative dielectric constant ε, which is given in its general from by [35]

$$\varepsilon(\omega) = \varepsilon_\infty + \frac{\varepsilon_0 - \varepsilon_\infty}{1 - (\omega/\omega_{TO})^2 - \mathrm{i}\omega\Gamma/\omega_{TO}^2}. \tag{50}$$

Herein, ω_{TO} and Γ are the frequency and the damping of the transverse optical phonon, ε_0 and ε_∞ are the low- and high-frequency dielectric constants, respectively. The complex dielectric function and, consequently, the complex refractive index $\sqrt{\varepsilon} = n + \mathrm{i}\varkappa$, determine the frequency dependence of the electric field components. Here n is the real part of the refractive index and $\varkappa$ its imaginary part, often referred to as the extinction coefficient. Within the reststrahl band, ε is negative and the material highly reflective due to a non-zero imaginary part. Consequently, an incoming electromagnetic wave gets almost perfectly reflected.
In Sections 2.3.1 and 2.3.2, the photon drag - and the photogalvanic effect are considered in response to single electromagnetic waves acting on the carriers

in graphene. This is reasonable for graphene synthesized on a substrate which is transparent in the investigated frequency region. However, in the present case when the substrate is highly reflective within the reststrahl band, the local electric field components responsible for the current generation may be considered as a superposition of that of the incoming and the reflected wave rather than that of a single wave. A scheme of the electric fields acting on the carriers in graphene is depicted in Fig. 40 (a).

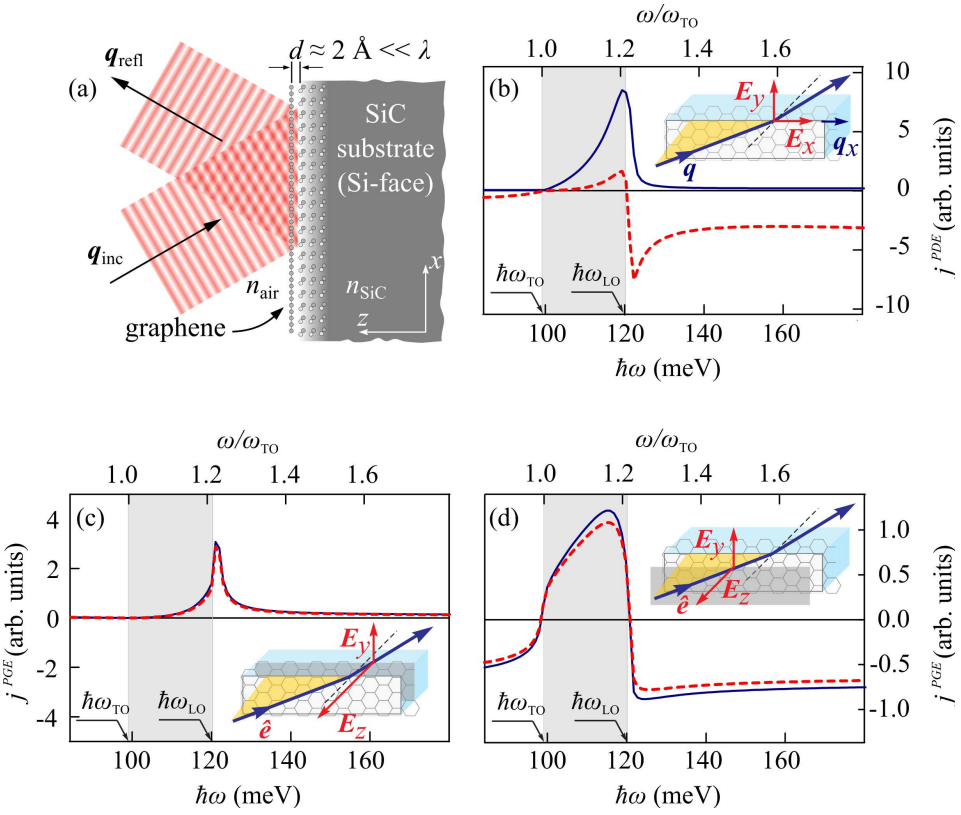

Figure 40: (a) Scheme of interfering incoming (q_{inc}) and reflected waves (q_{refl}) acting on graphene on SiC. (b)-(d) Calculated spectral dependence of the linear (solid) and circular (dashed) photocurrents. (b) Photon drag effect. (c) and (d) Photogalvanic effect caused by the electric field in the SiC side, $\boldsymbol{E}^{in}$, and in the air side of the air/SiC interface, $\boldsymbol{E}^{out}$, respectively. The insets show components of the electric field and photon wave vector considered in the corresponding calculations.

The spectral dependence of the photocurrent in response to the superimposed electric fields can be determined from the modified in-plane and out-of-plane electric field components, $\boldsymbol{E}^{in}$ and $\boldsymbol{E}^{out}$, of the interfering waves. These were calculated by L. E. Golub in the framework of a macroscopic Fresnel formalism [98] under the following assumptions: i) the graphene layer does not affect the radiation's electric field and ii) all prefactors in Eqs. (46) to (49) describing, respectively, the PDE and PGE are smooth functions of the radiation frequency. To obtain the frequency dependence of the required electric field the corresponding Fresnel transmission coefficients for oblique incident radiation were calculated, given by

$$t_s = \frac{2\cos\theta_0}{\sqrt{\varepsilon - \sin^2\theta_0} + \cos\theta_0}, \tag{51}$$

$$t_p = \frac{2\sqrt{\varepsilon}\cos\theta_0}{\sqrt{\varepsilon - \sin^2\theta_0} + \varepsilon\cos\theta_0}. \tag{52}$$

for s (perpendicularly) - and p (parallel) - polarized components of the electric fields. At an oblique incidence of radiation on the dielectric media with $\varepsilon(\omega)$ the wavevector component in the surface plane is $q_x = (\omega/c)\sin\theta_0$ is continuous while the normal wavevector component inside the medium $q_z^{in} = (\omega/c)(n+\mathrm{i}\varkappa)$ where

$$n = \frac{\sqrt{\sqrt{(\varepsilon' - \sin^2\theta_0)^2 + \varepsilon''^2} + \varepsilon' - \sin^2\theta_0}}{2}, \tag{53}$$

$$\varkappa = \frac{\sqrt{\sqrt{(\varepsilon' - \sin^2\theta_0)^2 + \varepsilon''^2} - (\varepsilon' - \sin^2\theta_0)}}{2}. \tag{54}$$

Here ε' and ε'' are the real and imaginary parts of the dielectric function, respectively.

As a result, the in-plane electric field components which are continuous at the air/SiC interface follow to

$$E_x = t_p E_{0p}(n + \mathrm{i}\varkappa)\Xi, \qquad E_y = t_s E_{0s}, \tag{55}$$

where E_{0s}, E_{0p} are the corresponding parts of the incident wave amplitude and $\Xi = 1/\sqrt{n^2 + \varkappa^2 + \sin^2\theta_0}$. In contrast, the normal-to-plane component E_z is

discontinuous at the air/SiC interface [70]. Therefore, its values inside E_z^{in} and outside the substrate E_z^{out} were calculated as the limiting cases:

$$E_z^{in} = -t_p E_{0p} \sin\theta_0 \Xi, \quad E_z^{out} = \varepsilon E_z^{in}. \tag{56}$$

With that knowledge, the photocurrent contributions can be calculated. For the photon drag effect, the in-plane wave-vector - and electric field components yield

$$\begin{aligned} j_y^L =& \frac{\omega}{c} \sin\theta_0 P_\mathrm{l} |E_0|^2 \\ & \times \left[(nT + \varkappa T') \operatorname{Re}(t_p^* t_s) + (\varkappa T - nT') \operatorname{Im}(t_p^* t_s) \right] \Xi, \end{aligned} \tag{57}$$

$$\begin{aligned} j_y^C =& \frac{\omega}{c} \sin\theta_0 P_\mathrm{c} |E_0|^2 \\ & \times \left[(\varkappa T - nT') \operatorname{Re}(t_p^* t_s) - (nT + \varkappa T') \operatorname{Im}(t_p^* t_s) \right] \Xi. \end{aligned} \tag{58}$$

for the linear and circular photon drag effect. $P_l = (E_{0p}E_{0s}^* + E_{0s}E_{0p}^*)/|E_0|^2$, and $P_c = \mathrm{i}(E_{0p}E_{0s}^* - E_{0s}E_{0p}^*)/|E_0|^2$ describe the linear and circular degree of polarization.

For the photogalvanic effect, depending on the out-of plane electric field component E_z, two solutions were derived. First, at the air side of the air/SiC interface, E_z^{out}:

$$j_y^L = -\sin\theta_0 P_\mathrm{l} |E_0|^2 \left[\chi \operatorname{Re}(t_p^* t_s) + \gamma \operatorname{Im}(t_p^* t_s) \right] \Xi, \tag{59}$$

$$j_y^C = -\sin\theta_0 P_\mathrm{c} |E_0|^2 \left[\gamma \operatorname{Re}(t_p^* t_s) + \chi \operatorname{Im}(t_p^* t_s) \right] \Xi, \tag{60}$$

and second, for the field in the SiC side of the interface, E_z^{in}:

$$j_y^L = -\sin\theta_0 P_\mathrm{l} |E_0|^2 \left[\chi \operatorname{Re}(t_p^* \varepsilon^* t_s) + \gamma \operatorname{Im}(t_p^* \varepsilon^* t_s) \right] \Xi, \tag{61}$$

$$j_y^C = -\sin\theta_0 P_\mathrm{c} |E_0|^2 \left[\gamma \operatorname{Re}(t_p^* \varepsilon^* t_s) + \chi \operatorname{Im}(t_p^* \varepsilon^* t_s) \right] \Xi. \tag{62}$$

The spectral dependencies of all possible contributions are plotted in Fig. 40 (b) - (d) in response to linearly (blue) and circularly polarized radiation (red). For the calculations, the following parameters were used: $\theta_0 = 30°$, $\gamma/\chi = 0.9$, $T'/T = 18$, the damping constant $\Gamma = 0.01\,\omega_{TO}$ obtained from the reflection data, and SiC high- and low-frequency dielectric constants $\varepsilon_\infty = 6.52$, $\varepsilon_0 = 9.66$, respectively (see Ref. [99]). The agreement of the calculations and the experimental observations is discussed in the following section.

6.4 Discussion

The calculations presented above clearly reveal strong modifications of the photocurrents within the reststrahl band of the substrate. By analyzing the contributions separately it turns out that the photon drag current reflects two of the main features of the experimental observations, that is the suppression of the circular and the resonance of the linear photocurrent (see Fig. 40 (b)). The suppression of the circular photocurrent follows from Eq. (58). In the case of a non-zero imaginary part of $t_p^* t_s$, present for a negative ε, real- and imaginary parts have different signs for circularly polarized radiation and cancel each other. This can be understood as the modification of the circular polarization state into an elliptically polarized state due to the reflection at the substrate and the interference. As a results, the circular photocurrent is reduced within the reststrahl band. By contrast, the linear photocurrent described by Eq. (57) is enhanced because real- and imaginary part of $t_p^* t_s$ add up. However, while the enhancement and suppression are well explained in terms of the photon drag effect, they do not describe the double change of sign of the linear contribution. This can be explained taking into account the PGE current. Considering first the contribution derived for the electric field in air (Fig. 40 (d)), the linear PGE shows two sign inversions close to $\hbar\omega_{LO}$ and $\hbar\omega_{TO}$ and a broad resonance covering the entire reststrahl band. However, the circular contribution behaves almost identical what is not observed experimentally. For the electric field E_z^{in} within the substrate, Fig. 40 (c) reveals that the current appears only in the vicinity of $\hbar\omega_{LO}$ where both contributions show a sharp resonance peak. Such a behavior is not observed in the experiments and hence, this contribution is neglected. In order to achieve an overall agreement between theory and experiment the current is calculated as a superposition of the photon drag - and the photogalvanic effect considering solely E_z^{out} for the latter effect.

The result of the calculations performed with the parameters introduced above is presented in Fig. 41 (b) together with the experimental data (a). Blue (red) curves represent the linear (circular) photocurrent. Both calculated curves where normalized onto the maximum value of the linear photocurrent in order to compare relative amplitudes. By that, a good agreement between theory

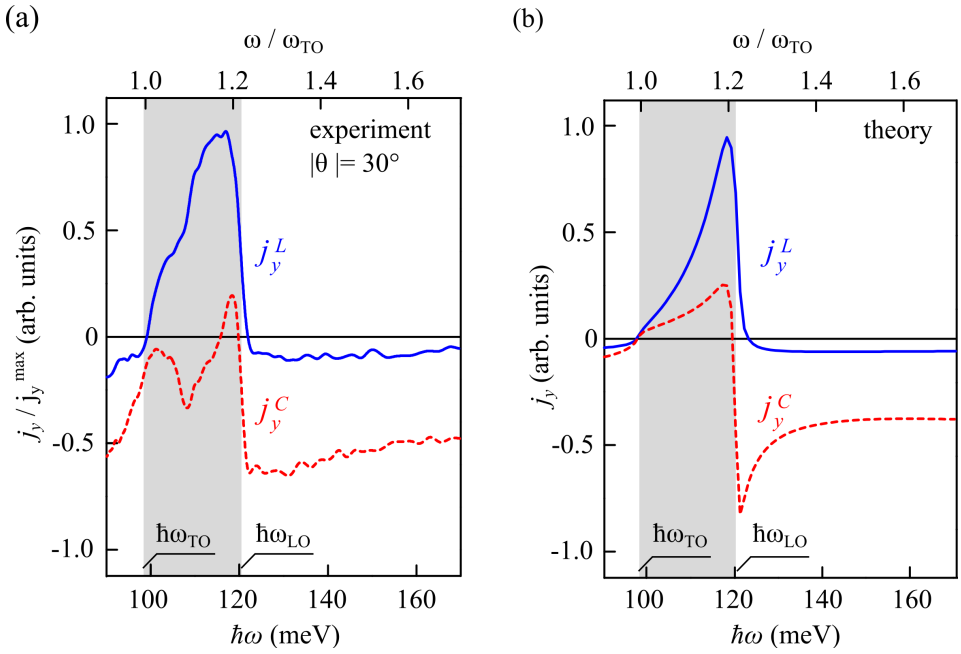

Figure 41: Spectral behavior of the linear (solid lines) and circular (dashed lines) photocurrents. (a) Experimental results calculated after $j_y = (j_y(\theta = -30°) - j_y(\theta = +30°))/2$. (b) Calculated photocurrent for electric field components E_x, E_y, E_z^{out} and the parameters given in the maintext.

(right panel) and experiment (left panel) is achieved. The main features, such as the sign changes of both photocurrents, the suppression of the circular and the enhancement of the linear photocurrent, are reproduced. Outside the reststrahl band, both currents depend only weakly on the radiation frequency. Moreover, the ratio between circular and linear photocurrents fits well to the experimental data. Within the reststrahl band, the linear dominates the circular current and outside it is vice versa. Comparing Fig. 41 to Fig. 40 (b) and (d) it turns out that within the resonance, the linear current is strongly dominated by the PDE whereas outside the resonance the main contribution comes from the PGE. For the circular photocurrent, the PDE is dominating in the whole studied spectral range.

The described agreements are achieved within a macroscopic formalism. Thus, it is tempting to assume that the electric field in the vicinity of a surface is de-

termined by the Fresnel formulas. In fact, the calculations have been performed assuming interfaces of fictitious homogeneous dielectric media described by dielectric functions. In the field of optics this assumption is usually valid since the wavelengths of light as well as penetration depths of evanescent waves exceed interatomic distances by several orders of magnitude. On an atomic length scale, however, the physics could be quite different at surfaces, because the local polarizability of the single atomic layer may deviate from the bulk values. These simplifications, the fact that influences of graphene on the optical fields were disregarded and possible charge transfer between graphene and SiC [78] induced by the E_z-electric field may be responsible for remaining discrepancies. It is also worth mentioning that the features of the current that would result from the E_z^{in}- component are not observed at all and were disregarded. This is rather unexpected since epitaxial graphene is deposited in the vicinity of atomic distances around 0.2 nm on top of SiC. Under that assumption, the primarily acting electric field onto the charge carriers trapped in the perfectly two-dimensional crystal graphene is that at the air-side of the air/SiC interface, E_z^{out}.

Finally, the complex spectral behavior of the dielectric constant ε within the reststrahl band, see Eq. (50), results in the enhancement of particular electric field components. As an example, the E_xE_y product changes by a factor of 8.4 upon variation of radiation frequency from ω lying outside the reststrahl band ($\omega = 0.5\ \omega_{\mathrm{TO}}$) to that within the reststrahl band ($\omega = 1.2\ \omega_{\mathrm{TO}}$) and leads to the resonance/enhancement of the linear photocurrent. This demonstrates that nonlinear HF photoelectric phenomena in 2D crystals can be giantly enhanced when they are deposited on a substrate with a negative ε.

7 Conclusion

To summarize this work, several nonlinear high frequency transport phenomena were observed and investigated in graphene under THz laser excitation. The results demonstrate that driven out of equilibrium by an *ac* electric field, carriers in graphene exhibit a directed motion in response to the second order electric field correction. The observation of the phenomena in graphene show that the nonlinear electric field corrections yield significant contributions to the current density even in the purest two-dimensional materials. The studies of the nonlinear HF photoelectric phenomena give access to fundamental properties of graphene and may serve as a model system for investigations of other 2D crystals.

In the first part of this work, the magnetic quantum ratchet effect was experimentally observed and theoretically explained. It has been demonstrated, that the carrier motion in response to an electric field in presence of an in-plane magnetic field results in an orbital shift of the electron wavefunction, though graphene is almost perfectly two-dimensional. In the case of a spatially asymmetric system, for instance if graphene is synthesized on a substrate or due to the chemisorbtion of adatoms, this shift leads to different mobilities for counterpropagating carriers and finally, to the rectification of an *ac* electric field into a *dc* current. The observation of the ratchet current is a strong evidence that structure inversion asymmetry is present even in graphene. In parallel, a microscopic theory was developed which is assisted by first-principle calculations of the band-structure of graphene in the presence of hydrogen atoms being the source of the asymmetry. The simplified model describes all experimental findings and allows the recalculation of the ratchet current within the same order of magnitude compared to the experimental values. As the magnetic quantum ratchet effect is sensitive to the sign and strength of the SIA it can serve as tool to explore its origin which may lead to better understanding in graphene spintronics [100–103] and ferromagnetism [104,105]. A future task is to study various graphene systems, such as e. g. bilayer and intercalated epitaxial graphene as well as monolayer graphene grown from the carbon face of SiC, for which strong modifications of the ratchet current can be expected. Besides the magnetic field induced photocurrents, photoelectric phenomena

have also been studied in the vicinity of edges. In the second part of the thesis it was demonstrated that the illumination of the edges of macroscopic samples results in chiral photocurrents in response to the second order electric field correction. The effect is directly coupled to electron scattering at the graphene edge and vanishes in bulk graphene. It was shown that the current emerges solely in a narrow 1D channel with a width of roughly the mean free path of the carriers. The semiclassical theory based on the Boltzman kinetic equation reveals a transmission from n-type doping in the interior region of the sample to p-type doping within the edge channel. The agreement between theory and experiments allows the determination of the edge scattering times which deviate from the "bulk" scattering time for each specific edge segment. Consequently, the chiral edge currents give an experimental access to the transport properties in the vicinity of graphene edges which are hard to study in common transport experiments. While the effect should exist in any 2D material, the specific properties of graphene, i. e. the high velocity of massless Dirac fermions, facilitate the experimental observation. An interesting aim for future research is to access the quantum regime where novel phenomena may occur [106, 107].

Finally, the enhancement of the nonlinear high frequency transport phenomena in graphene deposited on a substrate with a negative dielectric function was demonstrated. It has been shown that, within the spectral region of the reststrahl band of the substrate, the amplification of particular electric field components leads to a resonance of THz radiation induced photocurrents. The modification of the local electric fields acting on the carriers in graphene was explained within a macroscopic Fresnel formalism. Consequently, the investigation of the photocurrents in graphene in the spectral region of the reststrahl band of the substrate give access to the local electric fields acting at atomic distances. Moreover, the findings demonstrate that optical and optoelectronic phenomena can be giantly enhanced in strictly 2D systems deposited on a substrate with a negative ε. While in the present case the effect is restricted to a narrow spectral region, artificial structures with negative ε, for instance metamaterials [108, 109], may serve to study the broadband enhancement of the effects making use of the higher orders of the electric field in 2D systems.

8 Appendix

8.1 Helicity sensitive detection by field effect transistors

Terahertz science and technology hold a great promise for progress in diverse scientific areas and have a wide application potential in environmental monitoring, security, biomedical imaging and material characterization, see e.g. [19]. Most of the these applications require sensitive, but robust room temperature THz detectors with fast response time. Recently, field-effect-transistors (FETs) have been demonstrated as promising detectors of THz radiation (for review see e. g. [110]). The operation principle is based on the nonlinear properties of the two-dimensional (2D) plasma in the transistor channel. Most promising are the facts the FETs may serve for broadband room temperature detection from tens of gigahertz up to terahertz with very high sensitivity (5 kV/W) and low noise equivalent power below 10 pW/$\sqrt{\text{Hz}}$ [111]. Moreover, they can also be integrated on chip electronics and combined into matrices using standard III-V or silicon complementary metal-oxide-semiconductor (CMOS) technology [112].

While plasma based compact THz receivers are in focus of current research, the dependence of the voltage response on the radiation's polarization state is not yet exhaustively studied. The problem of radiation coupling and angular response to the linearly polarized radiation has been addressed recently by several groups [113]. However, no studies on the detector's response to circularly polarized radiation have been carried out so far. Exactly this is the goal of this chapter. It will be shown that for a certain design of the FETs the photoresponse has a substantial contribution which is proportional to the degree of circular polarization of the incident radiation. The generation of the photoresponse as well as its polarization dependence will be described in the framework of an extension of the Dyakonov-Shur (DS) model of rectification by FETs [114]. The observed helicity dependent photoresponse in FETs provides the basis for a sensitive all-electric characterization of THz radiation's polarization state and, therefore, can be used for the development of new methods of THz ellipsometry applying FET detectors.

8.1.1 Dyakonov-Shur model of broadband THz detection

In this section, the plasma nonlinearities based model of THz detection, proposed by Dyakonov and Shur in 1993 [115] is briefly reviewed. The basic idea is that a directed current in a two-dimensional electron fluid confined in the channel of a FET should be unstable because of the generation of plasma waves. The channel acts as a resonator for the plasma waves and under certain conditions they can be amplified due to the reflection at the device boundaries. The amplified charge carrier density oscillations were predicted to lead to the generation of far infrared radiation. Three years later, Dyakonov and Shur proposed that driven by an external *ac* electric THz field FETs can be used as detectors, mixers and frequency multipliers [114] as well. Nowadays, exploiting the mechanism of Dyakonov and Shur, FETs have proven to be a powerful tool for THz detection and emission (for review see e. g. [110]).

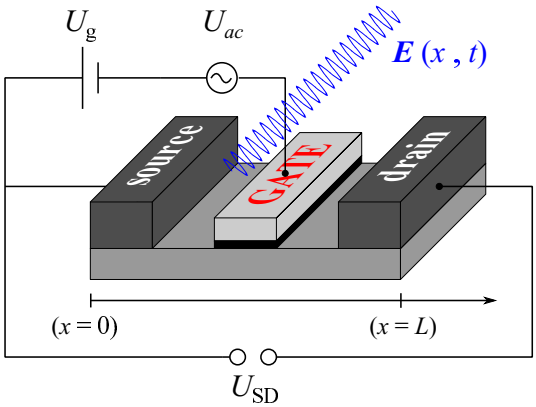

Figure 42: Schematic illustration of a FET operating in detection mode. The *ac* electric field induces an alternating voltage U_{ac} between source and gate electrode. The gate voltage U_g is applied between source and gate. The detector response U_{SD} is induced between source ($x = 0$) and drain ($x = L$) contacts.

The schematic geometry of a FET operating in the detector mode is illustrated in Fig. 42. The external *ac* electric field is fed into the transistor channel and acts as a source of an alternating voltage U_{ac}. In a circuit diagramm, this voltage source is connected in series together with the gate-voltage U_g between the gate and the source-side of the channel ($x = 0$), whereas at the drain side

of the channel ($x = L$), the voltage is zero. Hence, the boundary conditions are:

$$U(0,t) = U_0 + U_a cos(\omega t) = U_0 + U_{ac}, \tag{63}$$

$$j(L,t) = 0. \tag{64}$$

Herein, $U_0 = U_{\mathrm{g}} - U_{\mathrm{th}}$ is the gate-to-channel voltage swing, which is given by the difference in the applied gate voltage U_{g} and the threshold voltage of the transistor channel U_{th}. Equation (64) reveals that the current at the drain side of the channel is zero.
In Ref. [115] the detector response U_{SD} was derived in a hydrodynamic approximation, where the 2D electron gas was treated as a 2D electron fluid. The basic equations describing the 2D electron fluid are the Euler equation,

$$\frac{\partial v_e}{\partial t} + v_e \frac{\partial v_e}{\partial x} = -\frac{e}{m_{eff}} \frac{\partial U_0}{\partial x}, \tag{65}$$

the continuity equation,

$$\frac{\partial U_0}{\partial t} + \frac{\partial (U_0 \cdot v_e)}{\partial x} = 0, \tag{66}$$

and the relationship between the surface carrier concentration n_s and the gate-voltage swing given by

$$n_s = C U_0 / e. \tag{67}$$

In Eq. (65), v_e is the electron velocity, m_{eff} is the effective mass of the electrons and e is the electron charge. Together with Eq. (66) they describe the phenomena of shallow water waves [116] and where used as an analogon to derive the detector response U_{SD}.
As it was discussed in [114], a FET can operate in different regimes which are determined by the product of the radiation frequency ω and the momentum relaxation time τ of the electrons in the channel. For $\omega\tau >> 1$, the damping of the excited plasma oscillations is small and they propagate through the channel. For a short sample, they are reflected at the channel edge and under certain conditions interfere constructively. This results in resonant features of the detector response and can be observed at low temperatures [117].

In the common regime, achieved at room temperature where $\omega\tau$ is much smaller than unity, plasma oscillations are overdamped. They decay close to the drain side of the channel within a characteristic distance denoted as the leakage length $l = \sqrt{2\sigma/\omega C}$, where σ is the conductivity of the channel and C is the gate-to-channel capacitance per unit length. In this regime, U_{SD} becomes a smooth function of the frequency and the transistor acts as a nonresonant broadband THz detector. The detector response was calculated in [118]

$$\frac{U_{\mathrm{SD}}}{U_0} = 1/4 \left(\frac{U_a}{U_0}\right)^2 \cdot f(\omega), \tag{68}$$

and is proportional to U_a^2, in other words to the radiation's intensity. The frequency dependence of the response, $f(\omega)$ looks as follows

$$f(\omega) = 1 + \frac{2\omega\tau}{\sqrt{1+(\omega\tau)^2}} - ..., \tag{69}$$

and is a smooth function of the radiation's frequency in the considered regime of detection.

8.1.2 Sample and Setup

For studies of THz detection by field effect transistors commercially available GaAs/AlGaAs high electron mobility transistors (HEMTs), Fujitsu FHX45X [119], were investigated. The transistor channel has a gate length L_{g} of 150 nm and a gate width W_{g} of 280 μm. The dimensions of the device are shown in Fig. 43 where the position of source (S), drain (D) and two gate (G) pads is sketched. For optical experiments, the HEMTs were glued on a 14 PIN socket and connected to the contact pads with bonding wires.

The channel transfer characteristic determined for a source-drain voltage U_{SD} of 100 mV is shown in Fig. 43. At zero gate bias, the channel is open and the current is in the order of 10 mA. By applying a negative gate voltage the current decreases and the channel closes at a threshold voltage U_{th} of around -500 mV.

Most of the experiments were carried out at the pulsed optically pumped molecular THZ laser presented in section 3.3. In addition, a *cw* methanol THz laser was used providing a single line at 2.5 THz. The setup of this laser is depicted in Fig. 44. The continuous radiation is modulated with the help of an optical chopper in order to use lock-in amplifiers. The photoinduced signals are directly fed into the amplifiers via an 10 MΩ input resistance and synchronized with the reference signal supplied from the chopper system. The lock-in amplifiers are connected by GPIB to a computer which collects the data. All other components are aligned similar to the beam stage of the pulsed laser and calibration as well as beam profiling can be done in the same way.

Furthermore, in order to study the FET response also in the microwave range a commercially available Gunn diode from Spacek labs. Inc. providing frequencies between 80 and 110 GHz served for illumination. The radiation can be modulated with a PIN-switch diode in order to use lock-in technique as described above. The output power of the device is typically in the order of 10 mW.

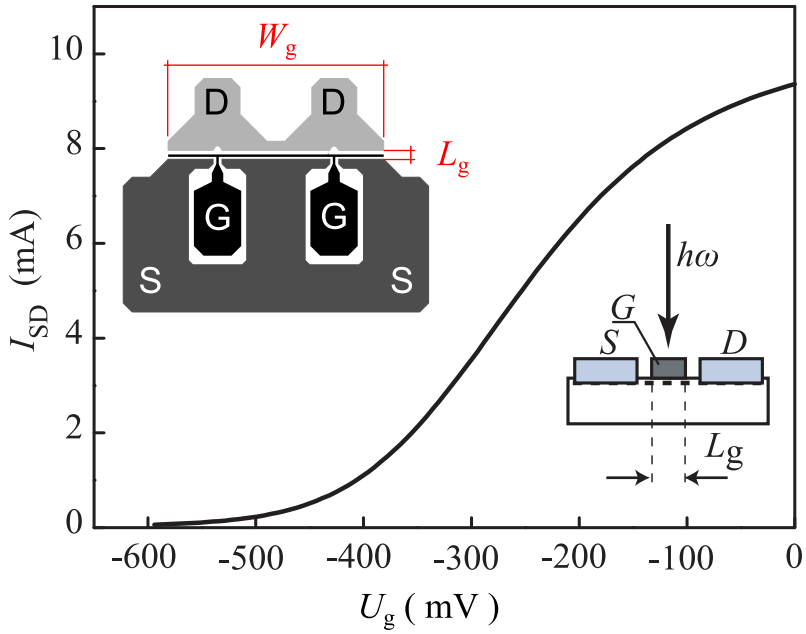

Figure 43: Transfer characteristic of GaAs/AlGaAs HEMT measured at U_{SD} = 100 mV. Insets shows channel dimensions and contact pads for source (S), drain (D) and gate (G) contacts.

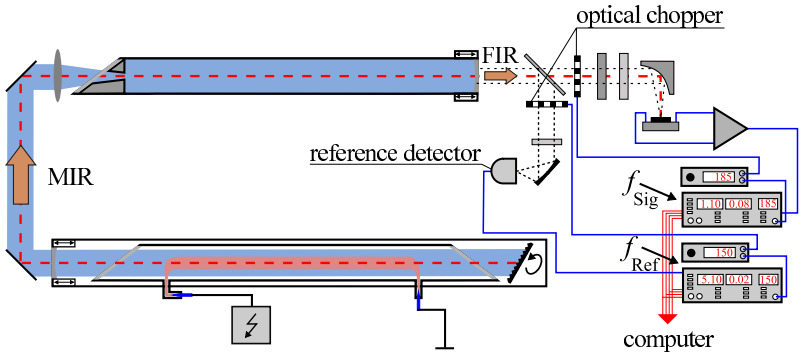

Figure 44: Setup of the *cw* methanol laser.

8.1.3 Experimental Results

The scheme of the photoresponse measurements of the biased field effect transistors is depicted in Fig. 45 (b). The photovoltage U_{SD} between source and drain contacts is measured as a voltage drop over a 50 Ω load resistor.

The illumination with linearly polarized radiation results in a photovoltage which depends strongly on the gate-bias U_g. Fig. 45 (a) shows the gate voltage dependencies of the GaAs/AlGaAs-HEMT's photoresponse measured at different radiation frequencies in the range of 0.1 to 2.5 THz. For all frequencies, only a small response is observed at zero gate bias which increases by applying a negative gate-voltage. For the lowest frequencies, U_{SD} shows a maximum at $U_g \approx -450$ mV which is close to the threshold voltage (see Fig. 45 (c)). The maximum shifts to lower values of U_g for higher frequencies. The data also show that at high frequencies, the signal switches its polarity at a certain value of U_g and the gate-bias of the inversion point diminishes with raising frequency. The curve obtained for 0.1 THz is given in arbitrary units on the right hand scale. The left ordinate shows that in general, the detector response decreases with increasing frequency (curves for 1.1, 2.0 and 2.5 THz are multiplied by integer factors 5, 2 and 10, respectively). Here it's worth mentioning that the detector response saturates at high radiation intensities. This problem was addressed recently in Ref. [120] and is out scope of this thesis. For all presented measurements, the detector response is studied in the linear dynamic range where it shows a linear dependence on the radiation's intensity.

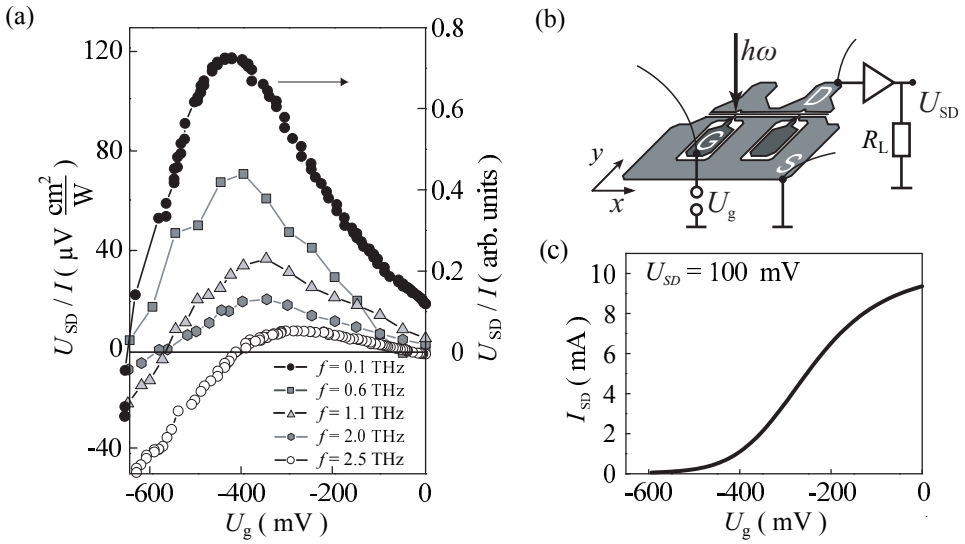

Figure 45: (a) Gate voltage dependence of the photovoltage induced in the GaAs/AlGaAs-HEMT by linearly polarized radiation. The data for frequencies f = 1.1, 2.0, 2.5 THz are multiplied by factors 5, 2, 10, respectively. The signals are read out after the inverting amplifier with a voltage amplification of 20 dB. The upper curve measured with the Gunn oscillator at 0.1 THz refers to the right ordinate, (b) Experimental geometry, (c) transfer characteristic of the GaAs/AlGaAs-HEMT.

A peculiar dependence on the orientation of the electric field vector is obtained by varying the linear polarization state with a half-wave plate. The final result is shown in Fig. 46 for various frequencies and gate voltages. For the special design of the GaAs/AlGaAs-HEMT, a maximum at $\alpha \approx 45°$ and a minimum at $\alpha \approx -45°$ is observed by excitation with 0.1 and 1.1 THz and a gate bias close to the threshold of the device (see left inset in Fig. 46). These two dependencies can be fitted after

$$U_{\mathrm{SD}} = U_1(U_{\mathrm{g}}, f)\cos^2(\alpha + \theta_1), \tag{70}$$

where α is the azimuth angle defined in the right inset of Fig. 46, and θ_1 is the phase angle, depending on the special alignment/geometry of bonding wires and metalization pads. A good agreement of the angular dependence is achieved with $U_1(U_{\mathrm{g}}, f) > 0$ and the value of the phase angle $\theta_1 = 47°$.
However, at higher values of U_{g} the dependency changes (see main panel of

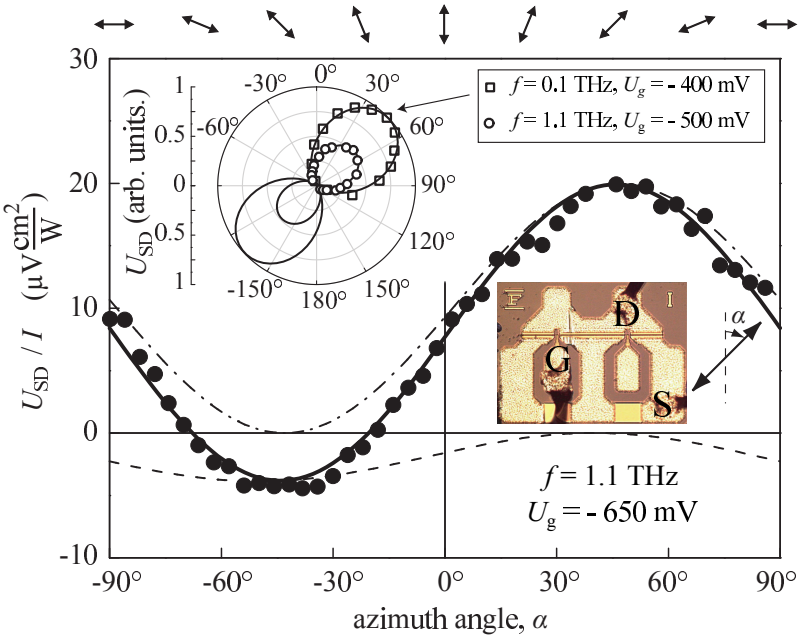

Figure 46: Photovoltage as a function of the azimuth angle α. Solid line shows the fit to Eq. (71). The dot-dashed and dashed lines display individual contributions proportional to $U_1(U_g, f)$ and $U_2(U_g, f)$, respectively. The left inset shows the polar plot of $U_{SD}(\alpha)$ measured for $f = 0.1$ THz, $U_g = -400$ mV (squares) and $f = 1.1$ THz, $U_g = -500$ mV (open circles) together with the corresponding fits to Eq. (70). The maximal signals for $f = 0.1$ THz and 1.1 THz are normalized to 1 and 0.5, respectively. The right inset shows the picture of the transistor with bonding wires and defines the angle α. On top the polarization direction corresponding to various azimuth angles is plotted.

Fig. 46). A negative photoresponse is present at $\alpha = -45°$ and a fit after Eq. (70) is not valid any more. In order to interpret the experimental data the photoinduced signal can be represented as a sum of two contributions:

$$U_{SD} = U_1(U_g, f)\cos^2(\alpha + \theta_1) + U_2(U_g, f)\cos^2(\alpha + \theta_2), \tag{71}$$

with U_1 $(U_g,\ f)$ and U_2 $(U_g,\ f)$ being of opposite sign. The sign of $U_1(U_g, f)$ and the value of the phase angle $\theta_1 = 47°$ introduced above remain unchanged for all applied gate voltages. However, at high gate voltages a second contri-

bution appears showing a negative value of $U_2(U_g, f)$ and $\theta_2 \approx -50°$. The two contributions are indicated by the dashed lines in Fig. 46.

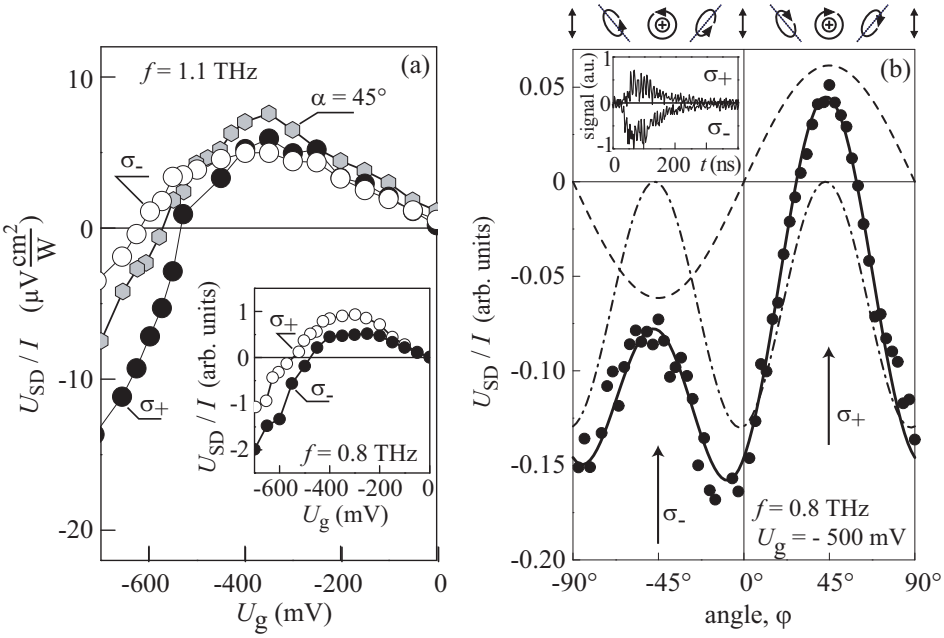

Figure 47: (a) Photoresponse as a function of the gate voltage, measured for right- (σ_+) and left- (σ_-) circularly polarized radiation with $f = 1.1$ THz. Inset shows the data for $f = 0.8$ THz. This data are normalized by the maximum signal in response to σ_+ radiation. (b) Helicity dependence of the photovoltage measured for radiation with $f = 0.8$ THz. Solid line shows the fit to Eq. (72). The dashed and dot-dashed lines display individual contributions proportional to the parameters U_A and U_B, respectively. The ellipses on top illustrate the polarization states for various values of φ. The inset shows the photosignal pulse traces measured for σ_+ and σ_- radiation.

Besides the dependence upon variation of the linear polarization plane, the photoresponse shows also sensitivity to the radiation's helicity. Fig. 47 (a) shows U_{SD} versus the gate voltage measured for right (σ_+) and left (σ_-) handed circularly polarized radiation at $f = 0.8$ (inset) and 1.1 THz (main panel), respectively. The data show that at relatively low bias voltages, for which a dominating contribution of the signal proportional to $U_1(U_g, f)$ is detected, the photoresponse is insensitive to the radiation's helicity. At higher negative bias

voltages, however, the values and even the sign of the signal becomes different for σ_+ and σ_- polarized radiation.
An overall dependence on the variation of the radiation's ellipticity is shown in Fig. 47 (b). The result can be well reproduced by the equation:

$$U_{\mathrm{SD}} = U_{\mathrm{A}}(U_{\mathrm{g}}, f)\sin(2\varphi) + U_{\mathrm{B}}(U_{\mathrm{g}}, f)\cos^2(2\varphi + \theta) + U_{\mathrm{C}}, \tag{72}$$

with U_{A}, U_{B}, U_{C} and θ as the fitting parameters. This equation shows that the photoresponse is caused by a superposition of i) the signal proportional to the degree of circular polarization $P_{\mathrm{circ}} = i(E_y E_x^* - E_x E_y^*)/\left|E\right|^2 = \sin 2\varphi$ (first term) and ii) signals determined by the degree of linear polarization of elliptically polarized light (second term) which vanish if the radiation is circularly polarized. Here, $\boldsymbol{E}$ is the radiation's electric field. The inset in Fig. 47 (b) shows the typical photoresponse pulses for right- and left-handed circularly polarized radiation. The pulse traces demonstrate that the transistor allows the time resolved detection of a fine structure of the laser pulses with short spikes of the order of nanoseconds. The response time of the transistor is limited by the time resolution of the setup and thus, it is 2 ns or less. The same response times were observed at $U_{\mathrm{g}} = U_{\mathrm{th}}$. The time constant is given by the cut-off frequency which is 10 GHz. The practically achievable time resolution, however, is RC-limited by the design of the electric circuitry and by the bandwidth of cables and amplifiers.
While the detector response to linearly polarized radiation and it's angular dependence has been discussed recently by several groups, the helicity sensitive detection of THz radiation by FETs has not been reported so far. In the following, it will be shown that the observed photoresponse, as well as its polarization dependence can be well described in the frame of the generalized model of THz detection by FETs which was introduced above.

8.1.4 Theory and Discussion

Following chapter 8.1.1, at room temperature the field effect transistor acts as nonresonant detector. Indeed, estimations reveal that for the experimental conditions the value of $\omega\tau$ is between 0.04 and 1 and hence, plasma oscillations are overdamped and decay in the vicinity of the source or drain contact.

In order to achieve a nonresonant detector signal, the radiation needs to be coupled to the transistor channel through either the source-gate or drain-gate contacts to induce an alternating voltage. Since the channel length of the investigated FETs is much shorter than the radiation's wavelength, there is no direct interaction of the electromagnetic radiation with the electron gas in the channel and the radiation needs to be coupled by effective antennas formed by the metallic contact pads and/or bonding wires.
In the case when the radiation is coupled solely to one end of the channel, for instance to the drain end, it induces an *ac* voltage with an amplitude U_{d} between the drain- and gate-contacts and the photoresponse is given by $U_{\mathrm{SD}} = U_{\mathrm{d}}^2 \cdot F(U_{\mathrm{g}})$ [110]. Herein, $F(U_{\mathrm{g}})$ describes the dependence of the response on the gate voltage and is valid for positive values of the gate voltage swing, $U_{\mathrm{g}} - U_{\mathrm{th}}$, which are not too close to zero. The amplitude of the input *ac* voltage U_{d} is related to the incoming radiation intensity I and the antenna's sensitivity $\beta_{\mathrm{d}}(\omega)$ as $U_{\mathrm{d}}^2 = \beta_{\mathrm{d}}(\omega) \cdot I$. Thus, the photoresponse can be presented in the form

$$U_{\mathrm{SD}} = \beta_{\mathrm{d}}(\omega) \cdot F_{\mathrm{d}}(U_{\mathrm{g}}) \cdot I. \tag{73}$$

So far, it was considered that the radiation induces an *ac* voltage only at one end of the channel. In order to interpret the experimental results, the radiation is assumed to be coupled to both, the source-gate and the drain-gate contacts. Consequently, the coupling of the radiation to the transistor channel can be modeled by two effective antennas, one of them producing an *ac* voltage between drain and gate (U_{d}) as considered above, and another one between source and gate (U_{s}) which are of opposite sign. The resulting *ac* currents, induced at the opposite ends of the channel, will decay within the characteristic leakage length l. If the gate length of the device L_{g} is much larger than the leakage length l, the photovoltage is generated in a region on the order of l near the contact and there is no interference between the currents induced at opposite sides of the channel. Hence, the corresponding contributions to the total photoresponse are independent and of opposite polarity. The total photoresponse is given by the superposition of both contributions:

$$U_{\mathrm{SD}}(U_{\mathrm{g}}) = [\beta_{\mathrm{s}}(\omega) F_{\mathrm{s}}(U_{\mathrm{g}}) + \beta_d(\omega) F_{\mathrm{d}}(U_{\mathrm{g}})] \cdot C(\omega) \cdot I, \tag{74}$$

where $C(\omega)$ is the parameter describing the frequency dependence of the photoresponse, whereas β_s and β_d are frequency dependent sensitivities of the source-gate and drain-gate effective antennas, respectively. The functions $F_d(U_g)$ and $F_s(U_g)$ describe the gate bias dependencies of the photoresponse generated at the source and drain sides of the channel.
In Ref. [113] it was shown that at low frequencies (< 100 GHz) the radiation is coupled to the transistor mainly by bonding wires, whereas at higher frequencies (> 100 GHz) the metalization of the contact pads plays the role of the antennas. From Fig. 46 it follows that at $f = 0.1$ THz the photoresponse exhibits a maximum when the radiation polarization is aligned along the line connecting the gate and drain contact wires (see inset) giving rise to the assumption that at low frequencies the radiation is basically coupled to the drain side of the channel. Hence, the upper curve in Fig. 48 can be attributed to the photoresponse generated at the drain side only, $F_d(U_g)$, i.e. β_d (0.1 THz) $= 1$ and β_s (0.1 THz) $= 0$. In contrast, at high frequencies, the radiation is expected to be coupled to the channel primarily through the contact metallic pads. This enables coupling to the source side of the channel which, obviously, should lead to an opposite sign of the signal. Indeed, the photoresponse at 2.5 THz is negative in most of the gate voltage range.

In order to reproduce the experimental data with Eq. (74), $F_s(U_g)$ is chosen to be negative in the whole range of U_g and represented by the dashed line in Fig. 48 (b). This function describes the case where the radiation is solely coupled to the source side of the channel, i.e. $\beta_d = 0$ and $\beta_s = 1$. By choosing $F_d(U_g)$ and $F_s(U_g)$ in these forms, the detector response for each frequency can be calculated after Eq. (74). A good agreement between the calculations, shown in Fig. 48 (b), and the experimental results, adapted from Fig. 45 and shown in panel (a), is achieved with that assumptions. The inset in Fig. 48 demonstrates that the increase of the radiation frequency consistently decreases the efficiency of the drain-gate antenna, $\beta_d(\omega)$, and increases the coupling by the source-gate antenna, $\beta_s(\omega)$. At intermediate frequencies the photoresponse is a superposition of two signals generated at the drain- and the source-side of the channel. This becomes also apparent in experiments with linear polarization of radiation. As seen in Fig. 46, at a frequency of 1.1 THz and $U_g = -650$ mV, the polarization dependence of the photoresponse is well

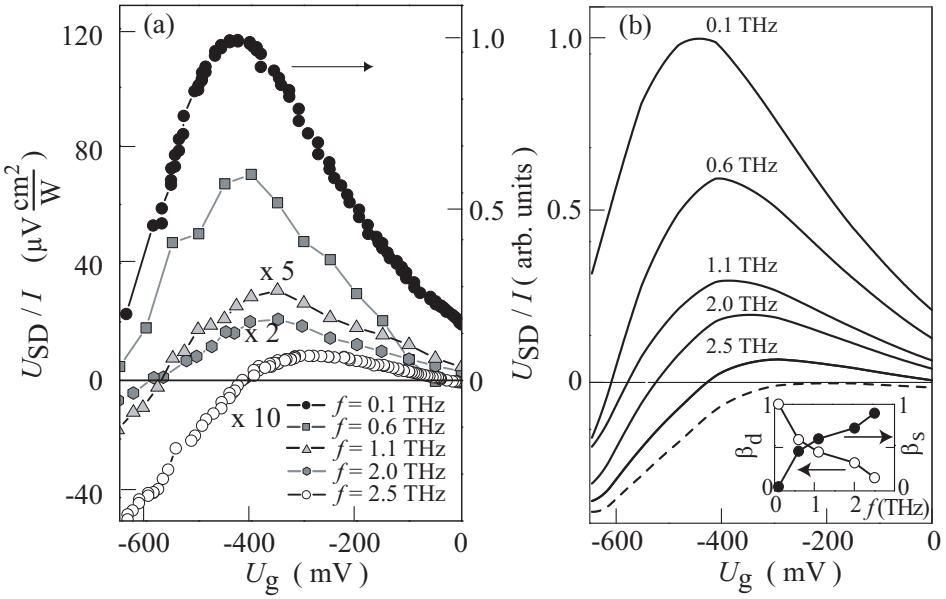

Figure 48: (a) Experimental results adapted from Fig. 45 for comparison. (b) Gate voltage dependence calculated after Eq. (74) and assuming $C(\omega) = 1$. The inset shows fitting parameters $\beta_{\rm s}(f)$ and $\beta_{\rm d}(f)$ as a function of the radiation frequency.

fitted by the sum of the two contributions (dot-dashed and dashed curves). The existence of two photosignals at opposite ends of the channel may also explain the helicity dependent photoresponse. So far, the case when the leakage length l is sufficiently small compared to $L_{\rm g}$ was assumed. In that situation, the *ac* currents generated at both sides of the channel do not interfere. However, if l is of the order of the half of the gate-length, $l \approx L_{\rm g}/2$, there is a region where the *ac* currents generated at the source and drain could coexist. It was shown in Ref. [121] that in this case the *ac* current resulting from the interference of the two independently induced currents is sensitive to their phase difference, ξ. Such a phase difference is present when source- and drain-antennas are excited by orthogonal electric fields of circularly (or elliptically) polarized radiation. In the investigated structures, source- and drain-effective antennas show maximal sensitivity for polarization directions differing by about 90°. Consequently, the *ac* currents generated at source and drain will interfere and have a phase shift

ξ. It was shown by in Ref. [121] that, if L_g is comparable to l, Eq. (74) modifies to:

$$\Delta U = \Big[\beta_\mathrm{s}(\omega)\cdot F_\mathrm{s}(U_\mathrm{g}) + \beta_\mathrm{d}(\omega)\cdot F_\mathrm{d}(U_\mathrm{g}) + \sqrt{\beta_\mathrm{s}(\omega)\cdot F_\mathrm{s}(U_\mathrm{g})\beta_\mathrm{d}(\omega)\cdot F_\mathrm{d}(U_\mathrm{g})}\sin(\xi)\exp(-L_\mathrm{g}/l)\Big]\cdot I\ , \tag{75}$$

where the last interference term is sensitive to the radiation's helicity (sign of ξ) and the characteristic leakage length l. In the case of linearly polarized radiation ξ equals zero and Eq. (75) reduces to Eq. (74).
Under the present experimental conditions, the characteristic length is frequency dependent and can be estimated to 76 nm (0.8 THz) and 89 nm (1.1 THz) being in the same order as the half of the gate length $L_g = 150$ nm. Hence, the *ac* currents induced at opposite ends of the channel can interfere and the detector response becomes sensitive to the radiation's helicity. As it follows from Fig. 48, for $f = 1.1$ THz the contributions of source-gate and drain-gate antenna become equal at $U_\mathrm{g} = -565$ mV, where $\beta_\mathrm{s}(\omega)\cdot F_\mathrm{s}(U_\mathrm{g}) \approx \beta_\mathrm{d}(\omega)\cdot F_\mathrm{d}(U_\mathrm{g})$. Thus, only the interference term in Eq. 75 remains and the photoresponse is expected to change its sign when the helicity of the radiation is reversed. Exactly this is observed at 1.1 THz in Fig. 47(a) and also at 0.8 THz in Fig. 47(b).

8.1.5 Conclusion

To summarize, a helicity dependent contribution to the photoresponse of a FET was observed by illumination with circularly polarized radiation. In particular, signals of opposite polarity for right- and left handed circularly polarized radiation was observed. The observation gives rise to an extension of the model from Dyakonov and Shur in such a way that the radiation is fed by two orthogonal antennas to both ends of the transistor channel inducing *ac* currents of opposite sign which interfere in a short device ($l \approx L_g/2$). The interference is sensitive to the phase shift between the two currents and hence, to the helicity of the radiation.
Consequently, (i) the optimization of the transistor design and (ii) the proper choice of the gate voltage, for which the response due to the linearly polarized radiation vanishes, should allow the construction of a detector element with the responsivity just proportional to the radiation helicity, i.e. to the corresponding fourth Stokes parameter. Combining such a detector element with two conventional FETs yielding a response to the linearly polarized radiation and, consequently, to the remaining Stokes parameters should permit the complete characterization of radiation polarization in an all-electric manner. By the proper choice of the gate voltage, such room temperature detectors can be tuned to any radiation frequency in the THz range and are characterized by a nanosecond time resolution.
Such a detector system for the all electric detection of the radiation's polarization state was developed based on the linear- and circular photogalvanic effect in semiconductor nanostructures [122]. However, the observed transistor photoresponse is by several orders of magnitude higher than that one of the existing system. Thus, the field effect transistors could be used for a polarization detector system with much higher sensitivity. Finally, just recently the graphene based field effect transistors were realized for THz detection [123]. With its high electron mobility, the graphene-FETs may serve as resonant detectors even at room temperature. Therefore, the realization of a graphene based polarization detector system might be a promising future task for THz ellipsometry.

References

[1] K. S. Novoselov, A. K. Geim, S. V. Morozov, D. Jiang, Y. Zhang, S. V. Dubonos, I. V. Grigorieva, and A. A. Firsov, *Electric Field Effect in Atomically Thin Carbon Films*, Science **306**, 666 (2004).

[2] P. R. Wallace, *The Band Theory of Graphite*, Phys. Rev. **71**, 622 (1947).

[3] K. S. Novoselov, A. K. Geim, S. V. Morozov, D. Jiang, M. I. Katsnelson, I. V. Grigorieva, S. V. Dubonos, and A. A. Firsov, *Two-dimensional gas of massless Dirac fermions in graphene*, Nature **438**, 197 (2005).

[4] C. Berger, Z. Song, X. Li, X. Wu, N. Brown, C. Naud, D. Mayou, T. Li, J. Hass, A. N. Marchenkov, E. H. Conrad, P. N. First, and W. A. de Heer, *Electronic Confinement and Coherence in Patterned Epitaxial Graphene*, Science **312**, 1191 (2006).

[5] F. V. Tikhonenko, D. W. Horsell, R. V. Gorbachev, and A. K. Savchenko, *Weak Localization in Graphene Flakes*, Phys. Rev. Lett. **100**, 056802 (2008).

[6] S. V. Morozov, K. S. Novoselov, M. I. Katsnelson, F. Schedin, L. A. Ponomarenko, D. Jiang, and A. K. Geim, *Strong Suppression of Weak Localization in Graphene*, Phys. Rev. Lett. **97**, 016801 (2006).

[7] X. Wu, X. Li, Z. Song, C. Berger, and W. A. de Heer, *Weak Antilocalization in Epitaxial Graphene: Evidence for Chiral Electrons*, Phys. Rev. Lett. **98**, 136801 (2007).

[8] Y. Zhang, Y.-W. Tan, H. L. Stormer, and P. Kim, *Experimental observation of the quantum Hall effect and Berry's phase in graphene*, Nature **438**, 201 (2005).

[9] K. S. Novoselov, Z. Jiang, Y. Zhang, S. V. Morozov, H. L. Stormer, U. Zeitler, J. C. Maan, G. S. Boebinger, P. Kim, and A. K. Geim,

Room-Temperature Quantum Hall Effect in Graphene, Science **315**, 1379 (2007).

[10] A. Rycerz, J. Tworzydlo, and C. W. J. Beenakker, *Valley filter and valley valve in graphene*, Nature Phys. **3**, 172 (2007).

[11] O. Klein, *Die Reflexion von Elektronen an einem Potentialsprung nach der relativistischen Dynamik von Dirac*, Z. Phys. **53**, 157 (1929).

[12] M. I. Katsnelson, K. S. Novoselov, and A. K. Geim, *Chiral tunneling and the Klein paradox*, Nature Phys. **2**, 620 (2006).

[13] A. F. Young and P. Kim, *Quantum interference and carrier collimation in graphene heterojunctions*, Nature Phys. **5**, 222 (2009).

[14] N. Stander, B. Huard, and D. Goldhaber-Gordon, *Evidence for Klein Tunneling in Graphene p-n Junctions*, Phys. Rev. Lett. **102**, 026807 (2009).

[15] A. H. Castro Neto, F. Guinea, N. M. R. Peres, K. S. Novoselov, and A. K. Geim, *The electronic properties of graphene*, Rev. Mod. Phys. **81**, 109 (2009).

[16] S. Das Sarma, S. Adam, E. H. Hwang, and E. Rossi, *Electronic transport in two-dimensional graphene*, Rev. Mod. Phys. **83**, 407 (2011).

[17] M. O. Goerbig, *Electronic properties of graphene in a strong magnetic field*, Rev. Mod. Phys. **83**, 1193 (2011).

[18] K. S. Novoselov, V. I. Fal'ko, L. Colombo, P. R. Gellert, M. G. Schwab, and K. Kim, *A roadmap for graphene*, Nature **490**, 192 (2012).

[19] S. D. Ganichev and W. Prettl, *Intense Terahertz Excitation of Semiconductors*. Oxford Univ. Press, Oxford, 2006.

[20] E. L. Ivchenko, *Optical Spectroscopy of Semiconductor Nanostructures*. Alpha Science Int., Harrow, 2005.

[21] A. Jorio, G. Dresselhaus, and M. S. Dresselhaus (Eds.), *Advanced Topics in the Synthesis, Structure, Properties and Applications*. Springer, 2008.

[22] S. A. Mikhailov, *Non-linear electromagnetic response of graphene*, Euro. Phys. Lett. **79**, 27002 (2007).

[23] J. J. Dean and H. M. van Driel, *Second harmonic generation from graphene and graphitic films*, Appl. Phys. Lett. **95**, (2009).

[24] M. M. Glazov, *Second Harmonic Generation in graphene*, Pis'ma v. ZhETF **93**, 408 (2011).

[25] M. Dragoman, D. Neculoiu, G. Deligeorgis, G. Konstantinidis, D. Dragoman, A. Cismaru, A. A. Muller, and R. Plana, *Millimeter-wave generation via frequency multiplication in graphene*, Appl. Phys. Lett. **97**, (2010).

[26] L. Prechtel, L. Song, D. Schuh, P. Ajayan, W. Wegscheider, and A. W. Holleitner, *Time-resolved ultrafast photocurrents and terahertz generation in freely suspended graphene*, Nature Comm. **3**, 646 (2012).

[27] M. Graham, S. F. Shi, D. C. Ralph, J. Park, and P. L. McEuen, *Photocurrent measurements of supercollision cooling in graphene*, Nature Phys. **9**, 103 (2013).

[28] J. Karch, P. Olbrich, M. Schmalzbauer, C. Zoth, C. Brinsteiner, M. Fehrenbacher, U. Wurstbauer, M. M. Glazov, S. A. Tarasenko, E. L. Ivchenko, D. Weiss, J. Eroms, R. Yakimova, S. Lara-Avila, S. Kubatkin, and S D. Ganichev, *Dynamic Hall Effect Driven by Circularly Polarized Light in a Graphene Layer*, Phys. Rev. Lett. **105**, 227402 (2010).

[29] C. Jiang, V. A. Shalygin, V. Yu. Panevin, S. N. Danilov, M. M. Glazov, R. Yakimova, S. Lara-Avila, S. Kubatkin, and S. D. Ganichev, *Helicity-dependent photocurrents in graphene layers excited by midinfrared radiation of a CO_2 laser*, Phys. Rev. B **84**, 125429 (2011).

[30] M. M. Glazov and S. D. Ganichev, *High frequency electric field induced nonlinear effects in graphene*, Phys. Reports **535**, 101–138 (2014).

[31] Reimann P., *Brownian motors:noisy transport far from equilibrium*, Phys. Reports **361**, 57–265 (2002).

[32] P. Hänggi and F. Marchesoni, *Artificial Brownian motors: Controlling transport on the nanoscale*, Rev. Mod. Phys. **81**, 387–442 (2009).

[33] A. Bostwick, T. Ohta, T. Seyller, K. Horn, and E. Rotenberg, *Quasiparticle dynamics in graphene*, Nature Phys. **3**, 36 (2007).

[34] R. R. Nair, P. Blake, A. N. Grigorenko, K. S. Novoselov, T. J. Booth, T. Stauber, N. M. R. Peres, and A. K. Geim, *Fine Structure Constant Defines Visual Transparency of Graphene*, Science **320**, 1308 (2008).

[35] A. M. Fox, *Optical Properties of Solids.* Oxford Univ. Press, Oxford, 2007.

[36] A. V. Ioffe and A. F. Ioffe, *Photoelectromotive forces in cubrite crystals*, Zh. Èksp. Teor. Fiz. **5**, 112 (1935). (in Russian).

[37] H. M. Barlow, *Application of the Hall effect in a semiconductor to the measurement of power in an electromagnetic field*, Nature **173**, 41 (1954).

[38] M. V. Entin, L. I. Magarill, and D. L. Shepelyansky, *Theory of resonant photon drag in monolayer graphene*, Phys. Rev. B **81**, 165441 (2010).

[39] A. M. Glass, D. von der Linde, and T. J. Negran, *High-voltage bulk photovoltaic effect and the photorefractive process in $LINbO_3$*, Appl. Phys. Lett. **25**, 233 (1974).

[40] P. Olbrich, S. A. Tarasenko, C. Reitmaier, J. Karch, D. Plohmann, Z. D. Kvon, and S. D. Ganichev, *Observation of the orbital circular photogalvanic effect*, Phys. Rev. B **79**, 121302 (2009).

[41] A. Zunger, *Self-consistent LCAO calculation of the electronic properties of graphite. I. The regular graphite lattice*, Phys. Rev. B **17**, 626 (1978).

[42] V. V. Bel'kov, S. D. Ganichev, E. L. Ivchenko, S. A. Tarasenko, W. Weber, S. Giglberger, M. Olteanu, H.-P. Tranitz, S. N. Danilov, P. Schneider, W. Wegscheider, D. Weiss, and W. Prettl, *Magneto-gyrotropic photogalvanic effects in semiconductor quantum wells*, J. Phys.: Condens. Matter **17**, 3405 (2005).

[43] S. D. Ganichev, S. A. Tarasenko, V. V. Bel'kov, P. Olbrich, W. Eder, D. R. Yakovlev, V. Kolkovsky, W. Zaleszczyk, G. Karczewski, T. Wojtowicz, and D. Weiss, *Spin Currents in Diluted Magnetic Semiconductors*, Phys. Rev. Lett. **102**, 156602 (2009).

[44] S. A. Tarasenko, *Electron scattering in quantum wells subjected to an in-plane magnetic field*, Phys. Rev. B **77**, 085328 (2008).

[45] S. D. Ganichev, V. V. Bel'kov, S. A. Tarasenko, S. N. Danilov, S. Giglberger, Ch. Hoffmann, E. L. Ivchenko, D. Weiss, W. Wegscheider, Ch. Gerl, D. Schuh, J. Stahl, J. De Boeck, G. Borghs, and W. Prettl, *Zero-bias spin separation*, Nature Phys. **2**, 609 (2006).

[46] C. Drexler, V. V. Bel'kov, B. Ashkinadze, P. Olbrich, C. Zoth, V. Lechner, Ya. V. Terent'ev, D. R. Yakovlev, G. Karczewski, T. Wojtowicz, D. Schuh, W. Wegscheider, and S. D. Ganichev, *Spin polarized electric currents in semiconductor heterostructures induced by microwave radiation*, Appl. Phys. Lett. **97**, 182107 (2010).

[47] V. Lechner, L. E. Golub, F. Lomakina, V. V. Bel'kov, P. Olbrich, S. Stachel, I. Caspers, M. Griesbeck, M. Kugler, M. J. Hirmer, T. Korn, C. Schüller, D. Schuh, W. Wegscheider, and S. D. Ganichev, *Spin and orbital mechanisms of the magnetogyrotropic photogalvanic effects in $GaAs/Al_xGa_{1-x}As$ quantum well structures*, Phys. Rev. B **83**, 155313 (2011).

[48] T. Y. Chang and J. D. McGee, *Laser action at 452, 296, and 541 μm in optically pumped CH_3F*, Optics Commun. **1**, 423 (1969).

[49] L. R. Elias, G. Ramian, J. Hu, and A. Amir, *Observation of Single-Mode Operation in a Free-Electron Laser*, Phys. Rev. Lett. **57**, 424 (1986).

[50] A. Crocker, H. A. Gebbie, M. F. Kimmitt, and L. E. S. Mathias, *Stimulated Emission in the far infra-red*, Nature **201**, 250 (1964).

[51] H. A. Gebbie, N. W. B. Stone, F. D. Findlay, and J. A. Robb, *Interferometric Observation on Far Infra-red Stimulated Emsiion Source*, Nature **202**, 170 (1964).

[52] T. A. DeTemple, *Pulsed Optically Pumped Far Infrared Lasers.* in Infrared and Millimeter Waves, Vol.1, Sources of Radiation, ed. K. J. Button, Academic Press, New York, 1979.

[53] F. K. Kneubühl and M. W. Siegrist, *Laser.* Teubner, Stuttgart, 1988.

[54] T. Y. Chang and J. D. McGee, *Off-resonant infrared laser action in NH3 and C2H4 without population inversion*, Appl. Phys. Lett. **29**, 725 (1976).

[55] D. G. Biron, R. J. Temkin, B. Lax, and B. G. Danly, *High-intensity CO_2 laser pumping of a CH_3F Raman FIR laser*, Optics Lett. **4**, 381 (1979).

[56] P. Mathieu and J. R. Izatt, *Narrow-Band CO_2 - TEA Laser for Efficient FIR Laser Pumping*, IEEE Journal of Quantum Electronics **13**, (1977).

[57] H. R. Fetterman, P. E. Tannenwald, C. D. Parker, J. Melngailis, R. C. Williamson, P. Woskoboinikow, H. C. Praddaude, and W. J. Mulligan, *Real-time spectral analysis of far-infrared laser pulses using an SAW dispersive delay line*, Appl. Phys. Lett. **34**, (1979).

[58] O. Svelto, *Principles of Lasers.* Plenum Press, New York, 1998.

[59] H. Motz, *Applications of the Radiation from Fast Electron Beams*, J. Appl. Phys. **22**, (1951).

[60] H. Motz, W. Thon, and R. N. Whitehurst, *Experiments on Radiation by Fast Electron Beams*, J. Appl. Phys. **24**, (1953).

[61] J. M. J. Madey, *Stimulated Emission of Bremsstrahlung in a Periodic Magnetic Field*, J. Appl. Phys. **42**, (1971).

[62] C. A. Brau, *Free-Electron Lasers.* Academic Press, New York, 1990.

[63] K. F. Renk, *Basics of Laser Phys.* Springer, Berlin, 2012.

[64] G. M. H. Knippels, X. Yan, A. M. MacLeod, W. A. Gillespie, M. Yasumoto, D. Oepts, and A. F. G. van der Meer, *Generation and Complete Electric-Field Characterization of Intense Ultrashort Tunable Far-Infrared Laser Pulses*, Phys. Rev. Lett. **83**, 1578 (1999).

[65] H. Fujiwara, *Spectroscopic Ellipsometry - Pinciples and Applications.* John Wiley and sons, Chichester, 2003.

[66] E. Born, M. nad Wolf, *Principles of optics.* Cambridge University Press, Cambridge, 1999.

[67] D. Meschede, *Gerthsen Physik, 22. Auflage.* Springer, Berlin, 2004.

[68] E.V. Loewenstein, R.R. Smith, and R.L. Morgan, *Optical Constants of Far Infrared Materials. 2: Crystalline Solids*, Appl. Opt. **12**, 398 (1973).

[69] F. Brehat and B. Wyncke, *Measurement of the Optical Constants of Crystal Quartz at 10 K and 300 K in the Far Infrared Spectral Range*, Int. J. Infrared Milli. **18**, 1663 (1997).

[70] B. E. A. Saleh and M. C. Teich, *Fundamentals of Photonics.* John Wiley and sons, New York, 1991.

[71] E. V. Loewenstein and D. R. Smith, *Optical Constants of Fra Infrared Materials. I: Analysis of Channeled Spectra and Application to Mylar*, Appl. Opt. **10**, 577 (1971).

[72] T. Seyller, *Epitaktisches Graphen*, Phys. Journal **9**, 53 (2010).

[73] X. Li, W. Cai, J. An, S. Kim, J. Nah, D. Yang, R. Piner, A. Velamakanni, I. Jung, E. Tutuc, S. K. Banerjee, L. Colombo, and R. S. Ruoff, *Large-Area Synthesis of High-Quality and Uniform Graphene Films on Copper Foils*, Science **324**, 1312–1314 (2009).

[74] R. Yakimova, C. Virojanadara, D. Gogova, M. Syväjärvi, D. Siche, K. Larsson, and L. I. Johansson, *Analysis of the Formation Conditions for Large Area Epitaxial Graphene on SiC Substrates*, Mater. Sci. Forum **645**, 565–568 (2010).

[75] R. Cheung, *Silicon Carbide Microelectrochemical Systems for Harsh Environments*. Imperial College Press, 2006.

[76] K. V. Emtsev, F. Speck, Th. Seyller, L. Ley, and J. D. Riley, *Interaction, growth, and ordering of epitaxial graphene on SiC0001 surfaces: A comparative photoelectron spectroscopy study*, Phys. Rev. B **77**, 155303 (2008).

[77] S. Lara-Avila, K. Moth-Poulsen, R. Yakimova, T. Bjørnholm, V. Fal'ko, A. Tzalenchuk, and S. Kubatkin, *Non-Volatile Photochemical Gating of an Epitaxial Graphene/Polymer Heterostructure*, Adv. Mater. **23**, 878 (2011).

[78] S. Kopylov, A. Tzalenchuk, S. Kubatkin, and V. I. Fal'ko, *Charge transfer between epitaxial graphene and silicon carbide*, Appl. Phys. Lett. **97**, 112109 (2010).

[79] S. Lara-Avila, A. Tzalenchuk, S. Kubatkin, R. Yakimova, T. J. B. M. Janssen, K. Cedergren, T. Bergsten, and V. Fal'ko, *Disordered Fermi Liquid in Epitaxial Graphene from Quantum Transport Measurements*, Phys. Rev. Lett. **107**, 166602 (2011).

[80] C. Drexler, S. A. Tarasenko, P. Olbrich, M. Karch, J. Hirmer, F. Mueller, M. Gmitra, J. Fabian, R. Yakimova, S. Lara-Avila, S. Kubatkin, M. Wang, R. Vajtai, P. M. Ajayan, J. Kono, and S. D. Ganichev, *Magnetic quantum ratchet effect in graphene*, Nature Nano. **8**, 104 (2013).

[81] V. I. Falko, *Rectifying properties of 2D inversion layers in a parallel magnetic field*, Sov. Phys. Solid State **31**, 561 (1989).

[82] S. A. Tarasenko, *Direct current driven by ac electric field in quantum wells*, Phys. Rev. B **83**, 035313 (2011).

[83] C. Kittel, *Introduction to Solid State Physics*. John Wiley and sons, New York, 1996.

[84] D. W. Boukhvalov, M. I. Katsnelson, and A. I. Lichtenstein, *Hydrogen on graphene: Electronic structure, total energy, structural distortions and magnetism from first-principles calculations*, Phys. Rev. B **77**, 035427 (2008).

[85] S. D. Ganichev, S. A. Tarasenko, J. Karch, J. Kamann, and Z. D. Kvon, *Magnetic quantum ratchet effect in Si-MOSFETs*, arXiv: 1401.0135v1 (2014).

[86] S. Konschuh, M. Gmitra, and J. Fabian, *Tight-binding theory of the spin-orbit coupling in graphene*, Phys. Rev. B **82**, 245412 (2010).

[87] F. Hiebel, P. Mallet, F. Varchon, L. Magaud, and J-Y. Veuillen, *Graphene-substrate interaction on 6H-SiC(*$000\bar{1}$*): A scanning tunneling microscopy study*, Phys. Rev. B **78**, 153412 (2008).

[88] J. Ristein, S. Mammadov, and Th. Seyller, *Origin of Doping in Quasi-Free-Standing Graphene on Silicon Carbide*, Phys. Rev. Lett. **108**, 246104 (2012).

[89] F. Fromm, M. H. Oliveira Jr, A. Molina-Sánchez, M. Hundhausen, J. M. J. Lopes, H. Riechert, L. Wirtz, and T. Seyller, *Contribution of the buffer layer to the Raman spectrum of epitaxial graphene on SiC(0001)*, New J. Phys. **15**, 043031 (2013).

[90] Y. Y. Wang, Z. H. Ni, T. Yu, Z. X. Shen, H. M. Wang, Y. H. Wu, W. Chen, and Andrew T. Shen W., *Raman Studies of Monolayer Graphene: The Substrate Effect*, The Journal of Physical Chemistry C **112**, 10637 (2008).

[91] J. Karch, P. Olbrich, M. Schmalzbauer, C. Brinsteiner, U. Wurstbauer, M. M. Glazov, S. A. Tarasenko, E. L. Ivchenko, D. Weiss, J. Eroms, and S. D. Ganichev, *Photon helicity driven electric currents in graphene*, arXiv: 1002.1047v1 (2010).

[92] J. Karch, C. Drexler, P. Olbrich, M. Fehrenbacher, M. Hirmer, M. M. Glazov, S. A. Tarasenko, E. L. Ivchenko, B. Birkner, J. Eroms, D. Weiss, R. Yakimova, S. Lara-Avila, S. Kubatkin, M. Ostler, T. Seyller, and S. D. Ganichev, *Terahertz Radiation Driven Chiral Edge Currents in Graphene*, Phys. Rev. Lett. **107**, 276601 (2011).

[93] C. Casiraghi, A. Hartschuh, H. Qian, S. Piscanec, C. Georgi, A. Fasoli, K. S. Novoselov, D. M. Basko, and A. C. Ferrari, *Raman Spectroscopy of Graphene Edges*, Nano Lett. **9**, 1433 (2009).

[94] S. Heydrich, M. Hirmer, C. Preis, T. Korn, J. Eroms, D. Weiss, and C. Schüller, *Scanning Raman spectroscopy of graphene antidot lattices: Evidence for systematic p-type doping*, Appl. Phys. Lett. **97**, (2010).

[95] F. Speck, J. Jobst, F. Fromm, M. Ostler, D. Waldmann, M. Hundhausen, H. B. Weber, and Th. Seyller, *The quasi-free-standing nature of graphene on H-saturated SiC(0001)*, Nature Nano. **3**, 486 (2008).

[96] E. J. H. Lee, K. Balasubramanian, R. T. Weitz, M. Burghard, and K. Kern, *Contact and edge effects in graphene devices*, Appl. Phys. Lett. **99**, 122106 (2011).

[97] B. K. Daas, K. M. Daniels, T. S. Sudarshan, and M V. S. Chandrashekar, *Polariton enhanced infrared reflection of epitaxial graphene*, J. Appl. Phys. **110**, 113114 (2011).

[98] P. Olbrich, C. Drexler, L. E. Golub, S. N. Danilov, V. A. Shalygin, R. Yakimova, S. Lara-Avila, S. Kubatkin, B. Redlich, R. Huber, and S. D. Ganichev, *Reststrahl band-assisted photocurrents in epitaxial graphene layers*, Phys. Rev. B **88**, 245425 (2013).

[99] Lyle P. and W. J. Choyke, *Static Dielectric Constant of SiC*, Phys. Rev. B **2**, 2255 (1970).

[100] A. H. Castro Neto and F. Guinea, *Impurity-Induced Spin-Orbit Coupling in Graphene*, Phys. Rev. Lett. **103**, 026804 (2009).

[101] C. Ertler, S. Konschuh, M. Gmitra, and J. Fabian, *Electron spin relaxation in graphene: The role of the substrate*, Phys. Rev. B **80**, 041405 (2009).

[102] B. Birkner, D. Pachniowski, A. Sandner, M. Ostler, T. Seyller, J. Fabian, M. Ciorga, D. Weiss, and J. Eroms, *Annealing-induced magnetic moments detected by spin precession measurements in epitaxial graphene on SiC*, Phys. Rev. B **87**, 081405 (2013).

[103] J. Balakrishnan, G. Kok Wai Koon, M. Jaiswal, A. H. Castro Neto, and B. Ozyilmaz, *Colossal enhancement of spin-orbit coupling in weakly hydrogenated graphene*, Nature Phys. **9**, 284 (2013).

[104] Oleg V. Yazyev and Lothar Helm, *Defect-induced magnetism in graphene*, Phys. Rev. B **75**, 125408 (2007).

[105] R. R. Nair, M. Sepioni, I-L. Tsai, O. Lehtinen, J. Keinonen, A. V. Krasheninnikov, T. Thomson, A. K. Geim, and I. V. Grigorieva, *Spin-half paramagnetism in graphene induced by point defects*, Nature Phys. **8**, 199 (2012).

[106] T. Oka and H. Aoki, *Photovoltaic Hall effect in graphene*, Phys. Rev. B **79**, 081406 (2009).

[107] Z. Gu, H. A. Fertig, D. P. Arovas, and A. Auerbach, *Floquet Spectrum and Transport through an Irradiated Graphene Ribbon*, Phys. Rev. Lett. **107**, 216601 (2011).

[108] L. Solymar and E. Shamonina, *Waves in Metamaterials*. Oxford University Press, New York, 2009.

[109] C. Drexler, T. V. Shishkanova, C. Lange, S. N. Danilov, D. Weiss, S. D. Ganichev, and V. M. Mirsky, *Terahertz split-ring metamaterials as transducers for chemical sensors based on conducting polymers: a feasibility study with sensing of acidic and basic gases using polyaniline chemosensitive layer*, Microchimica Acta 1–6 (2014).

[110] M. I. Dyakonov, *Generation and detection of Terahertz radiation by field effect transistors*, C. R. Phys. **11**, 413 (2010).

[111] W Knap, F Teppe, N Dyakonova, D Coquillat, and J Łusakowski, *Plasma wave oscillations in nanometer field effect transistors for terahertz detection and emission*, J. Phys.: Condens. Matter **20**, 384205 (2008).

[112] F. Schuster, D. Coquillat, H. Videlier, M. Sakowicz, F. Teppe, L. Dussopt, B. Giffard, T. Skotnicki, and W. Knap, *Broadband terahertz imaging with highly sensitive silicon CMOS detectors*, Opt. Express **19**, 7827 (2011).

[113] M. Sakowicz, J. Łusakowski, K. Karpierz, M. Grynberg, W. Knap, and W. Gwarek, *Polarization sensitive detection of 100 GHz radiation by high mobility field-effect transistors*, J. Appl. Phys. **104**, 024519 (2008).

[114] M. I. Dyakonov and M. S. Shur, *Detection, Mixing and Frequency Multiplication of Terahertz Radiation by Two-Dimensional Electronic Fluid*, IEEE Trans. Electron. Devices **43**, 380 (1996).

[115] M. Dyakonov and M. Shur, *Shallow water analogy for a ballistic field effect transistor: New mechanism of plasma wave generation by dc current*, Phys. Rev. Lett. **71**, 2465 (1993).

[116] L. D. Landau and E. M. Lifshits, *Fluid Mechanics*. Pergamon Press, Oxford, 1987.

[117] W. Knap, Y. Deng, S. Rumyantsev, J.-Q. Lü, M. S. Shur, C. A. Saylor, and L. C. Brunel, *Resonant detection of subterahertz radiation by plasma waves in a submicron field-effect transistor*, Appl. Phys. Lett. **80**, 3433 (2002).

[118] W. Knap, V. Kachorovskii, Y. Deng, S. Rumyantsev, J.-Q. Lü, R. Gaska, M. S. Shur, G. Simin, X. Hu, M. Asif Khan, C. A. Saylor, and L. C. Brunel, *Nonresonant detection of terahertz radiation in field effect transistors*, J. Appl. Phys. **91**, 9346 (2002).

[119] Fujitsu Compound Semiconductor Inc., *Fujitsu Microwave Semiconductor Databook*. 2355 Zanker Rd., San Jose, CA 95131-1138, USA., 1999.

[120] D. B. But, C. Drexler, M. V. Sakhno, N. Dyakonova, O. Drachenko, F. F. Sizov, A. Gutin, S. D. Ganichev, and W. Knap, *Nonlinear photoresponse of field effect transistors terahertz detectors at high irradiation intensities*, J. Appl. Phys. **115**, 164514 (2014).

[121] K. S. Romanov and M. I. Dyakonov, *Theory of helicity-sensitive terahertz radiation detection by field effect transistors*, arXiv:1303.0144v (2013).

[122] S. N. Danilov, B. Wittmann, P. Olbrich, W. Eder, W. Prettl, L. E. Golub, E. V. Beregulin, Z. D. Kvon, N. N. Mikhailov, S. A. Dvoretsky, V. A. Shalygin, N. Q. Vinh, A. F. G. van der Meer, B. Murdin, and S. D. Ganichev, *Fast detector of the ellipticity of infrared and terahertz radiation based on HgTe quantum well structures*, J. Appl. Phys. **105**, 13106 (2009).

[123] L. Vicarelli, M. S. Vitiello, D. Coquillat, A. Lombardo, A. C. Ferrari, W. Knap, M. Polini, V. Pellegrini, and A. Tredicucci, *Graphene field-effect transistors as room-temperature terahertz detectors*, Nature Mat. **11**, 865 (2012).

Danksagung

Zum Abschluss möchte ich mich bei allen Menschen bedanken, die mich während der Promotion begleitet haben und zum Gelingen dieser Arbeit maßgeblich beigetragen haben.

An erster Stelle gilt mein Dank Sergey Ganichev, der mir die Möglichkeit zur Promotion in seiner Arbeitsgruppe gegeben hat. Ich bedanke mich für die stetige Hilfsbereitschaft und zahlreichen Stunden der Diskussion.

Ebenso möchte ich mich bei meiner Familie bedanken, die mir Studium und Promotion ermöglicht hat und für stetige Ablenkung und Unterhaltung sorgte.

Bedanken möchte ich mich auch bei allen Kollegen und Kooperationspartnern. Peter Olbrich und Sergey Danilov waren meine Hauptansprechpartner in wissenschaftlichen Fragen. Danke für die Geduld. Bei den von mir betreuten Studenten Michael Schafberger, Marion Hirmer, Johannes Buchner, Florian Müller und Florian Rückerl möchte ich mich für die Unterstützung zu den Experimenten für diese Dissertation bedanken. Ebenso gilt mein Dank den langjährigen Doktorandenkolleginnen und -kollegen Christina Zoth (Danke fürs Korrekturlesen), Johannes Karch, Sebastian Stachel und Vera Lechner für die Zusammenarbeit. Danke auch an Toni Humbs, Hannelore Lanz und Ulla Turba für die Unterstützung bei technischen und formellen Problemen. Allen weiteren aktuellen und ehemaligen Mitgliedern der AG Ganichev sei an dieser Stelle ebenfalls gedankt. Ebenso geht ein Dankeschön an die Mitarbeiter aller Institute, die mich mit Proben versorgt haben und bereits namentlich im Verlauf der Dissertation genannt wurden. Ein besonderer Dank gilt auch den russischen Partnern Vasily Bel'kov, Sergey Tarasenko, Mikhail Glazov, Leonid Golub und Vadim Shalygin für Tips zu den Experimenten und den theoretischen Hintergrund zu den Resultaten. Danke auch für die Gastfreundschaft während meines Besuches in St. Petersburg. An dieser Stelle möchte ich auch zu meinen langjährigen Uni-Weggefährten Tommi Stangl und Daniel Schmid "Vergelt's Gott" sagen.

Last but not least bedanke ich mich bei meiner Freundin Andrea Hartl für die liebevolle Unterstützung in den letzten Jahren.